Kinematic evolution, metamorphism, and exhumation of the Greater Himalayan Series, Sutlej River and Zanskar regions of NW India

Donald William Stahr, III

Dissertation submitted to the faculty of the
Virginia Polytechnic Institute and State University
in partial fulfillment of the requirements for the degree of

Doctor of Philosophy
in
Geosciences

Richard D. Law
Mark J. Caddick
Robert J. Tracy
James A. Spotila
Michael P. Searle

May 6, 2013
Blacksburg, VA

Keywords: kinematic vorticity, P–T path analysis, quartz crystallographic fabrics

Kinematic evolution, metamorphism, and exhumation of the Greater Himalayan Series, Sutlej River and Zanskar regions of NW India

Donald William Stahr, III

Abstract

The Himalayan orogen provides a natural laboratory to test models of orogenic development due to large-scale continental collision. The Greater Himalayan Series (GHS), a lithotectonic unit continuous along the entire length of the belt, comprises the metamorphic core of the Himalayan orogen and underlies the highest topography. GHS rocks are exposed as a moderately north-dipping slab bounded below by the Main Central Thrust (MCT) and above by the South Tibetan Detachment System (STDS) of normal faults. Coeval reverse- and normal-sense motion on the crustal-scale MCT and STDS ductile shear zones allows the GHS to be modeled as an extruded wedge or channel of mid-crustal material. Due to this unique tectonic setting, the deformation path of rocks within the bounding shear zones and throughout the core of the GHS profoundly influences the efficiency of extrusion and exhumation processes. Attempts to quantify GHS deformation and metamorphic evolution have provided significant insight into Himalayan orogenic development, but these structural and petrologic studies are often conducted in isolation. Penetrative deformation fabrics developed under mid-upper amphibolite facies conditions within the GHS argue that deformation and metamorphism were coupled, and this should be considered in studies aimed at quantifying GHS teconometamorphic evolution.

This work focuses on two projects related to the coupled deformation, thermal and metamorphic evolution during extrusion and exhumation of the GHS, focused on the lower and upper margins of the slab. A detailed examination of the P–T history of a schist collected from within the MCT zone of the Sutlej River, NW India, provides insight into the path experienced by these rocks as they traveled through the crust in response to the extreme shortening related to India-Asia collision. Combined forward thermodynamic and diffusion modeling indicates compositional zoning preserved in garnet has remained unmodified since growth and can be related directly to the P–T–X evolution of rocks from this zone. Classic porphyroblast-matrix relationships coupled with the above models provide a structural framework within which to interpret the microstructures and provide additional constraints on the relative timing of metamorphic and deformation events.

A combined microstructural and quartz petrofabric study of rocks from the highest structural levels of the GHS in the Zanskar region was completed. This work provides the first quantitative estimate of temperatures attending normal-sense shearing along the Zanskar Shear Zone, the westernmost strand of the STDS. Results indicate penetrative top-N (extensional) deformation occurred at elevated temperatures and resulted in the telescoping of isothermal surfaces present during shearing and extrusion of GHS rocks. Simple geometric models invoking heterogeneous simple shear parallel to the overlying detachment require dip-slip displacement magnitudes on the order of 15–40 km, identical to estimates derived from nearby barometric analyses.

Finally, focus is given to the rotational behavior of rigid inclusions suspended in a flowing viscous matrix from a theoretical perspective. Predictions of clast rotational behavior have been used to

construct several kinematic vorticity estimation techniques that have become widely adopted for quantitative studies of naturally deformed rocks. Despite the popularity of the techniques, however, basic questions regarding clast-based analyses remain open. Therefore a numerical model was constructed and a systematic investigation of 2- and 3D clasts suspended in steady and non-steady plane-strain flows was undertaken to determine likely sources of error and the intrinsic strengths and limitations of the techniques.

Acknowledgements

I thank my parents for their tireless support and endless encouragement.

My advisory committee deserve thanks for their help in bringing this project to a successful conclusion.

My friends and co-workers have made this experience vastly more enjoyable than it could ever have been otherwise.

My deepest gratitude to each of you, for without you achieving this milestone would have been impossible.

Attributions

Chapter 1 was published as Stahr, III, D.W., and Law, R.D., 2011, Effect of finite strain on clast-based vorticity gauges. Journal of Structural Geology 33, 1178–1192. DW Stahr was responsible for project conception, development of computer code for numerical modeling, calculating and drafting all figures and animations, and writing the manuscript. RD Law helped clarify portions of the manuscript.

Chapter 2, "Strain memory of rigid inclusion shape fabrics – how sensitive are clasts to temporal vorticity changes?" will be submitted to Journal of Structural Geology for publication in a special issue devoted to 'Deformation Processes in Lithospheric High Strain Zones'. DW Stahr was responsible for project conception, development of computer code for numerical modeling, calculating and drafting all figures and animations, and writing the manuscript. RD Law helped clarify portions of the manuscript.

Chapter 3, "Stahr, III, D.W., Caddick, M.J., Law, R.D., Tracy, R.J., and Ahmad, T., Coupled deformation and metamorphism within the Main Central Thrust zone, Sutlej valley, NW India" may be submitted to Journal of Metamorphic Geology. DW Stahr was responsible for conceiving the project, data acquisition, petrologic calculations and forward thermodynamic modeling, drafting all figures, and writing the manuscript. MJ Caddick developed the diffusion code used in a portion of the modeling. RJ Tracy assisted with collection of electron microprobe data. T Ahmad provided valuable field assistance. RD Law assisted with sample collection during the May 2009 research expedition to Sutlej River valley.

Chapter 4, "Deformation temperatures at the top of the Higher Himalayan Crystallines, Zanskar region, NW India" may be submitted to Journal of Structural Geology. DW Stahr was responsible for collecting samples in the field, laboratory data acquisition, drafting all figures and writing the manuscript. RD Law provided instruction on collecting quartz fabric data using the universal stage.

Contents

List of Tables

List of Figures

Chapter 1

Effect of finite strain on clast-based vorticity gauges

Donald W. Stahr, III[1], Richard D. Law[1]

[1]*Department of Geosciences, Virginia Polytechnic Institute and State University, Blacksburg, VA, 24061, USA*

Published July 2011 in *Journal of Structural Geology*, 33, 1178–1192.

Abstract

Clast-based vorticity gauges utilize orientations of grains assumed to have behaved as isolated rigid particles suspended in a flowing viscous matrix. A fundamental assumption behind use of the method is that sufficient strain has accumulated for high aspect ratio grains to rotate into positions approaching their stable sink orientation, and that clasts below a critical aspect ratio may be observed in any orientation relative to the flow plane. We constructed a numerical model to explore the effect of variable finite strain on development of the orientation distribution of a large population of rigid clasts embedded in a viscous medium for end-member pure and simple shear and for several distinct general shear flows. Our model predicts the technique will tend to produce vorticity overestimates for lower vorticity flows for a wide range of finite strain. The model also indicates that clast populations in moderate to high vortical flows tend to develop shape preferred orientations that closely resemble those expected for flows of lower vorticity. We conclude that clast-based methods are not effective for extracting detailed kinematic information from a mylonite deformed in a flow with arbitrary boundary conditions. In fact, it appears that most general shear flows continued long enough to develop moderate–high finite strains will tend to produce a clast orientation distribution that will yield a visual estimate of the critical aspect ratio that suggests approximately equal contributions of pure and simple shear components.

1.1 Introduction

Since the introduction of kinematic vorticity into the geological literature (McKenzie, 1979; Means et al., 1980), and the development of methods for extracting these data from naturally deformed rocks (e.g., Passchier, 1986, 1987; Vissers, 1989; Wallis, 1992; Wallis et al., 1993; Simpson and De Paor, 1993), structural studies of orogenic belts have increasingly focused on determining the boundary conditions of flow during ductile deformation in high-strain zones. Results of these investigations have repeatedly shown crustal-scale shear zones from a wide array of tectonic settings involved a departure from ideal simple shear (e.g., Passchier, 1987; Vissers, 1989; Wallis et al., 1993; Xypolias and Doutsos, 2000; Law et al., 2004; Jessup et al., 2006, 2007; Bailey et al., 2007; Johnson et al., 2009). The implications of these results are significant for several reasons. Consider a shallowly dipping mylonite zone, a common feature in orogenic hinterlands, deforming by simultaneous pure and simple shearing [here we follow previous authors (e.g., Ramberg, 1975) in using the suffix *-ing* to emphasize terms related to the deformation process]. The pure shearing component of an isochoric, plane-strain, sub-simple shearing deformation causes thinning perpendicular to the zone boundaries. Strain compatibility arguments require that material must simultaneously stretch parallel to the shear zone boundary. Material in such a narrowing-lengthening shear zone (Simpson and De Paor, 1993; Tikoff and Fossen, 1999) is likely directed toward the synorogenic

topographic surface, causing a material flux from lower to higher crustal levels (i.e., from orogenic core to foreland). Purely geometric arguments indicate the magnitude and rate of extrusion of material increase rapidly from the core to foreland of the orogen forcing an increase in strain rate at higher structural levels (Law, 2010). Such coupling of middle and shallow crustal levels may help drive deformation in the orogenic foreland. This simple example illustrates that reliable methods of determining kinematic parameters from high-strain zones are critically important for meaningful interpretation of structural evolution within such ductile deformation zones.

Several vorticity gauges, including: 1) deformed vein sets (Talbot, 1970; Hutton, 1970; Passchier, 1986); 2) clast-based gauges (Passchier, 1987; Simpson and De Paor, 1993; Wallis et al., 1993); 3) quartz petrofabric and strain ratio (R_{XZ}/β) (Wallis, 1992, 1995); 4) oblique dynamically recrystallized grain shape foliation (Wallis, 1995); R_{XZ}/δ method of Xypolias (2009, 2010); 5) angle between macroscopic foliation and shear zone boundary (R_{XZ}/θ) (Tikoff and Fossen, 1995); and 6) flanking structures (Grasemann and Stüwe, 2001) have been applied to natural rocks. Clast-based vorticity gauges are the most commonly applied to natural samples due to: 1) their relative simplicity and rapid application; and 2) many of the assumptions required for the technique to be valid are apparently met (see Passchier, 1987). Early theoretical models published by Masuda et al. (1995) indicated that clast-based techniques may be useful to broadly discriminate between coaxial and non-coaxial flow. However, even with the increased use during the last 15 years (e.g., Passchier, 1987; Vissers, 1989; Wallis et al., 1993; Simpson and De Paor, 1997; Holcombe and Little, 2001; Xypolias and Koukouvelas, 2001; Bailey and Eyster, 2003; Law et al., 2004; Carosi et al., 2006; Jessup et al., 2006, 2007; Xypolias and Kokkalas, 2006; Bailey et al., 2007; Marques et al., 2007; Thigpen et al., 2010), no advance has been made on the role finite strain plays on the evolution of clast orientation distributions for different flow types.

Finite strain magnitude is critically important in all vorticity estimation methods as it is either an explicit parameter (e.g., R_{XZ}/θ, R_{XZ}/β, and R_{XZ}/δ methods), or for the clast-based method in particular, it is tacitly assumed that sufficient strain has accumulated for high aspect ratio grains to have rotated into their stable positions. Because finite strain is a fundamental parameter for determining the porphyroclast orientation distribution produced during deformation, we view the lack of knowledge of strain state as a limit on the usefulness of vorticity estimates made *solely* from clast-based techniques, and argue that multiple techniques should be used to constrain deformation

kinematics.

In this paper we first review the mathematical theory necessary to describe pure, simple, and sub-simple shearing flow and use this theoretical framework to model a large population of rigid elliptical objects in viscous flows of variable kinematic vorticity and at a wide range of finite strains. Our primary interest lies in discovering if there exists a single value of finite strain necessary to produce a well-organized orientation distribution for different flow types. To this end we applied the governing equations (and therefore assumptions and limitations) derived in the seminal paper by Ghosh and Ramberg (1976). Some surprising behavior is predicted at moderate to high kinematic vorticity and high finite strains. Implications of these results are discussed in a geological context.

1.2 Mathematical framework

1.2.1 Description of flow and progressive deformation

The velocity field about a point in a deforming continuum is described by the velocity gradient tensor, $\mathbf{L}$,

$$\mathbf{v} = \mathbf{L}\mathbf{x} \tag{1.1}$$

where $\mathbf{v}$ is a velocity vector, or the time derivative of position vector $\mathbf{x}$ (i.e., $\mathbf{v} = d\mathbf{x}/dt$). The associated velocity gradient equations become (Means et al., 1980):

$$v_i = L_{ij}x_j \tag{1.2}$$

where v_i are the velocity components at position x_j at an instant in time, and

$$L_{ij} = \frac{\partial v_i}{\partial x_j} = \begin{bmatrix} L_{11} & L_{12} \\ L_{21} & L_{22} \end{bmatrix}$$

(see Malvern, 1969, p. 146) are the spatial velocity gradients for a two-dimensional flow (see Fig. 1.9). If the velocity gradient tensor components L_{ij} are constant the flow is homogeneous (Means et al., 1980). For isochoric plane strain monoclinic flow with simultaneous pure and simple shearing,

FIGURE 1.1. Steady flows considered in this paper. (a) Mohr circle for given numerical $\mathbf{L}$ ($\dot{\varepsilon}$ – ω space). Note that a constant value of unity is used as simple shearing strain rate ($\dot{\gamma}$) for simple shear and all general shear flows. Eigenvectors ($\boldsymbol{\xi}_i$) of $\mathbf{L}$, instantaneous stretching axes (ISA_i), and angle (α) between eigenvectors in real space indicated on Mohr construction. Percent simple shear and W_k number also indicated for each flow. (b) Velocity field in real space for associated $\mathbf{L}$. Each arrow points in the direction of the velocity vector at the spatial point coincident with vector tail, and is scaled relative to velocity magnitude. (c) Representative particle paths for associated $\mathbf{L}$ and velocity field for each flow. Flow apophyses (labeled by coincident eigenvector) and ISA_i indicated. Arrows superimposed on curves indicate temporal evolution of particle positions. Thin curves represent hyperbolic particle paths of material points, thick curves represent straight-line particle paths directly toward or away from origin parallel to flow eigenvectors.

L may be written as

$$\mathbf{L} = \begin{bmatrix} \dot{\varepsilon}_x & \dot{\gamma} \\ 0 & \dot{\varepsilon}_y \end{bmatrix} \tag{1.3}$$

where $\dot{\varepsilon}_x$ is the pure shearing strain rate and $\dot{\gamma}$ is the simple shearing strain rate, here taken perpendicular and parallel to the abscissa, respectively. Setting $\dot{\varepsilon}_y = -\dot{\varepsilon}_x$ forces the deforming material to be incompressible. The eigenvectors, $\boldsymbol{\xi}_i$, of **L** give the orientations of the flow apophyses (Ramberg, 1975; Passchier, 1988).

The velocity gradient tensor, **L**, may be decomposed into the symmetric stretching tensor, $\dot{\mathbf{S}}$, and skew-symmetric vorticity tensor, **W**, (Malvern, 1969, p. 147; Bobyarchick, 1986)

$$\mathbf{L} = \dot{\mathbf{S}} + \mathbf{W} \tag{1.4}$$

where

$$\dot{\mathbf{S}} = \begin{bmatrix} \dot{\varepsilon}_x & \frac{1}{2}\dot{\gamma} \\ \frac{1}{2}\dot{\gamma} & \dot{\varepsilon}_y \end{bmatrix} \tag{1.5}$$

and

$$\mathbf{W} = \begin{bmatrix} 0 & \frac{1}{2}\dot{\gamma} \\ -\frac{1}{2}\dot{\gamma} & 0 \end{bmatrix}. \tag{1.6}$$

The eigenvectors and eigenvalues of $\dot{\mathbf{S}}$ provide information on the orientation and magnitude of the instantaneous stretching axes (ISA_i) and instantaneous stretching rates ($\dot{s}_i$) of the flow, respectively. The vorticity tensor, **W**, has components of angular velocity and describes the rotation rate of elements in the deforming material.

The kinematic vorticity number, W_k, is a useful way of quantifying the instantaneous non-coaxiality of the flow at a point in space and an instant in time, and has a unique value for any distinct flow. By definition, W_k is an instantaneous quantity, but for the steady flows considered here the vorticity number remains constant during progressive deformation. The quantity s_r, defined as the ratio of pure to simple shearing strain rate, $s_\mathrm{r} = \dot{\varepsilon}_x/\dot{\gamma}$ (Ghosh and Ramberg, 1976), is also a measure of the degree of non-coaxiality of the flow and may be expressed as a function of

the kinematic vorticity number by the relation (Ghosh, 1987, eqn. 9)

$$s_{\mathrm{r}} = \frac{1}{2}\sqrt{\frac{1}{W_k^2} - 1}. \tag{1.7}$$

Conversely, the kinematic vorticity may be calculated from knowledge of the instantaneous pure and simple shearing strain rates by the relation

$$W_k = \cos\left[\tan^{-1}\left(2\frac{\dot{\varepsilon}_x}{\dot{\gamma}}\right)\right] \tag{1.8}$$

or more simply

$$W_k = \cos(\alpha) \tag{1.9}$$

where α is the acute angle between the eigenvectors ($\boldsymbol{\xi}_i$) of $\mathbf{L}$ (for derivation see Bobyarchick, 1986). By choosing appropriate values for s_{r} or W_k we can form a velocity gradient tensor, $\mathbf{L}$, to produce the velocity field of a deformation of any vorticity number of interest.

From (1.8) it is clear that identical W_k values result from any combination of $\dot{\varepsilon}_x$ and $\dot{\gamma}$ that yield the same s_{r} value. Thus, any choice of $\dot{\varepsilon}_x$ and $\dot{\gamma}$ that yield the same ratio give rise to identical velocity fields; only the time required to accumulate a finite strain state will vary. Note from (1.7) that s_{r} increases without bound as W_k approaches zero. Inspection of (1.8) and (1.9) reveals that W_k is a nonlinear function of s_{r} or α. W_k ranges from 0 ($\alpha = 90°$) for pure shearing to 1 ($\alpha = 0°$) for simple shearing (Fig. 1.2). Flows with $W_k > 1$, where the rotation component is greater than that for strict simple shear, are also possible but are not considered here.

The position gradient tensor, $\mathbf{D}$, relates the position of a particle in the deformed state, $\mathbf{x}'$, to its position in the undeformed state, $\mathbf{x}$:

$$\mathbf{x}' = \mathbf{D}\mathbf{x}. \tag{1.10}$$

Provost et al. (2004, eqn. 29) have shown that a relationship between $\mathbf{L}$ and $\mathbf{D}$ exists in the form

$$\mathbf{D} = \exp[\mathbf{L}\Delta t] \tag{1.11}$$

where $\Delta t = t - t_0$ is the time elapsed since the onset of deformation (or since a previously deformed state). It is therefore possible to use this relationship to determine the position of a particle at any

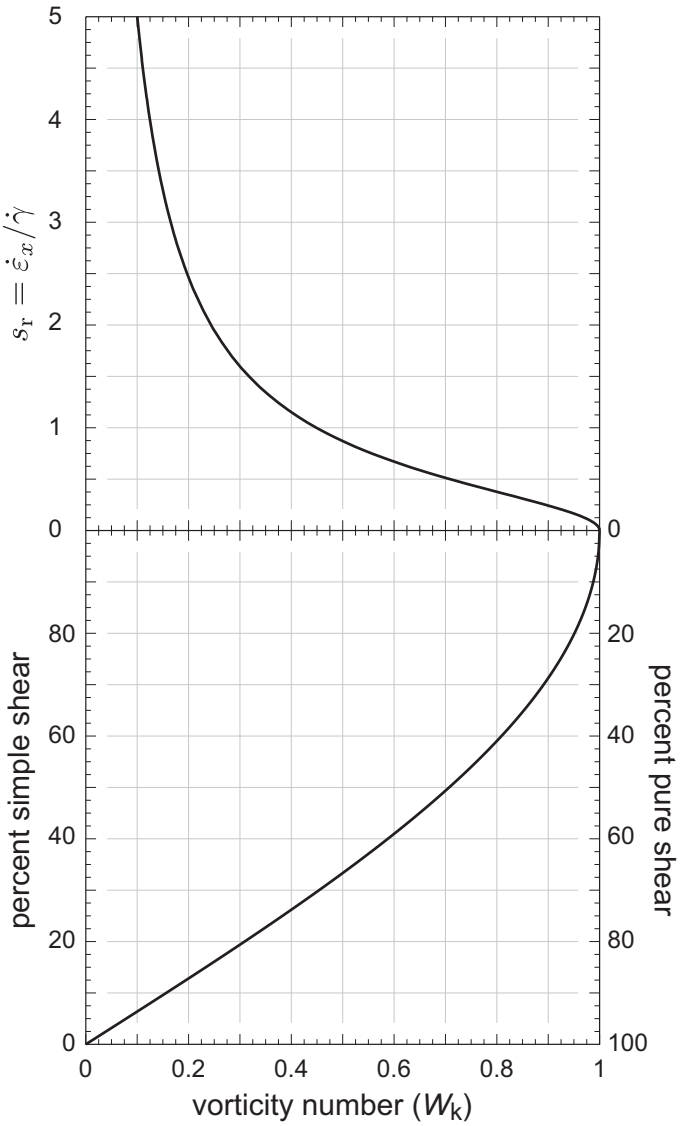

FIGURE 1.2. Variation of percent simple shear and $s_r = \dot{\varepsilon}_x/\dot{\gamma}$ with kinematic vorticity number, W_k. Note both quantities s_r and percent simple shear are moderately to strongly nonlinear for different ranges of W_k. Percent simple shear rapidly increases as W_k approaches unity. Note also the quantity s_r increases without bound as pure shearing end-member is approached.

time t for a given flow. If we let deformation begin at $t_0 = 0$ then

$$\mathbf{D} = \exp[\mathbf{L}t] = \begin{bmatrix} \exp(\dot{\varepsilon}_x t) & \dfrac{1}{s_r}\sinh(\dot{\varepsilon}_x t) \\ 0 & \exp(\dot{\varepsilon}_y t) \end{bmatrix} \tag{1.12}$$

(cf. Ramberg, 1975, eqn. 38; see also Bobyarchick, 1986). It is therefore possible to determine particle paths for any $\mathbf{L}$ and any choice of kinematic vorticity number.

The finite strain state is also simply related to $\mathbf{D}$ (and therefore $\mathbf{L}$). The tensor, $\mathbf{F}$, (Finger

tensor of Tikoff and Fossen, 1993) contains a complete description of the finite strain accumulated to time t for a given flow. $\mathbf{F}$ may be obtained from $\mathbf{D}$ by forming

$$\mathbf{F} = \mathbf{D}\mathbf{D}^{\mathrm{T}} \tag{1.13}$$

(Malvern, 1969, p. 174) where $\mathbf{D}^{\mathrm{T}}$ is the matrix transpose of $\mathbf{D}$. The eigenvalues of $\mathbf{F}$ give the squares of the semi-axes of the finite strain ellipse and the eigenvectors give their orientations (Tikoff and Fossen, 1993). Thus, by simply choosing appropriate instantaneous strain rates for a particular kinematic vorticity number of interest we may calculate the velocity field and any particle path. We may also determine the finite matrix strain parameters at any time during the flow.

1.3 Orientation of rigid elliptical objects embedded in a steady viscous flow

1.3.1 Rotation rate of elliptical clasts

We have chosen to use the angle (θ) between the clast long axis and flow plane in our analysis to reflect a reference frame commonly used in the kinematics literature (cf. Kanagawa, 1996). Here we take the angle as positive if the clast is leaning in the direction of the applied simple shearing component; a dextral shear couple is considered positive (Fig. 1.3). Clasts rotating counterclockwise

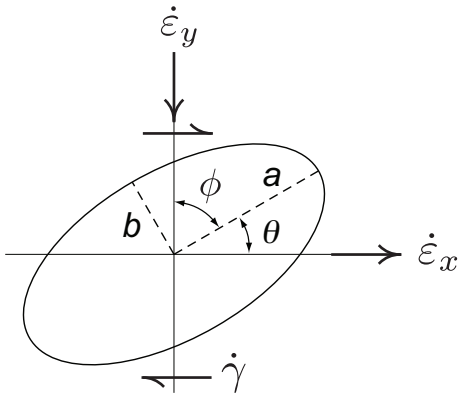

FIGURE 1.3. Kinematic reference frame used in this paper. The angle (θ) between clast long axis and extensional flow apophysis (i.e., flow or shear plane) measured as shown; counterclockwise rotation considered positive. Clast aspect ratio (R) obtained by forming the ratio of long to short semi-axis lengths, $R = a/b$. The angle ϕ was used in the work by Ghosh and Ramberg (1976). Note $\theta = 90 - \phi$.

in this frame give rise to a positive rotation rate. To accomplish this change of reference frame we

substituted the angle $\theta = 90 - \phi$ into the independent variable ϕ in Ghosh and Ramberg's equations (1) and (2).

Upon substitution, the rotation rate for a clast in simple shear becomes

$$\begin{aligned}\dot{\theta_\gamma} &= -\dot{\gamma}\frac{R^2\cos^2(90-\phi)+\sin^2(90-\phi)}{R^2+1}\\ &= -\dot{\gamma}\frac{R^2\sin^2(\theta)+\cos^2(\theta)}{R^2+1}.\end{aligned} \tag{1.14}$$

The rotation rate for a clast in pure shear flow becomes

$$\begin{aligned}\dot{\theta_\varepsilon} &= -\dot{\varepsilon}_x\frac{R^2-1}{R^2+1}\sin\left[2(90-\phi)\right]\\ &= -\dot{\varepsilon}_x\frac{R^2-1}{R^2+1}\sin(2\theta).\end{aligned} \tag{1.15}$$

Addition of the instantaneous clast rotation rates in pure and simple shear gives the expression for the instantaneous rotation rate of a clast in a general shear flow

$$\dot{\theta} = -\dot{\varepsilon}_x\frac{R^2-1}{R^2+1}\sin(2\theta) - \dot{\gamma}\frac{R^2\sin^2(\theta)+\cos^2(\theta)}{R^2+1}$$

which, after minor manipulation becomes

$$\dot{\theta} = -\dot{\gamma}\left[A\cos^2(\theta) + B\sin(2\theta) + C\sin^2(\theta)\right] \tag{1.16}$$

where

$$A = \frac{1}{R^2+1}, \quad B = s_{\mathrm{r}}\frac{R^2-1}{R^2+1}, \quad C = \frac{R^2}{R^2+1}.$$

Note the similarity of (1.16) to equation (4a) of Ghosh and Ramberg (1976).

1.3.2 Final clast orientation

The relationship between the initial and final angle of a clast suspended in the flow is obtained by integrating the rotation rate equations (1.14)–(1.16). The boundary conditions in our analysis are: 1) γ (or ε_x) $= 0$ and $\theta = \theta_0$ when $t = 0$; and 2) γ (or ε_x) $= \dot{\gamma}t$ (or $\dot{\varepsilon_x}t$) and $\theta = \theta$ when $t = t$ (see

also Kanagawa 1996). Thus, the simple shear component at time t is given by

$$\gamma = \int_{t=0}^{t=t} \dot{\gamma}\, \mathrm{d}t = \dot{\gamma} t.$$

Similarly, the value of finite pure shear strain at time t is

$$\varepsilon_x = \int_{t=0}^{t=t} \dot{\varepsilon}_x\, \mathrm{d}t = \dot{\varepsilon}_x t$$

(see also Masuda et al., 1995). Alternatively, using the continuum mechanics notation

$$\gamma = L_{12} t$$

and

$$\varepsilon_x = L_{11} t$$

where $L_{ij}t$ is a component of the velocity gradient tensor multiplied by the temporal duration of deformation. Once the flow type and finite strain to be modeled have been chosen, parameters from the matrix strain may be input into the finite rotation equations given below to determine the orientation of a clast in the flow at any time t (Fig. 1.4).

Simple shear flow

We may rewrite equation (1.14) and integrate both sides between the boundaries discussed above to obtain

$$-\dot{\gamma} t = \int_{\theta_0}^{\theta} \frac{R^2 + 1}{R^2 \sin^2(\theta) + \cos^2(\theta)}\, \mathrm{d}\theta. \tag{1.17}$$

Upon integration and solving for the final orientation θ, we obtain

$$\theta = \tan^{-1}\left[\frac{1}{R} \tan\left\{\tan^{-1}\left(R \tan\theta_0\right) - \dot{\gamma} t \frac{R^2}{R^2 + 1}\right\}\right] \tag{1.18}$$

where θ_0 is the initial orientation of the long axis of the elliptical inclusion.

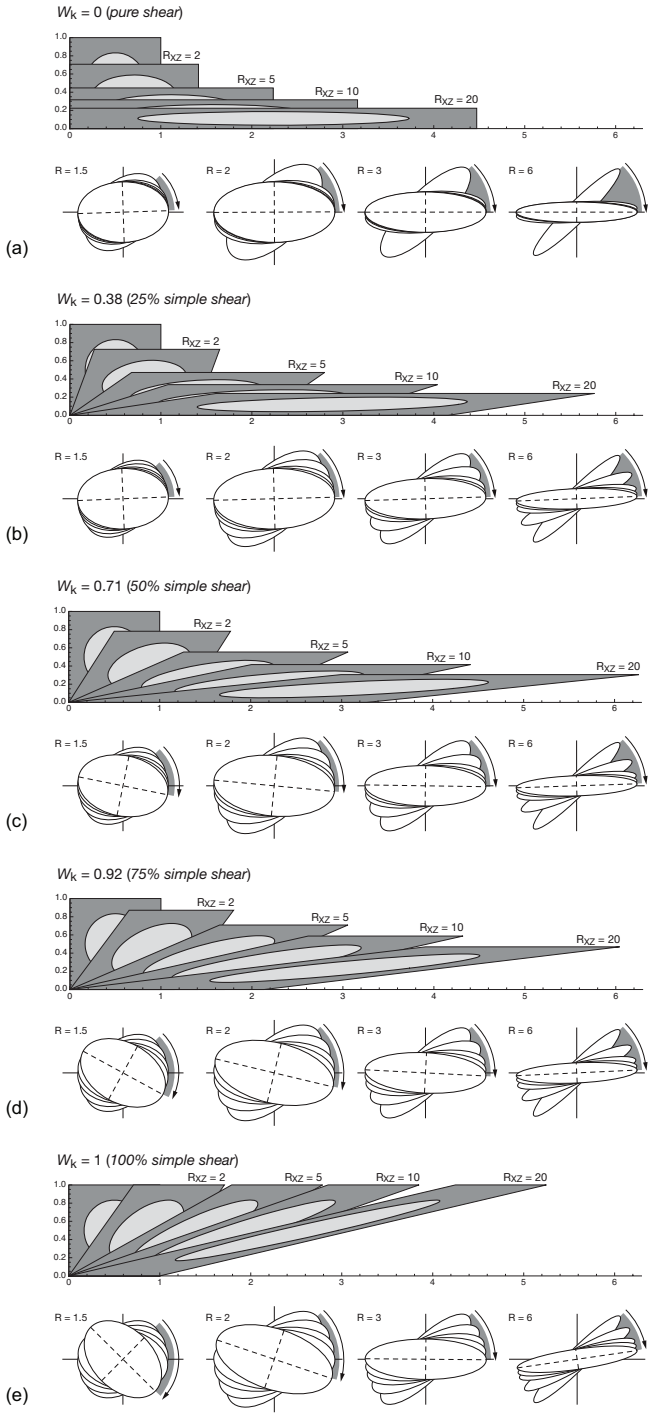

FIGURE 1.4. Orientation of selected individual rigid clasts suspended in a Newtonian matrix during progressive deformation. Dark gray boxes show initially square matrix element deformed to strain ratios of R_{XZ} = 2, 5, 10, and 20. Passive circular markers deformed into finite strain ellipses indicated by lighter gray screen at each deformation stage. Abscissa and ordinate scales equal. Shown below strained matrix elements are orientations of rigid clasts (no pattern) of aspect ratio R = 1.5, 2, 3, and 6 embedded in the matrix at the given R_{XZ} values (all clasts had +45 degrees initial orientation). Dashed lines indicate trace of clast semi-axes after last deformation increment. Arrows indicate sense and approximate amount of clast rotation. (a) Pure shear. (b) $W_k = 0.38$ (25% simple shear). (c) $W_k = 0.71$ (50% simple shear). (d) $W_k = 0.92$ (75% simple shear). (e) Simple shear. Note rapidly increasing shear zone-parallel stretch for flows with higher pure shearing component. Rotation amounts of suspended clasts generally decrease with increasing R for a given flow, while the finite rotation angle increases for constant low aspect ratio clasts for flows of increasing W_k (this trend reverses for higher aspect ratio clasts). See text for discussion.

Pure shear flow

Similarly, we may rewrite equation (1.15) and integrate both sides, such that

$$-\dot{\varepsilon}t = \frac{R^2+1}{R^2-1}\int_{\theta_0}^{\theta}\frac{\mathrm{d}\theta}{\sin(2\theta)}. \tag{1.19}$$

Upon integration and solving for the final orientation θ, we obtain

$$\theta = \tan^{-1}\left[\tan(\theta_0)\cdot\exp\left(-2\dot{\varepsilon}t\frac{R^2-1}{R^2+1}\right)\right]. \tag{1.20}$$

General shear flow

Finally, we may rewrite equation (1.16) and integrate both sides, such that

$$-\dot{\gamma}t = \int_{\theta_0}^{\theta}\frac{\mathrm{d}\theta}{A\cos^2(\theta)+B\sin(2\theta)+C\sin^2(\theta)} \tag{1.21}$$

(cf. Ghosh and Ramberg, 1976, eqn. 10). The integral on the right hand side of (1.21) has three types of solution depending on whether $B^2 > AC, B^2 < AC$, or $B^2 = AC$. The solutions to these integrals may be found in any book of standard mathematical tables. Upon integration, the solutions for θ for each case are (see also Ghosh and Ramberg, 1976):

1. $B^2 > AC$:

$$\theta = \tan^{-1}\left[\frac{P(B+\sqrt{B^2-AC})-B+\sqrt{B^2-AC}}{C(1-P)}\right] \tag{1.22}$$

where

$$P = \frac{C\,\tan(\theta_0)+B-\sqrt{B^2-AC}}{C\,\tan(\theta_0)+B+\sqrt{B^2-AC}}\cdot\exp\left[-2\dot{\gamma}t\sqrt{B^2-AC}\right]$$

2. $B^2 < AC$:

$$\theta = \tan^{-1}\left[\frac{\sqrt{AC-B^2}}{C}\times\tan\left\{\tan^{-1}\left(\frac{C\,\tan(\theta_0)+B}{\sqrt{AC-B^2}}\right)-\dot{\gamma}t\sqrt{AC-B^2}\right\}-\frac{B}{C}\right] \tag{1.23}$$

3. $B^2 = AC$:

$$\theta = \tan^{-1}\left[\frac{1}{C}\left\{\frac{C\,\tan(\theta_0)+B}{1+\dot{\gamma}t(C\,\tan(\theta_0)+B)}-B\right\}\right]. \tag{1.24}$$

1.4 Review of inclusion and passive marker re-orientation in a steady flow

The behavior of individual elliptical and passive line elements in a flowing matrix is critical to understanding the behavior of the larger populations of non-interacting elliptical inclusions that we will discuss throughout the remainder of this paper. Here we briefly review basic properties of the behavior of elements embedded in selected steady flows. Because our model uses the governing equations of Ghosh and Ramberg (1976) the assumptions built into their formulation apply here as well. Namely, we assume: 1) clasts are rigid, elliptical, and are embedded in a linear viscous (i.e., Newtonian) matrix; 2) one symmetry axis of the clast is parallel to the vorticity vector; 3) the flow is steady, with a simultaneous combination of pure and simple shearing; and 4) perfect coupling of the clast and matrix.

1.4.1 Rotation rate of rigid inclusions

In this section we present plots of rate of change of orientation ($\dot{\theta}$) divided by strain rate ($\dot{\varepsilon}_x$ or $\dot{\gamma}$, as appropriate) vs. orientation (θ) of clast long axis. These plots may be thought of as a normalized rotation rate vs. orientation in the flow. The fundamental behavior of rigid particles suspended in a flowing viscous matrix that forms the basis of clast-based vorticity gauges is depicted in these plots. Therefore, considerable attention is devoted to unique aspects of the behavior of clasts in simple shear, pure shear, and mixed flow type.

Simple shear flow

Patterns of rotation rate in a simple shear flow are by far the simplest (Fig. 1.5a). All inclusions rotate synthetic to the imposed shear direction with the exception of a passive line element parallel to the shear plane, which has zero angular velocity. A spherical inclusion rotates at half the applied shear strain rate. Line elements and large aspect ratio (R) grains have lower angular velocities within ± 45 degrees of the flow plane, and higher angular velocities at any other orientation. Rotation rates are a maximum for an inclusion of any aspect ratio when it is at high angles to the flow plane, and minimum when parallel. Note that all elliptical or linear elements embedded in the matrix have identical angular velocities when they are at exactly ± 45 degrees to the flow plane

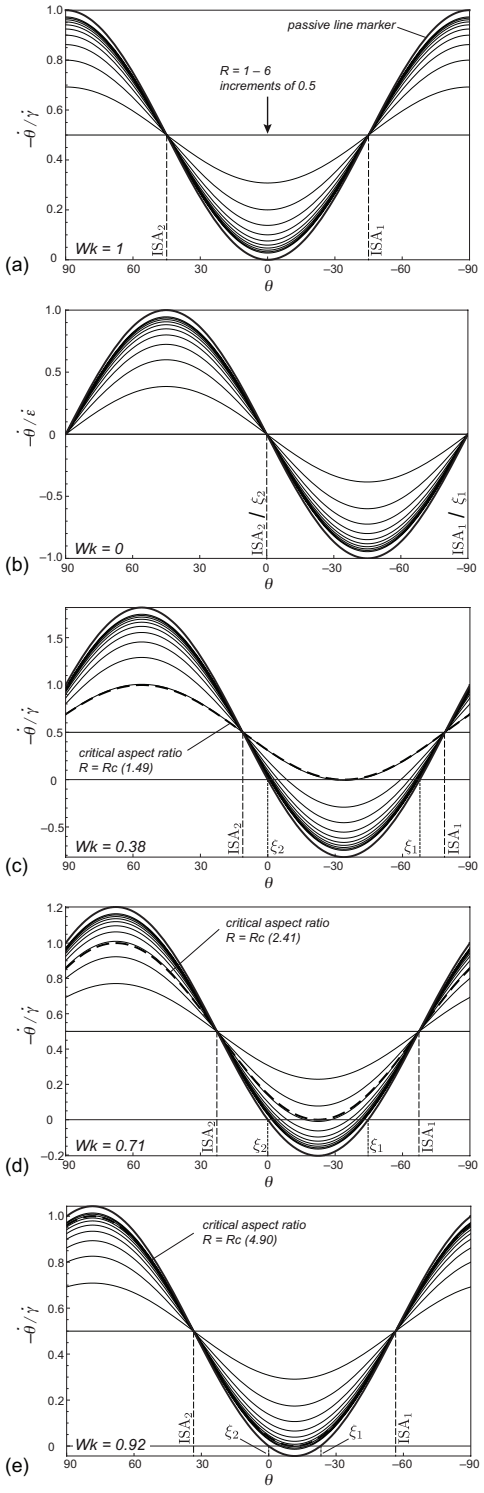

FIGURE 1.5. Normalized rotation rate vs. clast orientation plots for elements embedded in a viscous flow. (a) Simple shear. (b) Pure shear. (c) $W_k = 0.38$ (25% simple shear). (d) $W_k = 0.71$ (50% simple shear). (e) $W_k = 0.92$ (75% simple shear). Thin curves represent clasts with aspect ratios ranging from 1 to 6 in increments of 0.5 (i.e., $R = 1, 1.5, 2, \ldots, 6$); labels omitted for clarity. Thick solid curve represents a passive line marker, thick dashed curve (c–e) represents clast with $R = R_{\text{crit}}$. Passive line markers and clasts (regardless of aspect ratio) have identical angular velocity when parallel to ISA of the flow. Clasts with aspect ratios $R > 5$ approximate behavior of passive line elements. ISA_i and $\boldsymbol{\xi}_i$ indicated by dashed and dotted lines, respectively. Note clasts with $R \approx R_{\text{crit}}$ have rotation rates that are such a small fraction of the applied shear strain rate when in orientations near the flow plane that they may be mistaken for clasts with a stable orientation. Compare Figs. 1.9–1.11. See text for discussion.

(i.e., when they are parallel to the ISA). This is a general feature of suspended clasts in any flow type.

Pure shear flow

Rotation rates of elliptical objects suspended in a pure shear flow are more complex than those in simple shear flow (Fig. 1.5b). Spherical clasts do not rotate, whereas positive and negative rotation rates (i.e., counterclockwise and clockwise rotation, respectively) are predicted for all elongate clasts, depending on orientation. Maximum absolute values of rotation rates are obtained for any non-spherical clast at ±45 degrees to the flattening plane. Grains of higher R always have faster rotation rates (either positive or negative) than grains of lower R in the same orientation. Inclusions and linear elements parallel and perpendicular to the flattening plane (parallel to ISA) have zero angular velocity.

General shear flow

Clasts embedded in a matrix undergoing general shear share attributes with those in both pure and simple shear flow; however, the most significant feature is the existence of a particular aspect ratio whose rotation rate vanishes in a flow of a given vorticity (Fig. 1.5c–e). This aspect ratio is termed the *critical aspect ratio,* R_{crit}. Clasts with $R < R_{\mathrm{crit}}$ rotate synthetic to the imposed simple shearing component only, whereas those with $R > R_{\mathrm{crit}}$ have fields of positive and negative rotation rate. Each clast with $R > R_{\mathrm{crit}}$ has one stable and one metastable orientation in the flow. A clast initially in a metastable orientation, after any perturbation, will rotate toward its stable orientation (i.e., the stable orientation at a lower angle to the flow plane). The value of R_{crit} increases with increasing vorticity number until, in the limit, $R_{\mathrm{crit}} = \infty$ for simple shear flow. Because R_{crit} is unique for a given general shear flow, the kinematic vorticity may theoretically be calculated if this aspect ratio can be determined (Fig. 1.6).

1.4.2 Field of back-rotation

The existence of both negative and positive angular velocities for flows with $0 < W_k < 1$ discussed above indicate that some clasts will rotate *against* the applied shear direction during sub-simple

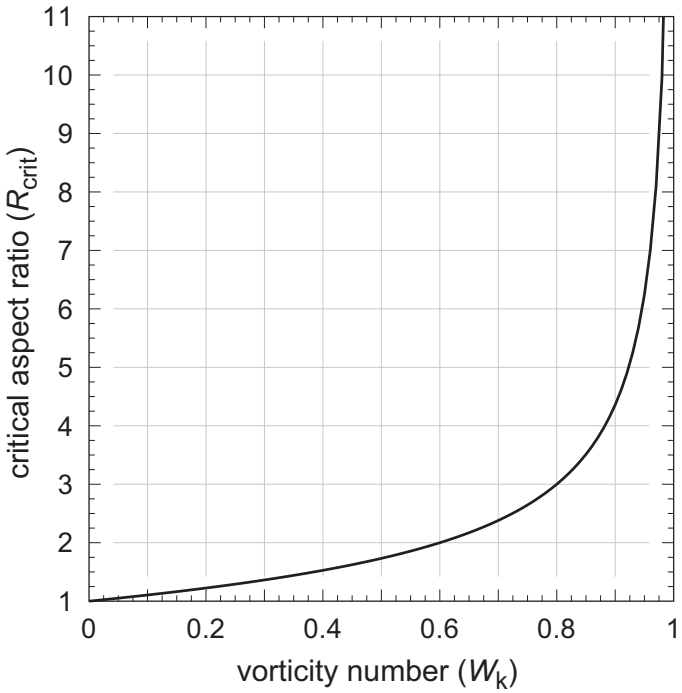

FIGURE 1.6. Relationship between critical aspect ratio (R_{crit}), and kinematic vorticity number (W_k). R_{crit} increases only from 1 to 2 for an increase in W_k of 0 to 0.6 (i.e., an increase from 0–40% simple shearing component). The ability to accurately distinguish flows with R_{crit} in this range may be difficult for natural mylonites. Note also R_{crit} increases rapidly and without bound for kinematic vorticity values above $W_k \approx 0.9$.

shearing. In fact, Figure 5c–e clearly indicates the range of orientations for which a clast may back-rotate is a function of aspect ratio and kinematic vorticity. Clasts with R only slightly greater than R_{crit} have a more restricted range of orientations where back-rotation is possible than clasts with $R \gg R_{\text{crit}}$. In the limit, passive line elements define the widest possible orientation range for back-rotation in a given flow. The orientation where curves representing passive line markers intersect the zero angular velocity contour are by definition the orientation of the flow apophyses (i.e., eigenvectors, $\boldsymbol{\xi}_i$, of the velocity gradient tensor, $\mathbf{L}$). These orientations separate fields of forward and backward rotation for a given flow. It can also be seen that the single stable orientation for clasts with $R = R_{\text{crit}}$ bisects the acute angle between the eigenvectors of $\mathbf{L}$. The size of the field of back-rotation increases rapidly with increasing aspect ratio (Fig. 1.5c–e).

1.5 Kinematic model

1.5.1 Initial and boundary conditions

In an attempt to model as realistic a clast population as possible, we combined observations from 76 mylonitic samples (total of 14 959 measured porphyroclasts) from a variety of lithologies and tectonic settings (Fig. 1.7a–c). Our model utilizes a large population of clasts ($n = 500$) with aspect

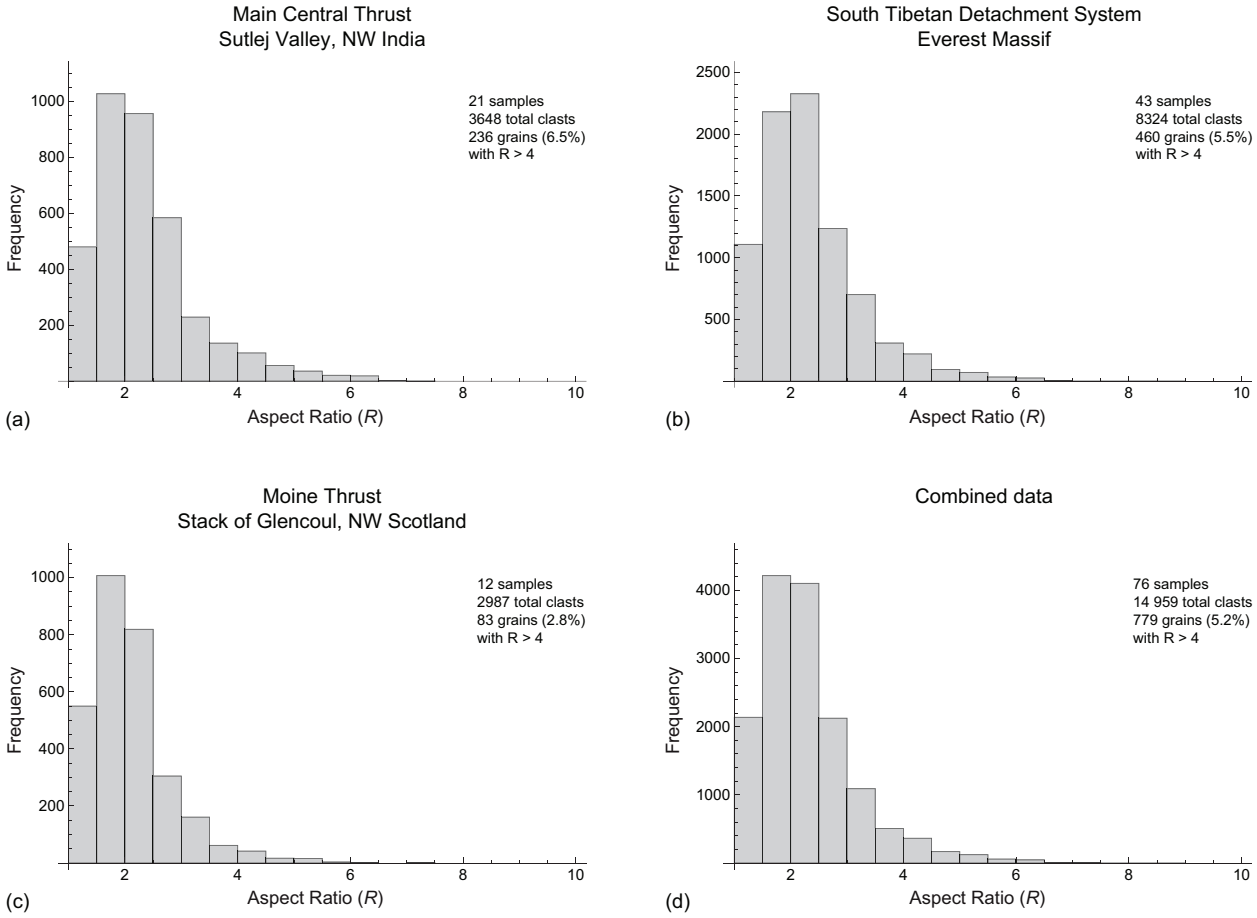

FIGURE 1.7. Histograms showing frequency of clast aspect ratios measured in natural mylonites. (a) Results from examination of 21 mylonitic samples (3648 total clasts) from the Main Central Thrust zone, Sutlej Valley, NW India (unpublished data). (b) Results from examination of 43 mylonitic samples (8324 total clasts) from the South Tibetan Detachment System, Everest Massif (Jessup et al., 2006). (c) Results from examination of 12 mylonitic samples (2987 total clasts) from the Moine Thrust, Stack of Glencoul, NW Scotland (Law, 2010). (d) Results of combined datasets. Note grains with $R \leq 3$ dominate the natural populations, but clasts with $R \geq 4$ are much less common (here they represent between only ∼3 and 6.5% of the population for a given dataset, and ∼ 5% of the total data).

ratios satisfying the requirement $1 \leq R \leq 7$, in the same proportions as our combined dataset (i.e., the histogram of model clasts is identical to that in Fig. 1.7d, but the total data sum to $n = 500$). Initial orientations (θ_0) for our clasts ranged from −90 to +90 degrees and were derived using a

random number generator so every possible pair of R and θ_0 values from the range given above is well-represented in the initial population (Fig. 2.3). The same initial population was used to

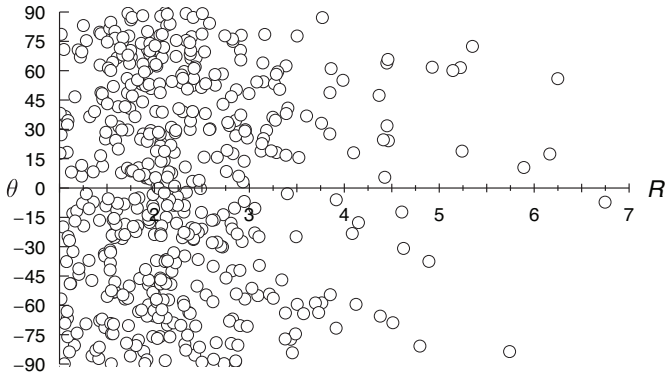

FIGURE 1.8. Initial population. Clast aspect ratios (R) range from 1–7, and initial angles (θ_0) range from −90 to +90 degrees. Clast proportions of total population are as detailed for combined natural datasets (Fig. 1.7d). Pairs (R, θ_0) chosen using a random number generator to represent a homogeneous distribution of clast initial orientations.

calculate the orientation distribution at each finite strain state for each flow.

We modeled flows with W_k values of 0 (pure shear), 0.38 (25% simple shear), 0.71 (50% simple shear), 0.92 (75% simple shear), and 1 (100% simple shear) to investigate the effects of increasing simple shearing component on clast orientation distributions. The orientation distributions shown here were calculated for matrix strain ratios (R_{XZ}) of 2, 5, 10, 20, 50, 100, 200, and 500. Animations depicting the evolution of clast orientation distributions during progressive deformation for all five model flows presented in this paper are provided as an electronic supplement.

1.5.2 Results

It is apparent from our model results that moderate to high finite strains are required for clasts with $R \geq R_{crit}$ to rotate into their stable orientation (Fig. 1.9). However, due to the different response of clasts of variable aspect ratio to the imposed boundary conditions, not all clasts above R_{crit} reach the flow plane after an identical matrix strain, so a well-developed clast orientation distribution is not developed for each flow after the same duration of deformation. In other words, flows of different vorticity require different amounts of finite strain to produce well-organized porphyroclast orientation distribution patterns that will yield reliable results from the rigid grain technique.

The final orientation, or finite angle of rotation, of a clast is a complex function of aspect ratio, initial orientation, flow vorticity, and finite strain. Figure 4 provides insight into the behavior of a

small subset of grains within the larger population used to calculate clast orientation distributions. An initial square matrix element with embedded passive circular marker is shown in the initial configuration and after matrix strains of R_{XZ} = 2, 5, 10, and 20 for each modeled flow. Progressive deformation may be monitored by change in angles or calculated directly by measuring the passive strain ellipse. Shown below the graphical matrix strains in Figure 4 are rigid elliptical clasts of variable aspect ratio (R = 1.5, 2, 3, and 6), all initially at +45 degrees to the flow plane, and their orientation after each matrix strain increment. The figure clearly shows the maximum angle of finite rotation is $\sim$ 90 degrees for a grain with R = 1.5 and a matrix strain of R_{XZ} = 20 in a simple shear flow. All other grains in pure and general shear rotate significantly less after identical matrix strains. This is the case if the clast aspect ratio is well above, below, or near R_{crit} for the flow. Also evident from the figure is a decrease in rotation angle with increasing strain when clast long axes approach parallelism with the flow plane. Most clasts in these examples rotate no more than $\sim$ 20 degrees during progressive matrix strains of 5 to 20. This is an important point that has implications for clast orientation distributions at high finite strain.

1.5.3 Clast orientation distributions at high finite strain

An interesting phenomenon occurs in the models for high W_k flows at moderate to high finite strains (e.g., W_k = 0.92 flow at $R_{XZ} > 10$; Fig. 1.9). Clasts with $R < R_{crit}$ rotate into sub-parallelism with the flow plane and remain near this orientation until very high strains accumulate. Similar results are obtained for all flows, but the phenomenon becomes increasingly apparent for higher W_k flows simply because a similar percentage of R_{crit} occupies a larger R range.

For the case of the W_k = 0.92 flow, clasts with $R \geq 4.4$ (within approximately 10% of R_{crit} = 4.9) reach subparallelism with the extensional flow apophysis and remain near this position regardless of their initial orientation (Fig. 1.10). These clasts do not become significantly re-oriented until matrix strains of $R_{XZ} \approx 275\,000$ ($\dot{\gamma}t \approx 25$), and even then nearly all clasts in this range are predicted to lie within 20 degrees of the flow plane. Thus, for geologically realistic and greater matrix strain ratios, clasts within this range are indistinguishable from grains with $R \geq R_{crit}$; they are effectively stable. If we now examine clasts further separated from R_{crit}, say within $\sim$ 22–10% (i.e., $3.8 \leq R \leq 4.3$), we see the behavior is similar but less pronounced (Fig. 1.11). Here the lower aspect ratio clasts rotate to greater (negative) angles to the flow apophysis by the time we reach the maximum strains

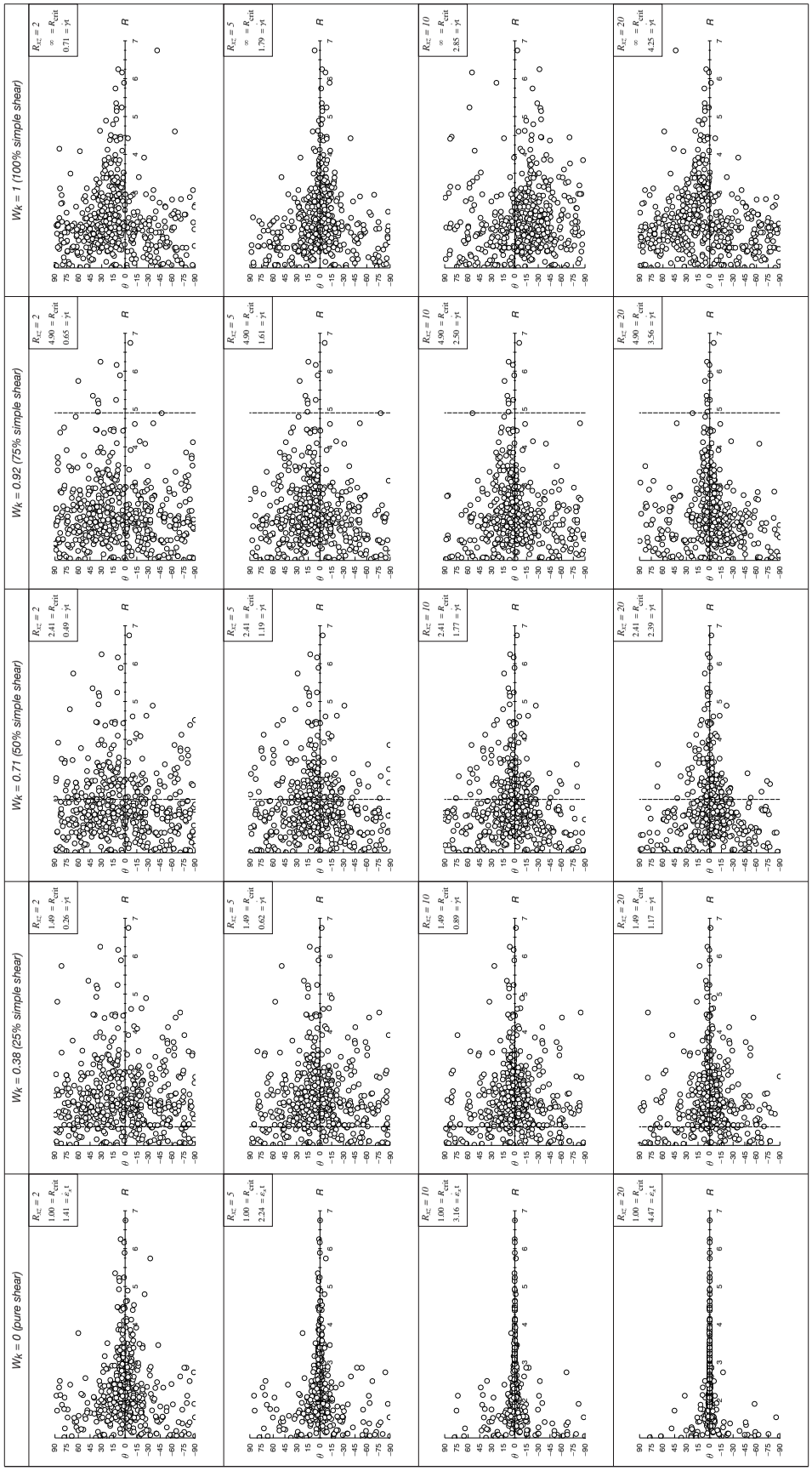

FIGURE 1.9. Kinematic model results for five steady flows ($W_k = 0$, 0.38, 0.71, 0.92, and 1) at eight different finite strain ratios ($R_{XZ} = 2$, 5, 10, 20, 50, 100, 200, and 500). Constant W_k values aligned in columns; rows contain results from different W_k values calculated at identical matrix strain ratios. Dashed vertical lines indicate theoretical R_{crit} for given flow. Finite matrix strain, R_{XZ}, theoretical critical aspect ratio, R_{crit}, and strain component, $\varepsilon = \dot{\varepsilon}_x t$ or $\gamma = \dot{\gamma} t$, used to produce orientation distribution indicated.

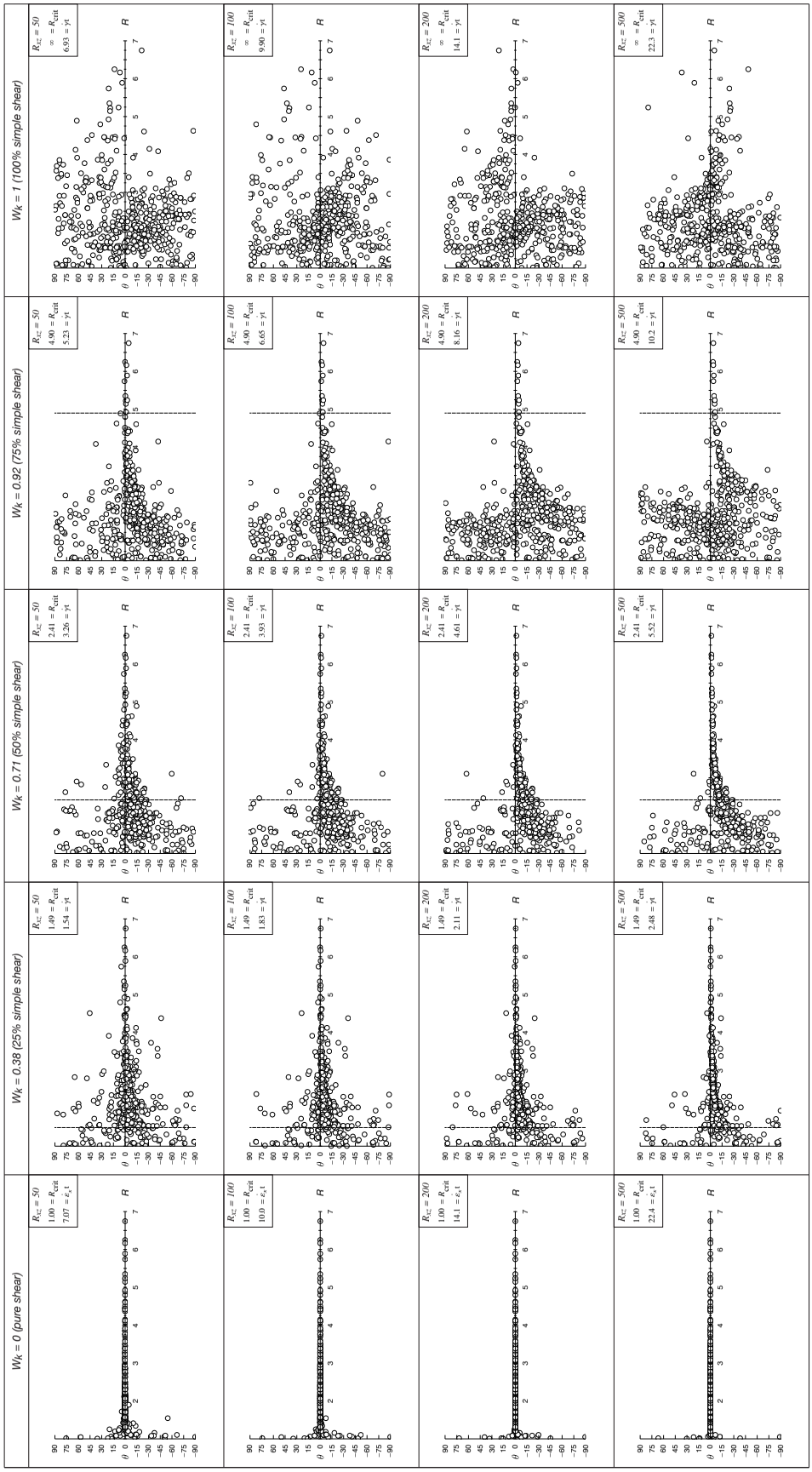

FIGURE 1.9. *continued.*

modeled, on the order of $R_{XZ} = 500$. Therefore, by the time moderate strains are reached in this flow, nearly all clasts within ∼22% of R_{crit} have rotated to within ∼10 degrees of the flow plane and will remain close to this orientation until large finite strains accumulate.

The reason for this behavior is clearly seen in the rotation rate vs. orientation curves (Fig. 1.5c–e). The normalized rotation rate of clasts with R near R_{crit} is such a small fraction of the applied shear strain rate, particularly in orientations near the extensional flow apophysis, that very high shear strains are necessary for clasts to rotate away from the flow plane (cf. Marques and Coelho, 2003).

1.6 Discussion

1.6.1 Model predictions

The numerical model presented here of evolving clast orientation distributions for steady flows of variable vorticity provides insight into the first-order behavior of natural systems during progressive deformation. The model allows direct comparison of the effects of progressive deformation for a steady flow and of increasing simple shearing component for viscous flows at constant strain states. Our results confirm previous conclusions (Masuda et al., 1995; Bailey et al., 2007; Mulchrone, 2007) that clast-based kinematic vorticity gauges may aid in discriminating pure and simple shear-dominated flows. We also found that large clast populations with a large range of clast aspect ratio are required for a reliable estimate of R_{crit}. This point has received little attention in the recent literature and will be discussed further below.

Pure shear-dominated flows

Our results indicate rather high strains are required to identify low W_k flows due to the relatively slow rotation of clasts with $R \geq 2$, particularly when they have initial orientations at moderate to high negative angles to the flow plane. Even in these strongly pure shear-dominated flows, relatively high strains (e.g., $1 \leq \dot{\gamma}t \leq 2$) are required to rotate clasts above R_{crit} into their stable orientations subparallel to the flow plane (see e.g., Ghosh and Ramberg, 1976, their figs. 9–13). For the modeled pure shear flow, elongate clasts tend to reach the flattening (foliation) plane at the lowest R_{XZ} values, but finite strains on the order of $> 20 : 1$ appear necessary for the majority

of clasts to reach their stable orientation. Similarly, visual estimates of R_{crit} for the $W_k = 0.38$ flow tend to produce an overestimate of the applied vorticity for all modeled strain states (Fig. 1.9). Visually estimated R_{crit} for this flow appears to lie between 2 and 3 for much of the deformation history, even for strain ratios approaching 500:1. This may be one contributing factor to the W_k = 0.65–0.75 results obtained from samples interpreted to have experienced pure shear-dominated flow (e.g., Bailey et al., 2007).

Simple shear-dominated flows

Clast orientation distributions closely resembling those expected for lower W_k flows are predicted for high W_k flows, even at low finite strain (Fig. 1.9). Here clasts of all aspect ratios rotate slowly in orientations subparallel to the flow plane so high strains must accumulate to rotate these grains from this orientation. Greater strains are needed for higher aspect ratio clasts, even though they are unstable in the flow (Figs. 1.9–1.11). The visually estimated R_{crit} of the $W_k = 0.92$ flow model

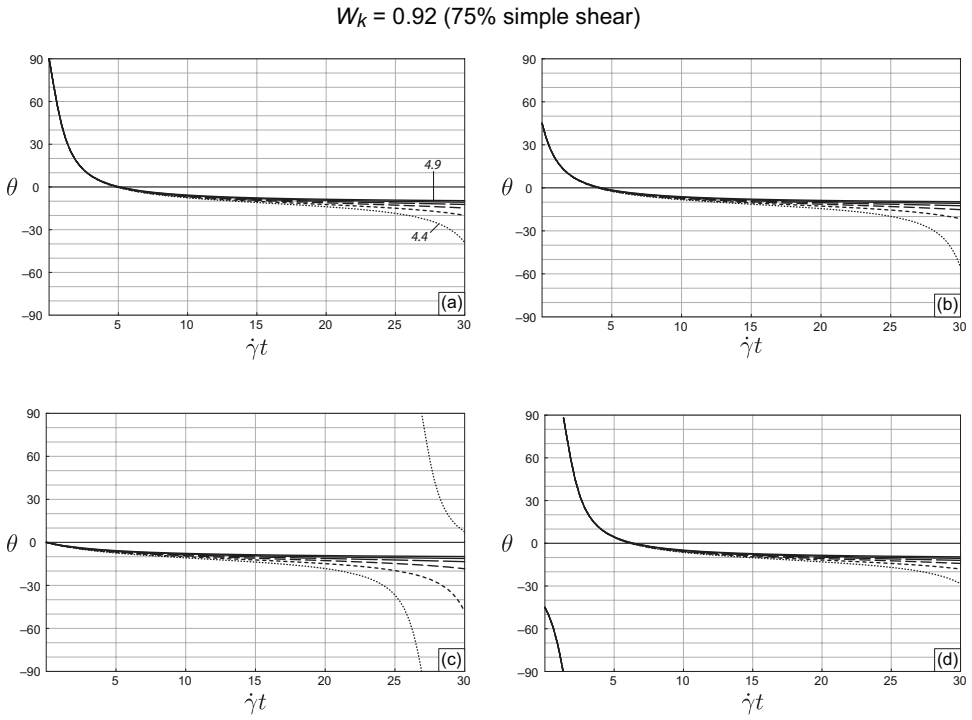

FIGURE 1.10. Orientation (θ) of clast long axis (cf. Fig. 1.3) vs. simple shear component ($\dot{\gamma}t$) for a flow of $W_k = 0.92$. Aspect ratios of $R = 4.4, 4.5, \ldots, 4.9$ shown (i.e., clasts within ~10% of R_{crit}). Length of dashes in pattern increase with increasing R; some labels omitted for clarity. Initial clast orientations of (a) +90 degrees, (b) +45 degrees, (c) 0 degrees, and (d) −45 degrees.

at high strain ($R_{XZ} > 20$) is ~ 3–3.75, corresponding to a W_k of 0.8–0.87 (Fig. 1.9). This is a

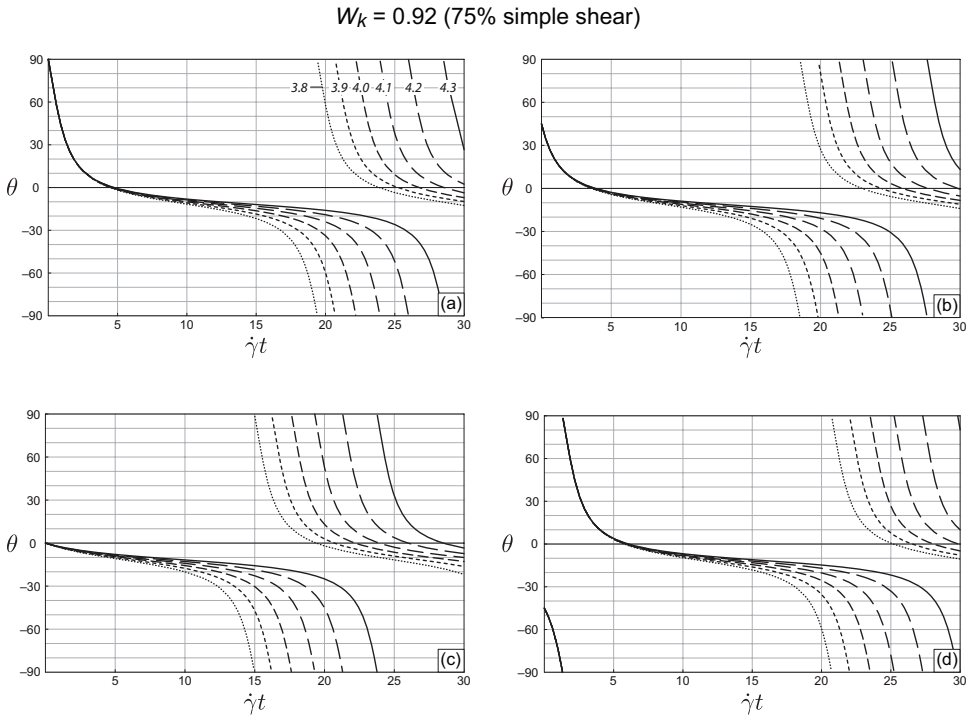

FIGURE 1.11. Orientation (θ) of clast long axis (cf. Fig. 1.3) vs. simple shear component ($\dot{\gamma}t$) for a flow of $W_k = 0.92$. Aspect ratios of $R = 3.8, 3.9, \ldots, 4.3$ shown (i.e., clasts within ∼22–10% of R_{crit}). Length of dashes in pattern increase with increasing R. Initial clast orientations of (a) +90 degrees, (b) +45 degrees, (c) 0 degrees, and (d) −45 degrees.

significant underestimation of the simple shearing component of flow (16–8%). The lower bound on visual estimates of the $W_k = 0.71$ flow may also yield underestimates on the applied vorticity of the same order ($\sim 10\%$) at high strain. Notice that this range of visually estimated W_k values are in agreement with results reported from many studies, even if higher W_k estimates were obtained for the same samples using different methods. We suspect that pseudostable behavior of clasts with $R < R_{\text{crit}}$, particularly in simple shear-dominated flows, may be another potential cause of the ubiquitous 0.65–0.75 W_k estimates from natural rocks. Underestimations of the simple shearing component of the magnitude estimated here, propagated through calculations of shear zone-parallel stretch, may yield substantial errors that impact interpretations relating the role of general shear flow to deformation-driven exhumation of plastically deformed rocks.

1.6.2 Application to naturally deformed rocks

Clearly, a critically important factor regarding the reliability of the rigid grain technique is the existence of a population of grains with $R > R_{\text{crit}}$. For example, samples must have a population of grains with $R > 3$ for effective discrimination of flows with $W_k > 0.8$ (Fig. 1.6). Results

from our own analyses, complimented by a brief examination of published analyses (e.g., Xypolias and Koukouvelas, 2001; Law et al., 2004; Jessup et al., 2006, 2007; Bailey et al., 2007; Johnson et al., 2009; Thigpen et al., 2010), unfortunately reveal that many natural rocks lack a significant population of suitable grains to discriminate high vorticity flows. For example, examination of the 76 mylonitic rocks from which we derived the aspect ratio distribution for our initial population, revealed that approximately 5% (779 of 14 959 clasts) have aspect ratios greater than $R = 4$ (Fig. 1.7). This value is consistent with other published studies. Such a small fraction of high aspect ratio grains in naturally deformed rocks indicates that flows with more than ∼60–70% simple shearing component are not generally identifiable by the rigid grain method.

We suggest that a lack of high aspect ratio grains may be yet another contributing factor to the overwhelming 0.65–0.75 W_k estimates for naturally deformed rocks obtained from clast-based techniques. Our experience suggests that for natural samples, clasts with $R < 3$ are abundant while grains with $R > 4$ are much more uncommon. Uncritical use of such naturally-limited datasets will tend to produce underestimates of W_k for natural mylonites (assuming they experience moderate to high vortical flows). We suspect that it is unrealistic to expect to identify flows with $W_k > 0.85$, and discriminating flows with this high of a simple shearing component is likely only possible under ideal circumstances.

Example

We present a brief example illustrating some limitations of the rigid grain technique by examining in more detail samples from the Rongbuk valley, Everest massif, originally presented by Law et al. (2004). We are primarily interested in the influence variable matrix strains and variable vorticity values have on the theoretical orientation distribution of porphyroclasts. We will examine the impact of finite strain estimates that vary over two orders of magnitude (R_{XZ} ∼2–250). Both the rigid grain and R_{XZ}/β techniques have been applied to several of the same samples (see Law et al., 2004, Table 1, samples ET08 and ET12–ET14). Rigid grain analyses applied to these rocks resulted in W_m estimates in the range of 0.67–0.85, (mean of 0.76). Here we use the notation W_m to indicate the measured vorticity was not likely an instantaneous quantity. Application of the R_{XZ}/β method to the same rocks, however, yielded W_m estimates in the range 0.78–0.94 (mean of 0.87), providing an upper bound on flow vorticity during mylonitization. We will show that this vorticity range

is indistinguishable by the rigid grain method, and that large differences in kinematics of simple shear-dominated flows are predicted to be difficult to distinguish using rigid grain analysis.

Minimum strains for these rocks of $R_{XZ} \approx 2$–3 have been inferred from aspect ratios of dynamically recrystallized quartz aggregates surrounded by mica films (Law et al., 2004). At these low matrix strains most grains above R_{crit} have not rotated into their stable orientations (cf. predictions for all flows at similar strains in Fig. 1.9). It is not until matrix strains of ~10–12 that clast populations resembling those observed begin to emerge from our model (Fig. 1.12a, b; Law, in preparation). Interestingly, matrix strains of this magnitude are near the maximum compatible with constraints on angle β determined from optically measured quartz *c*-axis fabrics on reconnaissance samples published by Law et al. (2004). Even at these moderate strain values, however, predictions for the $W_k = 0.76$ flow suggest that the 'true' vorticity may be overestimated in at least some natural rocks. Perhaps more important here than potential W_k underestimates is the similarity of the orientation distributions predicted for both $W_k = 0.76$ and $W_k = 0.87$ flows for a matrix strain ratio of 12:1 (Fig. 1.12a, b). At R_{XZ} values of 100–250, maximum estimates obtained

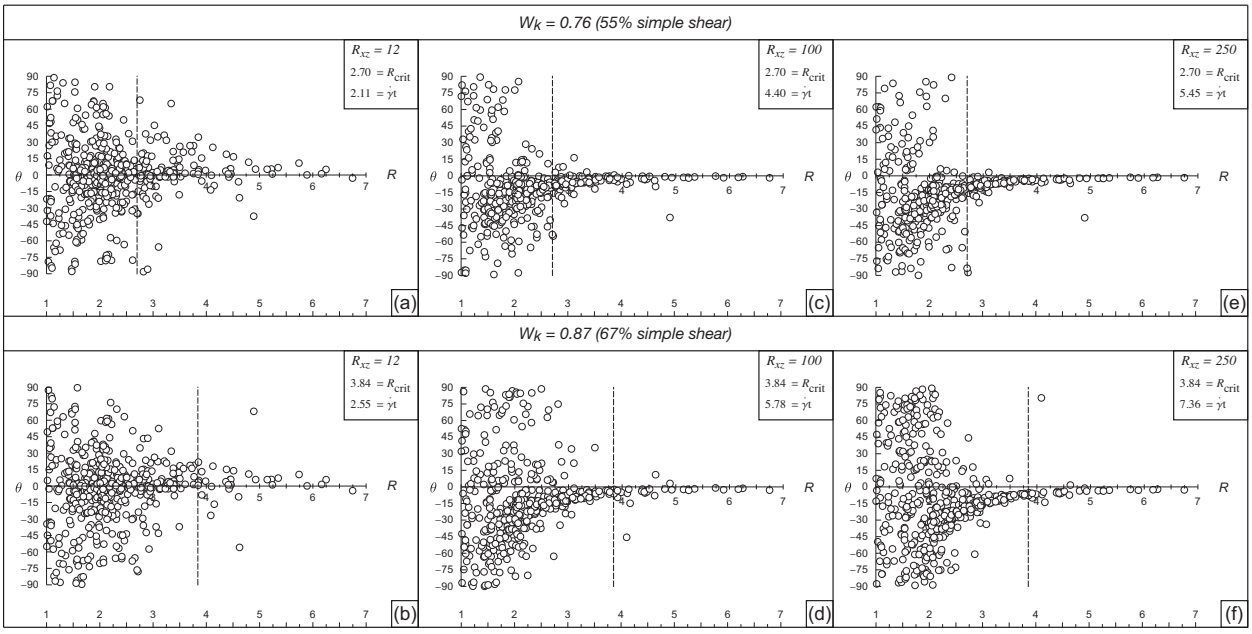

FIGURE 1.12. Model simulations of our original initial clast population for W_k values of 0.76 (upper panel) and 0.87 (lower panel) at matrix strains of (a, b) 12:1, (c, d) 100:1, and (e, f) 250:1. Note that clast orientation distributions are strikingly similar at the same matrix strains for these different W_k values. Thus, the $W_k = 0.76$ value obtained from measurements of the natural mylonites is a likely lower bound on the true flow vorticity, while higher W_k values for these rocks are also possible.

by assuming a penetrative vertical telescoping of isotherms below the South Tibetan Detachment,

clasts with $R \geq R_{\text{crit}}$ have rotated into positions approaching their stable orientation. However, even at these high strains the visual estimates of R_{crit} have not changed significantly and both flows modeled are predicted to produce virtually indistinguishable results (Fig. 1.12c–f).

The important observations here are: 1) for simple-shear-dominated flows such as this, finite strain ratios greater than $\sim 10:1$ appear necessary for clasts with $R \geq R_{\text{crit}}$ to closely approach their stable orientation. At lower matrix strains the rigid grain technique may overestimate the applied vorticity; and 2) similar clast orientation distributions are predicted for significantly different flows at matrix strains higher than $R_{XZ} \approx 10$. Thus, it appears that for simple shear-dominated flows—such as described for the Rongbuk valley—that by the time clasts rotate to near their stable position for moderate vorticity flows (e.g., $W_k \approx 0.7$ or so), strikingly similar orientation distributions are predicted for significantly higher vorticity flows (e.g., $W_k \geq 0.85$). There does not seem to be a way, solely by rigid grain analysis, to identify any flow of significantly greater vorticity than $W_k = 0.65$–0.75—*even though grains with* $R \geq R_{crit}$ *exist in the rocks.*

This example underscores the importance of applying multiple techniques to single appropriate samples, and of obtaining independent finite strain estimates for samples selected for rigid grain analysis to determine likely upper and lower bounds on flow vorticity. By combining different vorticity estimation techniques with strain data the two vorticity values estimated for the Rongbuk section are seen to be identical within the limitations of the rigid grain method, rather than incompatible.

1.7 Conclusions

Our numerical model employing Ghosh and Ramberg's (1976) analytic solutions for the re-orientation of ellipsoidal clasts suspended in a flowing Newtonian matrix indicate: 1) moderate to high matrix strains are required for clasts with $R \geq R_{\text{crit}}$ to rotate into their stable orientations—even for flows of low W_k. We cannot state a particular strain ratio that must be attained by a deformed rock to ensure successful application of the technique, however, because different flow types require different matrix strains for clasts with $R \geq R_{\text{crit}}$ to approach their stable orientation; 2) in simple shear-dominated flows, some clasts with $R < R_{\text{crit}}$ rotate into sub-parallelism with the flow plane and remain near this orientation until large matrix strains accumulate. The exact amount

of strain required to re-orient these pseudostable clasts is a function of their aspect ratio and flow vorticity; and 3) although the rigid grain technique may potentially discriminate pure- and simple shear-dominated strain paths, the restricted R range of natural clast populations and pseudostable behavior of clasts that exist in many rocks, limit the usefulness of the method for extracting high-quality, meaningful results for many flows, particularly when used as the sole vorticity estimation technique.

We suggest the main limitations regarding application of the rigid grain technique to natural rocks are: 1) a significant population of grains with $R > R_{\text{crit}}$ must exist in the sample for it to be useful; 2) high matrix strains must be reached, even in low W_k flows, for clasts to reach their stable orientation. This may cause overestimations of the applied vorticity for many low strain rocks; and 3) at high matrix strains, clast populations in moderate to high W_k flows tend to develop shape preferred orientations that closely resemble those expected for lower W_k flows. The first point is critical because there is no way to know, *a priori*, the kinematic parameters of an ancient flow—indeed, these are the data sought. If the clast population used to extract these parameters is inadequate the results will be biased. The second and third points may provide some insight into the ubiquitous 0.65–0.75 W_k values obtained from natural samples.

In many cases where the quartz *c*-axis fabric and rigid grain methods have been applied to the same sample the results are markedly different. Results obtained from the quartz *c*-axis fabric method often yield $W_k \geq 0.9$, whereas rigid grain results are significantly lower (e.g., Law et al., 2004; Sullivan, 2008; Johnson et al., 2009; Xypolias, 2009, 2010). If results from the quartz *c*-axis fabric method are indeed representative of much of the ductile flow history for a given rock volume, then this discrepancy may be due to: 1) the behavior of higher aspect ratio grains in high W_k flows at high strain; 2) a lack of grains above R_{crit}, or possibly a combination of both. The discrepancy may be amplified if other contributing factors such as a non-Newtonian rheology (ten Grotenhuis et al., 2002) or imperfect clast–matrix coupling is also a factor (Johnson et al., 2009).

In light of the model presented here it appears that Ghosh and Ramberg's (1976) equations that govern clast rotational behavior in a viscous medium—upon which the rigid grain technique is founded—predict that the method is *not* equally effective for all flows, particularly at high finite strain. In fact, it appears that most general shear flows continued long enough to develop moderate–high finite strain will tend to produce a clast orientation distribution that will yield a

visual estimate of the critical aspect ratio that suggests approximately equal contributions of pure and simple shear components.

Acknowledgments

This paper presents part of the primary author's Ph.D. research. Thorough reviews by Paris Xypolias and an anonymous reviewer helped strengthen and focus the manuscript. Careful editorial handling of Cees Passchier is also appreciated. Funding for this research was provided by National Science Foundation grant EAR 0711207 to RDL.

References

Bailey, C.M., Eyster, E.L., 2003. General shear deformation in the Pinelano Mountains metamorphic core complex, Arizona. Journal of Structural Geology 25, 1883–1893.

Bailey, C.M., Polvi, L.E., Forte, A.M., 2007. Pure shear dominated high-strain zones in basement terranes. In: Hatcher, Jr., R.D., Carlson, M.P., McBride, J.H., Martinez Catalan, J.R. (Eds.), 4-D Framework of Continental Crust, vol. 200, pp. 93–108.

Bobyarchick, A.R., 1986. The eigenvalues of steady flow in Mohr space. Tectonophysics 122, 35 – 51.

Carosi, R., Montomoli, C., Rubatto, D., Visona, D., 2006. Normal-sense shear zones in the core of the Higher Himalayan crystallines (Bhutan Himalaya): evidence for extrusion? In: Law, R.D., Searle, M.P., Godin, L. (Eds.), Channel Flow, Ductile Extrusion and Exhumation in Continental Collision Zones, vol. 268, pp. 425–444.

Ghosh, S.K., 1987. Measure of non-coaxiality. Journal of Structural Geology 9, 111–114.

Ghosh, S.K., Ramberg, H., 1976. Reorientation of inclusions by combination of pure and simple shear. Tectonophysics 34, 1–70.

Grasemann, B., Stüwe, K., 2001. The development of flanking structures during simple shear and their use as kinematic indicators. Journal of Structural Geology 23, 715–724.

ten Grotenhuis, S.M., Passchier, C.W., Bons, P.D., 2002. The influence of strain localisation on the rotation behaviour of rigid objects in experimental shear zones. Journal of Structural Geology 24, 485–499.

Holcombe, R.J., Little, T.A., 2001. A sensitive vorticity gauge using rotated porphyroblasts, and its application to rocks adjacent to the Alpine Fault, New Zealand. Journal of Structural Geology 23, 979–989.

Hutton, D.H.W., 1970. A tectonic model for the emplacement of the main Donegal granite, NW Ireland. Journal of the Geological Society of London 139, 615–631.

Jessup, M.J., Law, R.D., Searle, M.P., Hubbard, M.S., 2006. Structural evolution and vorticity of flow during extrusion and exhumation of the Greater Himalayan Slab, Mount Everest Massif, Tibet/Nepal: implications for orogen-scale flow partitioning. In: Law, R., Butler, R., Holdsworth, R., Krabbendam, M., Strachan, R. (Eds.), Channel Flow, Ductile Extrusion and Exhumation in Continental Collision Zones, vol. 268, pp. 379–419.

Jessup, M.J., Law, R.D., Searle, M.P., Hubbard, M.S., 2007. The rigid grain net (RGN): an alternative method for estimating mean kinematic vorticity number (W_m). Journal of Structural Geology 29, 411–421.

Johnson, S.E., Lenferink, H.J., Price, N.A., Marsh, J.H., Koons, P.O., West, Jr., D.P., 2009. Clast-based kinematic vorticity gauges: the effects of slip at matrix/clast interfaces. Journal of Structural Geology 31, 1322–1339.

Kanagawa, K., 1996. Simulated pressure fringes, vorticity, and progressive deformation. In: De Paor, D.G. (Ed.), Structural Geology and Personal Computers. Pergamon, vol. 15, pp. 259–283.

Law, R.D., 2010. Moine Thrust zone mylonites at the Stack of Glencoul: II – results of vorticity analyses and their tectonic significance. In: Law, R., Butler, R., Holdsworth, R., Krabbendam, M., Strachan, R. (Eds.), Continental Tectonics and Mountain Building: The Legacy of Peach and Horne, vol. 335, pp. 579–602.

Law, R.D., Searle, M.S., Simpson, R.L., 2004. Strain, deformation temperatures and vorticity of flow at the top of the greater Himalayan Slab, Everest Massif, Tibet. Journal of the Geological Society of London 161, 305–320.

Malvern, L.E., 1969. Introduction to the Mechanics of a Continuous Medium. Prentice Hall.

Marques, F.O., Coelho, S., 2003. 2-d shape preferred orientations of rigid particles in transtensional viscous flow. Journal of Structural Geology 25, 841 – 854.

Marques, F.O., Schmid, D.W., Andersen, T.B., 2007. Applications of inclusion behavior models to a major shear zone system: the Nordfjord-Sogn Detachment Zone in Western Norway. Journal of Structural Geology 29, 1622–1631.

Masuda, T., Michibayashi, K., Ohta, H., 1995. Shape preferred orientation of rigid particles in a viscous matrix: reevaluation to determine kinematic parameters of ductile deformation. Journal of Structural Geology 17, 115–129.

McKenzie, D., 1979. Finite deformation during fluid flow. Geophysical Journal of the Royal Astronomical Society 58, 115–129.

Means, W.D., Hobbs, B.E., Lister, G.S., Williams, P.F., 1980. Vorticity and non-coaxiality of progressive deformations. Journal of Structural Geology 2, 371–378.

Mulchrone, K.F., 2007. Shape fabrics in populations of rigid objects in 2D: Estimating finite strain and vorticity. Journal of Structural Geology 29, 1558–1570.

Passchier, C.W., 1986. Flow in natural shear zones. Earth and Planetary Science Letters 77, 70–80.

Passchier, C.W., 1987. Stable positions of rigid objects in non-coaxial flow–a study in vorticity analysis. Journal of Structural Geology 9, 679–690.

Passchier, C.W., 1988. Analysis of deformation paths in shear zones. Geologische Rundschau 77, 308–318.

Provost, A., Buisson, C., Merle, O., 2004. From progressive to finite deformation and back. Journal of Geophysical Research 109, doi:10.1029/2001JB001734.

Ramberg, H., 1975. Particle paths, displacement and progressive strain applicable to rocks. Tectonophysics 28, 1–37.

Simpson, C., De Paor, D.G., 1993. Strain and kinematic analysis in general shear zones. Journal of Structural Geology 15, 1–20.

Simpson, C., De Paor, D.G., 1997. Practical analysis of general shear zones using the porphyroclast hyperbolic distribution method: an example from the scandinavian caledonides. In: Sengupta, S. (Ed.), Evolution of Geological Structures in Micro- to Macro-scales. Chapman and Hall, pp. 169–184.

Sullivan, W.A., 2008. Significance of transport-parallel strain variations in part of the Raft River shear zone, Raft River Mountains, Utah, USA. Journal of Structural Geology 30, 138–158.

Talbot, C.J., 1970. The minimum strain ellipsoid using deformed quartz veins. Tectonophysics 9, 47–74.

Thigpen, J.R., Law, R.D., Brown, S.J., Lloyd, G.L., Cook, B., 2010. Deformation temperatures, vorticity of flow and strain symmetry in the loch eriboll mylonites, nw scotland: implications for the kinematic and structural evolution of the northernmost moine thrust zone. In: Law, R., Butler, R., Holdsworth, R., Krabbendam, M., Strachan, R. (Eds.), Continental Tectonics and Mountain Building: The Legacy of Peach and Horne, vol. 335, pp. 623–662.

Tikoff, B., Fossen, H., 1993. Simultaneous pure and simple shear: the unifying deformation matrix. Tectonophysics 217, 267–283.

Tikoff, B., Fossen, H., 1995. The limitations of three-dimensional kinematic vorticity analysis. Journal of Structural Geology 17, 1791–1784.

Tikoff, B., Fossen, H., 1999. Three dimensional reference deformations and strain facies. Journal of Structural Geology 21, 1497–1512.

Vissers, R.J.M., 1989. Asymmetric quartz *c*-axis fabrics and flow vorticity: a study using rotated garnets. Journal of Structural Geology 11, 231–244.

Wallis, S.R., 1992. Vorticity analysis in a metachert from the Sanbagawa Belt, SW Japan. Journal of Structural Geology 14, 271–280.

Wallis, S.R., 1995. Vorticity analysis and recognition of ductile extension in the Sanbagawa Belt, SW Japan. Journal of Structural Geology 17, 1077–1093.

Wallis, S.R., Platt, J.P., Knott, S.D., 1993. Recognition of syn-convergence extension in accretionary wedges with examples from the Calabrian arc and the eastern Alps. American Journal of Science 293, 463–495.

Xypolias, P., 2009. Some new aspects of kinematic vorticity analysis in naturally deformed quartzites. Journal of Structural Geology 31, 3 – 10.

Xypolias, P., 2010. Vorticity analysis in shear zones: A review of methods and applications. Journal of Structural Geology 32, 2072 – 2092.

Xypolias, P., Doutsos, T., 2000. Kinematics of rock flow in a crustal-scale shear zone: implications for the orogenic evolution of the southwestern Hellenides. Geological Magazine 137, 81–96.

Xypolias, P., Kokkalas, S., 2006. Heterogeneous ductile deformation along a mid-crustal extruding shear zone: an example from the external Hellenides (Greece). In: Law, R.D., Searle, M.P., Godin, L. (Eds.), Channel Flow, Ductile Extrusion and Exhumation in Continental Collision Zones, vol. 268, pp. 497–516.

Xypolias, P., Koukouvelas, I.K., 2001. Kinematic vorticity and strain patterns associated with ductile extrusion in the Chelmos shear zone (External Hellinides, Greece). Tectonophysics 338, 59–77.

Chapter 2

Strain memory of rigid inclusion shape fabrics—how sensitive are clasts to temporal vorticity changes?

Donald W. Stahr, III[1], Richard D. Law[1]

[1]*Department of Geosciences, Virginia Polytechnic Institute and State University, Blacksburg, VA, 24061, USA*

This article will be submitted to *Journal of Structural Geology* for publication.

Abstract

We model the development of shape preferred orientation (SPO) of a large population of two- and three-dimensional (2D and 3D) rigid clasts suspended in a linear viscous matrix deformed by superposed steady and continuously non-steady plane strain flows to investigate the sensitivity of clasts to changing boundary conditions during a single or superposed deformation events. The resulting SPO of the clast populations are compared to that developed by an identical initial population experiencing a steady flow of constant kinematic vorticity that reaches an identical finite strain state. Rotation paths of individual 3D triaxial inclusions suspended in a plane strain flow are complex. However, for a population of such clasts the simplification to a 2D model provides a good approximation to the final SPO for all investigated deformation paths. Predictions of shape fabric development for a large population of inclusions calculated using 2D models are qualitatively similar to the more complex 3D analysis and display the same limitations of techniques based on clast SPO commonly used as a quantitative kinematic vorticity gauge. Our model results from steady, superposed, and non-steady flow histories with a significant protracted pure shearing component at a wide range of finite strain are not significantly different than predictions for an identical initial population that experienced a single steady simple shear flow. We conclude that *individual* clasts respond instantaneously to changes in boundary conditions. However, in aggregate, SPO of a large population of rigid inclusions does not reflect the late-stage kinematics of deformation, nor can it be considered a unique indicator of the 'mean' kinematic vorticity experienced by a deformed rock volume.

2.1 Introduction

There is currently renewed interest in quantitative predictions of the rotational behavior of both rigid and deformable clasts in a flowing matrix of Newtonian or other rheology (e.g., Ghosh et al., 2003; Marques and Coelho, 2003; Schmid and Podladchikov, 2004; Jiang, 2007a,b; Johnson et al., 2009; Li and Jiang, 2011; Mancktelow, 2011; Stahr and Law, 2011). Recent geological research has typically focused on the behavior of elliptical porphyroblasts and / or porphyroclasts in ductile high-strain zones, but clast orientation analyses have also been applied to aligned phenocrysts in igneous rocks (e.g., Bhattacharyya, 1966), rock fragments embedded in fault gouge (e.g., Cladouhos, 1999a,b), and cobbles in glacial till as quantitative markers of shear strain, kinematic framework, and / or tectonic boundary conditions in these settings (e.g., Glen et al., 1957; Hooyer and Iverson, 2000).

The quantitative theory of the rotational behavior of rigid ellipsoidal bodies suspended in a Newtonian matrix was first published by Jeffery over 90 years ago (Jeffery, 1922). Closed-form solutions to these equations only exist for special inclusion geometries or flow types (e.g., Jeffery, 1922; Gay, 1968), and due to the relative difficulty of numerically integrating Jeffery's equations

few structural geologists have examined predictions of the governing theory in detail. Consequently, only a general qualitative understanding of the theory's predictions seems to exist in much of the geological literature. In an effort to make the theory tractable for geologic applications, Ghosh and Ramberg (1976) were the first to apply rather strict assumptions to the system in order to develop analytic solutions that approximate the rotational behavior of a cylindrical inclusion in a 2-dimensional (2D) flow of monoclinic symmetry. This mathematical simplification spawned development of the rigid clast techniques of kinematic vorticity analysis whereby the aspect ratio and shape preferred orientation (SPO) of a population of inclusions are utilized as vorticity indicators (Passchier, 1986; Simpson and De Paor, 1993; Wallis et al., 1993).

Masuda et al. (1995) and Stahr and Law (2011) have shown that clasts do not behave as one would naively expect even for the original rather strict assumptions regarding clast orientation and 2D boundary conditions first described by Ghosh and Ramberg (1976). Additionally, several other numerical studies have recently examined predictions of clast behavior with relaxed assumptions relative to the original Ghosh and Ramberg (1976) 2D framework (e.g., Mulchrone, 2007; Johnson et al., 2009; Jiang, 2007b; Mancktelow, 2011). What has emerged from these forward modeling studies is the realization that clast SPO may not record the kinematics of a flowing rock mass as expected, and other complicating factors such as rheologic contrasts between inclusion and matrix or slip at the clast–matrix interface may influence development of inclusion SPO in a tectonite.

A brief literature review indicates results from rigid grain vorticity analyses are interpreted in at least two significantly different ways. Simpson and De Paor (1997), Bailey et al. (2004), and Sullivan (2008) interpreted results from rigid clast-based techniques as recording kinematics from only the waning stages of flow (equivalent to recording W_k of late flow increments), while Law et al. (2004), Jessup et al. (2007), and Xypolias (2010), among others, interpreted results from the same methods as yielding a meaningful average or 'mean' flow vorticity (i.e., rigid clast-based techniques record W_m in the sense of Passchier, 1988). The purpose of the present communication is to test the above hypotheses in simple plane strain flows with suspended 2- and 3D rigid inclusions by forward numerical modeling. We seek to address the above conflicting hypotheses regarding the rapidity of clast re-orientation in a flowing viscous matrix and determine if clast populations are more likely to integrate a large fraction of the ductile flow history or simply record late flow kinematics.

Ghosh and Ramberg's analytic expressions for inclusion re-orientation form the theoretical

basis for all clast-based techniques, so we begin by examining consequences of superposed and non-steady 2D flows for a population of non-interacting rigid clasts. We then extend the 2D analysis to investigate how a presumably more realistic population of randomly oriented 3D triaxial clasts impacts SPO development for identical isochoric, plane strain, monoclinic flows. The effect of 3D rigid clast rotation in simple monoclinic flows has been explored most recently by Jiang (2007b, 2012) and Li and Jiang (2011) for steady, simple shearing-dominated flows only (i.e., $W_k \geq 0.7$). Here we explore consequences of 3D initial clast orientation for both superposed deformations and largely pure shearing-dominated flow histories that follow a decelerating flow path similar to those inferred for some naturally occurring shear zones (e.g., Simpson and De Paor, 1997; Grasemann et al., 1999).

2.2 Kinematic Modeling

2.2.1 2D models

The kinematic model of Stahr and Law (2011) was modified to investigate clast SPO produced as a result of two scenarios: a) superposition of end-member pure and simple shear flows; and b) flow with continually changing parameters (i.e., flow with variable vorticity). These scenarios capture a range of deformation histories that may significantly impact the behavior of a large population of non-interacting rigid clasts and allow us to address the question of clast sensitivity to changes in flow boundary conditions (Fig. 2.1). All model flows terminate at an identical finite strain state. Analyses have been completed on flows maintained to finite matrix strain ratios (R_S) of approximately 18, 60, and 220. Stated equivalently, all deformation paths modeled result in an identical position gradient tensor ($\mathbf{F_f}$ of Passchier, 1988; $\mathbf{D}$ of Tikoff and Fossen, 1993). Thus, the 'mean' vorticity (W_m of Passchier, 1988) is identical for each flow, but the stretch and rotation history of material lines in each flow are significantly different.

The initial condition for our 2D models was derived by calculating the apparent aspect ratio for central sections through 300 triaxial clasts (those generated for our 3D models) and using these values as the inclusion axial ratio. By doing so we are effectively assuming that two clast symmetry axes lie in the vorticity normal surface (VNS) and the remaining axis parallels the vorticity vector (so its magnitude is immaterial). Thus, each clast is constrained to rotate about the vorticity vector

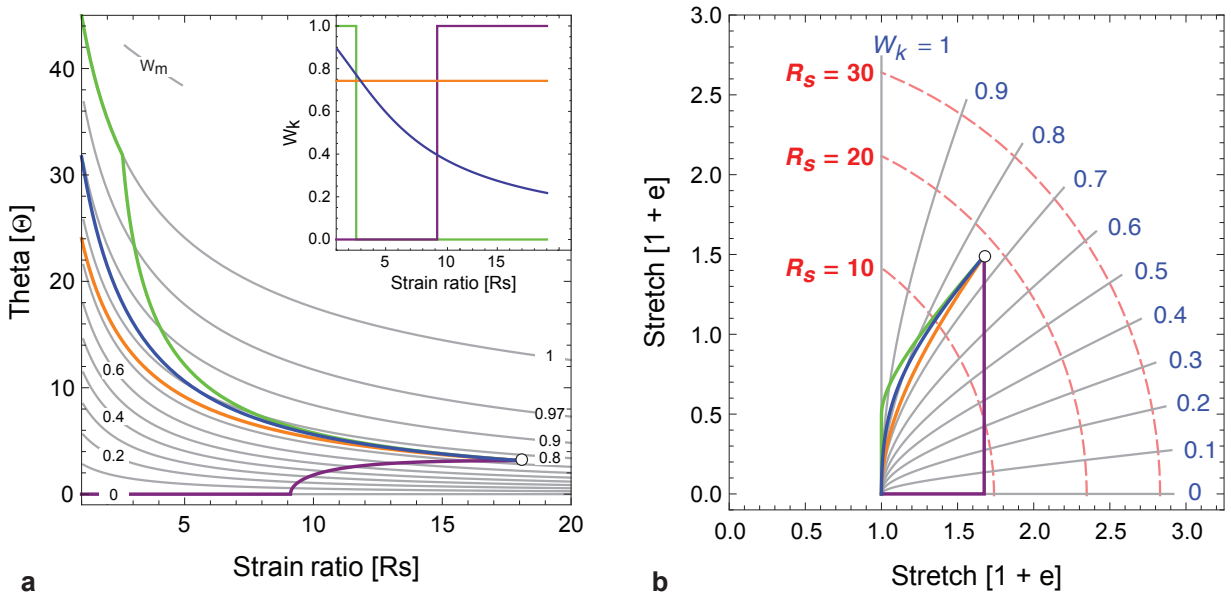

FIGURE 2.1. Modeled strain paths. (a) Strain paths shown in R_S/Θ space. Gray contours show evolution of finite strain ellipse for steady flows (i.e., $W_k \equiv W_m$). Inset plot depicts instantaneous kinematic vorticity number at each offset value (deformation increment) for the modeled flows in this investigation. (b) Strain paths representation in Mohr stretch space. Paths traced by center of off-axis Mohr circles for each path indicated, whereby the Mohr circle for strain is defined by components of position gradient tensor, $\mathbf{F_f}$, or $\mathbf{D}$, following each deformation increment. Mohr space is contoured for strain ratio (dashed red arcs) and steady flow paths (radiating solid gray curves). Strain paths depicted in parts (a) and (b) correspond to a matrix strain ratio of 18.06 (offset of 5 in the sense of Fossen and Tikoff, 1997) for each modeled deformation path considered in this paper. Modeled flows resulting in higher finite strain states (offsets of 10 and 20) not shown.

in such a way that the pitch of its longest axis on the VNS may vary, but the clast aspect ratio remains constant.

2D superposed flows

We have chosen to model two distinct superposed flows constructed by application of simple and pure shear end-members:

Path 1 Simple shear followed by pure shear; and

Path 2 Pure shear followed by simple shear.

Combinations of end-member flows are easily understood and provide a useful bound for the non-steady sub-simple shear deformation considered next.

2D non-steady flow

The model used to approximate non-steady flow is perhaps more accurately described as an instantaneously steady flow with continuously varying boundary conditions that approximates a flow with smoothly varying velocity gradient tensor components. The model used is an extension of the minimum strain path of Fossen and Tikoff (1997) to an offset of 20 by incremental offsets of 0.1 (i.e., total offset accomplished after 200 incremental strain steps); see Fossen and Tikoff (1997) for a detailed discussion of the minimum strain path. Each offset was specified and the W_k value that minimized the finite strain for that increment was determined (Fig. 2.2). The minimum strain path begins as a largely non-coaxial deformation (first increment of deformation has a W_k value of 0.89), but rapidly becomes dominated by pure shearing flow. This deformation path was chosen because: a) minimizing strain at every increment during a deformation event puts restrictions on the non-steady strain paths possible that produce a given finite strain state; and b) its resemblance to inferred changes in boundary conditions in some natural high-strain zones (e.g., Simpson and De Paor, 1997; Grasemann et al., 1999). The minimum strain path provides an easy way to determine if such protracted pure shearing-dominated deformation late in the flow history significantly affects the final clast orientation distribution.

2.2.2 3D models

Li and Jiang (2011) have recently demonstrated the importance of the 3D orientation of rigid clasts suspended in simple shear-dominated viscous flows (see also Bretherton, 1962; Willis, 1977; Freeman, 1985; Ježek, 1994; Ježek et al., 1994, 1996; Giorgis and Tikoff, 2004). We therefore wish to expand our 2D model to include an analysis of 3D clast re-orientation in superposed, steady, and non-steady flows. To accomplish this we modeled 3D monoclinic flows with zero stretching rate in the third dimension (i.e., $z-$axial direction in the external reference frame) to produce identical deformations on the VNS as those described above for 2D flow (cf. Li and Jiang, 2011). Monoclinic flow is generally assumed in applied kinematic vorticity analysis, and we are interested only in the differences predicted by generally oriented triaxial clasts for these simple flow geometries. Modeling results for triaxial inclusion populations are shown as both lower-hemisphere, equal-area projections of clast symmetry axis orientations and as clast aspect ratio vs. orientation (R–ϕ)

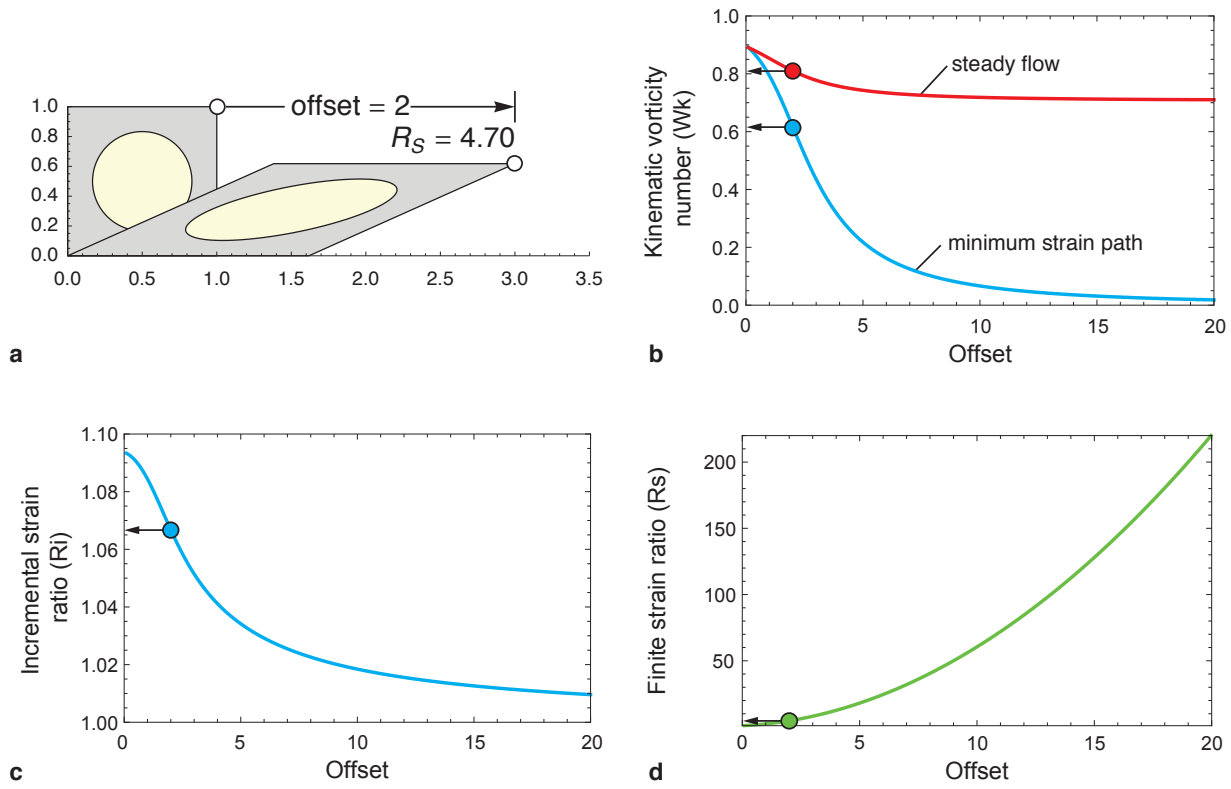

FIGURE 2.2. Details of minimum strain path (extended from Fossen and Tikoff, 1997). (a) Geometry of a particular finite strain state of interest, in this case an offset of 2, corresponding to a strain ratio (R_S) of 4.70. (b) Plot indicating identical strain state may be produced by very different deformation paths. Reference deformation in (a) indicated by red and blue circles on steady and non-steady flow curves, respectively. A steady flow of the *single* W_k value indicated on curve achieves the prescribed offset, $W_k = 0.82$ for particular case in (a). A deformation that minimizes finite strain at every instant assumes *all* W_k values for each incremental offset to achieve a given strain state, but its mean vorticity number W_m is identical to the steady flow that produces an identical offset. Here, to achieve an offset of 2, flow conforming to the minimum strain path *begins* with $W_k = 0.89$ whereas the flow *ends* with $W_k = 0.62$. The unique mean vorticity number for this deformation is of course $W_m = 0.82$. (c) and (d) indicate incremental strain ratio for intermediate steps of the minimum strain path, and finite strain for any prescribed offset, respectively. Note the W_m number of the steady flow that would accomplish a prescribed offset continuously decreases, asymptotically approaching a value of ~ 0.71 (equal contributions of pure and simple shear), whereas the minimum strain path approaches pure shearing flow at large offsets.

diagrams as observed on the VNS for direct comparison with observations of natural data.

We modeled 300 triaxial ellipsoidal clasts suspended in each flow (clast axes defined such that $a_1 \geq a_2 \geq a_3$). Clasts were chosen such that

$$10 \geq a_1 \geq 5, \qquad 5 \geq a_2 \geq 3, \qquad 3 \geq a_3 \geq 1,$$

and were given an initially uniform distribution in 3D geographical space (see Jiang, 2007b) (Fig. 2.3).

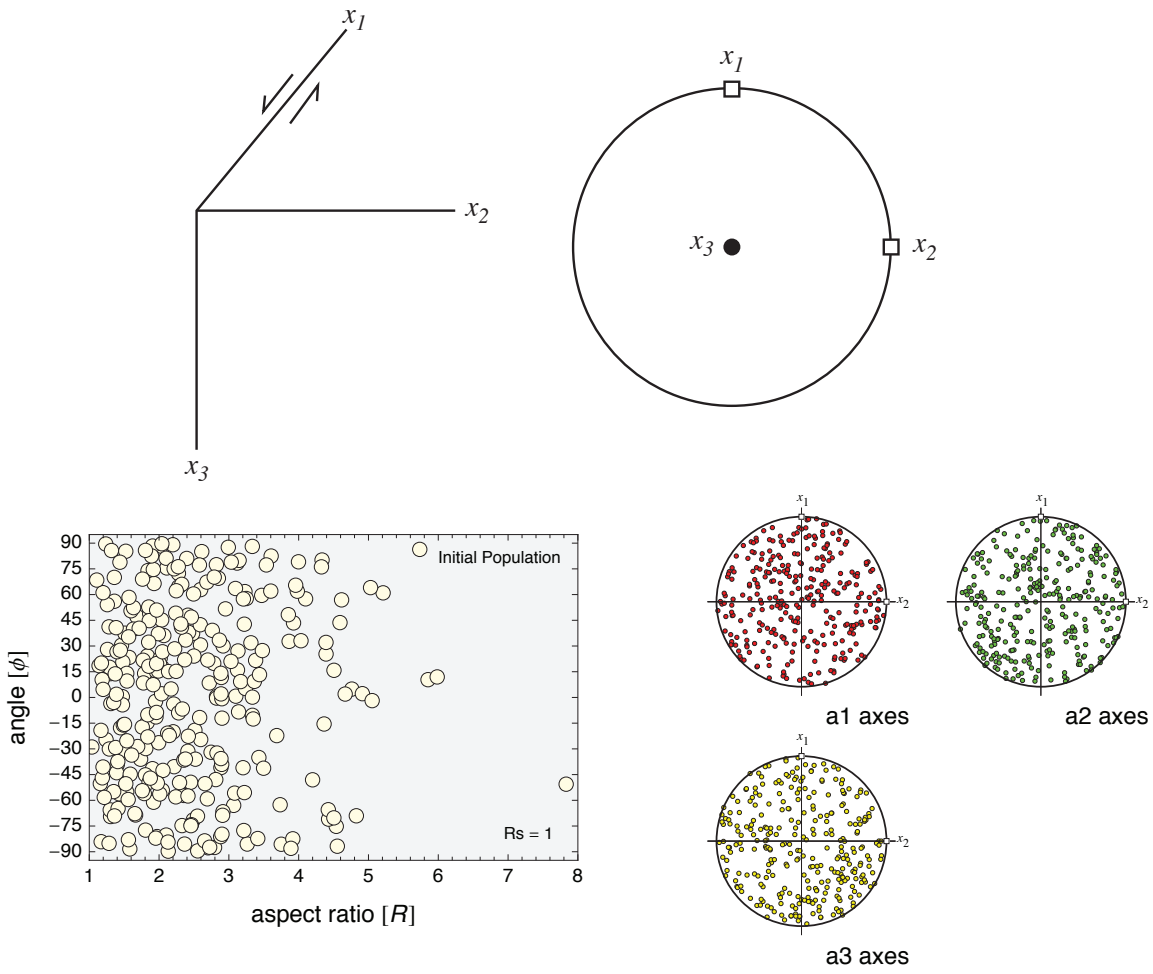

FIGURE 2.3. External reference frame and initial clast population. Vorticity vector parallels z coordinate axis for all plane strain flows considered in this work. R–ϕ diagrams constructed parallel to xy coordinate plane (i.e., XZ plane of finite strain). Below is a representation of apparent clast aspect ratios as observed on VNS and lower hemisphere, equal-area projections of initial orientations of clast symmetry axes used in 3D models. Clasts in 2D models assumed to have a true aspect ratio equal to their apparent value on the VNS. Inclusions are initially uniformly distributed in 3D geographical space.

3D steady and superposed flows

Closed-form solutions to Jeffery's equations of motion do not exist for the general 3D case, so one must use numerical techniques to integrate the governing system of coupled differential equations. We have chosen to use the Runge-Kutta method discussed by Jiang (2007b) to perform the numer-

ical analysis (see also Jiang, 2012). A critical aspect of numerical solution of Jeffrey's equations is the step size required to guarantee numerical stability of the calculations. We utilized a step size (δt) of 0.01 for each path segment to ensure numerical stability. Following the analysis of Jiang (2007b), given an angular velocity of 1 radian Myr^{-1}, the resulting error at each computational step of the fourth-order accurate Runge-Kutta ODE numerical solution method is on the order of 3.1×10^{-7} radians.

3D non-steady flow

Examination of Fig 2. reveals that the incremental strain magnitude continually decreases, as does the flow vorticity, as the minimum strain path progresses. In order to model this efficiently, we divided the path into 200 incremental offsets as above, but further divided each increment into 10 steps for numerical calculation. Using this approach, the step size, δt, varies from 7.951×10^{-3} to 1.740×10^{-5} from the beginning to ending deformation increments. As above, given an angular velocity of 1 Myr^{-1}, these δt values give rise to errors of 3.2×10^{-11} to 1.6×10^{-24} radians for each computational step.

2.3 Model Results

2.3.1 2D models

Individual clast rotation paths following Ghosh and Ramberg's analysis are relatively straightforward. Here, if $R < R_{\text{crit}}$, clasts will rotate continually forward with the sense of imposed vorticity, whereas, if $R > R_{\text{crit}}$ clasts may rotate forward or backward in the flow, depending on their initial orientation, until deformation ceases or they reach their stable orientation. The parameters in the equations describing clast rotation that determine a clast's final position in a flow are its initial orientation, flow vorticity, and finite matrix strain. Accordingly, individual clasts must to some extent be sensitive to the instantaneous boundary conditions of the flow in which they are suspended. Our modeling confirms that clasts will instantaneously respond to changes in flow regime by changing their sense or rate of rotation, or possibly both.

Clast orientation distribution patterns formed by a large population of non-interacting clasts appear only moderately sensitive to choice of deformation path in our simulations. In general, paths

that are close in strain ratio vs. orientation (R_S/Θ or Mohr stretch) space tend to produce similar clast SPOs at similar matrix strains. The path furthest from the others in this study (i.e., pure shear followed by simple shear) produces the most strikingly different clast SPO at arbitrary finite matrix strain. Part of the reason for this phenomenon is that the only stable orientation in simple shearing flow is that of a material line parallel to the extensional flow apophysis, so even objects with high aspect ratios are not stable during any increment of deformation and will continuously rotate. A second reason is because a large matrix strain is required to reorient the strain ellipse produced by a pure shear deformation into one with the dimensions and orientation of the desired finite strain state for our offsets of interest. Thus, Path 2 undergoes a moderate pure shear strain then a very high simple shear strain to produce the desired final state (with Θ at positive angles to the flow plane). This high simple shear strain tends to rotate any inclusion with long axis nearly parallel to the flow plane into positions potentially far removed from this orientation.

Animated evolutionary models constructed for the extended minimum strain path illustrate the instantaneous response of clasts to changes in boundary conditions (see supplementary material). Clasts suddenly change their rotation direction or sense (e.g., clockwise to counterclockwise) as the critical aspect ratio drops below the value of their particular aspect ratio during the progressive decelerating strain path. A similar phenomenon occurs, except with rotation sense reversed, for accelerating strain paths where the kinematic vorticity number continually increases during progressive deformation (not shown here). This tends to produce clast SPOs that are not necessarily indicative of late flow kinematics, and also do not necessarily represent true 'mean' flow vorticity, W_m, in the sense of Passchier (1988). In general, results for each flow with the exception of Path 2 (pure followed by simple shear) at all modeled matrix strains would likely be interpreted similarly (with a flow vorticity approaching equal contributions of pure and simple shear components) at arbitrary points along the deformation path. Results of our 2D models are reasonably consistent with published results from rigid grain analyses applied to natural rocks (Figs. 2.4, 2.5, 2.6).

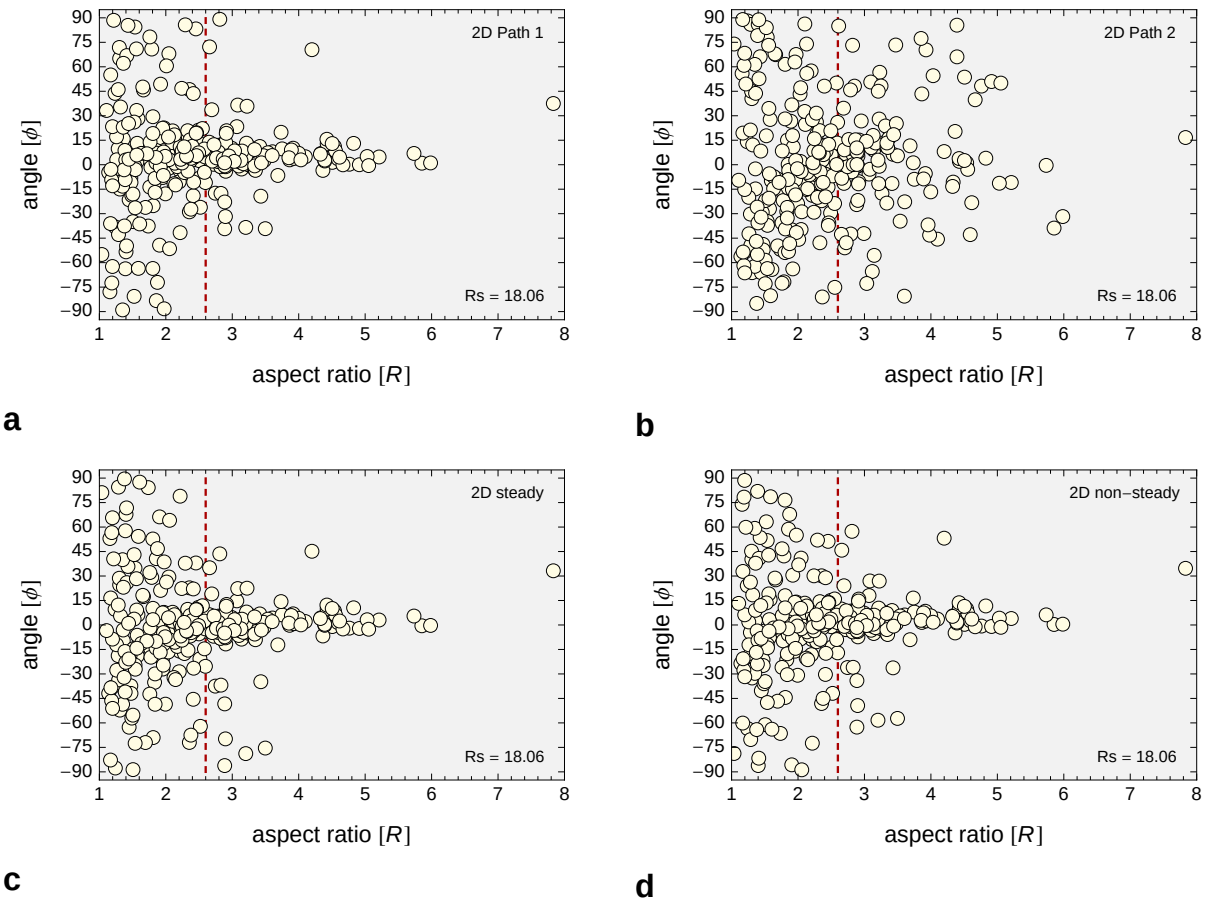

FIGURE 2.4. 2D model results for an offset of 5, $R_S \sim 18$. (a) Path 1; simple shear followed by pure shear. (b) Path 2; pure shear followed by simple shear. (c) Steady flow with $W_k = 0.74$. (d) Minimum strain path. Red dashed line indicates theoretical R_{crit} value for steady flow with kinematic vorticity number $W_m \equiv W_k = 0.74$.

2.3.2 3D models

Rotation path of an individual triaxial inclusion

The rotation path of generally oriented, individual spheroidal or ellipsoidal inclusions has received only modest attention in the geologic literature (e.g., Jeffery, 1922; Gay, 1968; Bretherton, 1962; Freeman, 1985; Jiang, 2007a), and modeled SPO development of a population of 3D clasts is even more rare (e.g., Reed and Tryggvason, 1974; Willis, 1977; Ježek, 1994; Ježek et al., 1996; Giorgis and Tikoff, 2004; Jiang, 2007a; Li and Jiang, 2011). The critical dependence of clast aspect ratio, initial orientation, and flow vorticity on clast behavior is briefly reviewed below to provide context for the following discussion of a large population of randomly oriented 3D inclusions.

The rotation path of a single triaxial clast is largely unpredictable even in the relatively simple

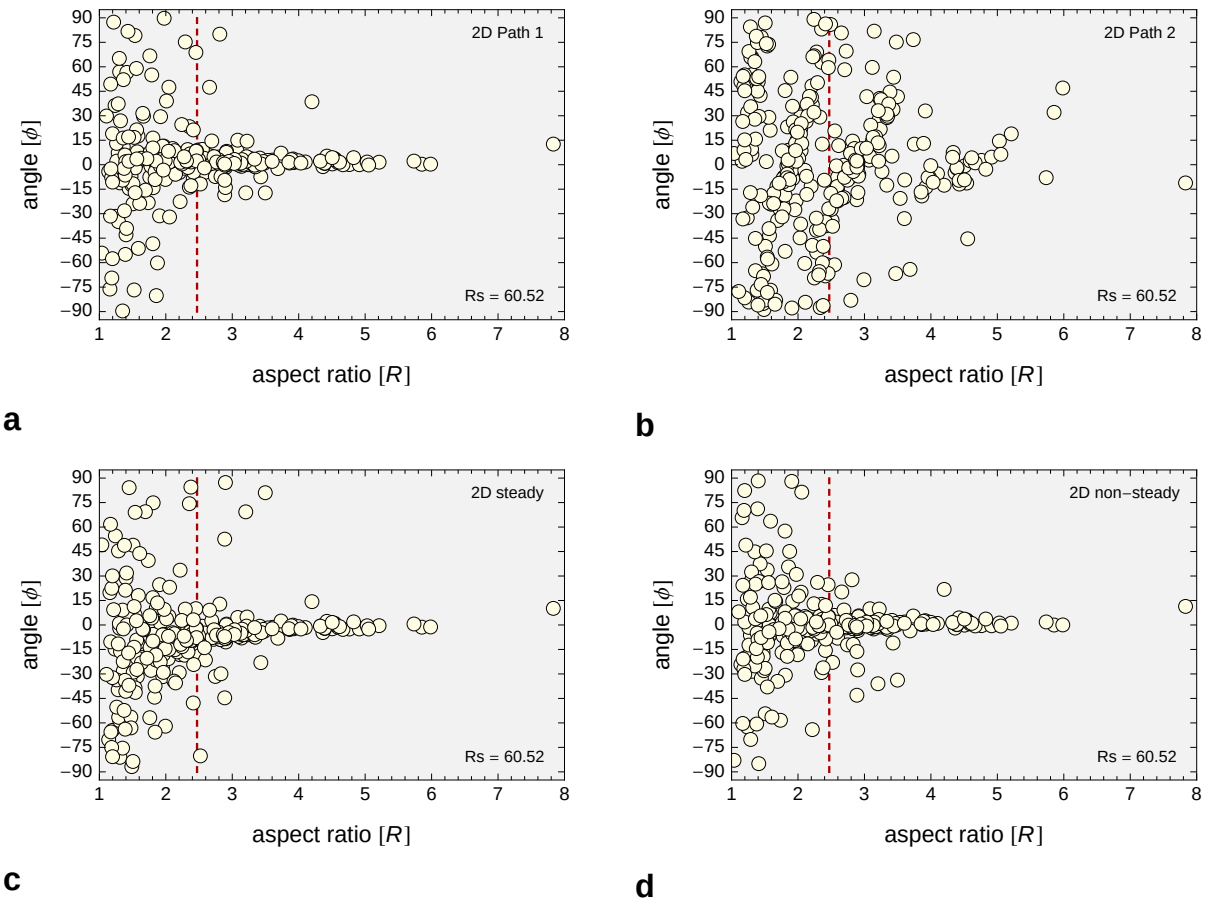

FIGURE 2.5. 2D model results for an offset of 10, $R_S \sim 60$. (a) Path 1; simple shear followed by pure shear. (b) Path 2; pure shear followed by simple shear. (c) Steady flow with $W_k = 0.72$. (d) Minimum strain path. Red dashed line indicates theoretical R_{crit} value for steady flow with kinematic vorticity number of $W_m \equiv W_k = 0.72$.

monoclinic plane strain flows considered here, but the ultimate stable orientations of higher aspect ratio clasts suspended in an arbitrary flow may be calculated. Each clast above a particular aspect ratio (a_1/a_3) has a stable orientation in a flow. The stable orientations of clasts in the plane strain flows considered here is such that their a_1 and a_3 axes lie in the plane of strain, and their intermediate a_2 axis rotates into alignment with the vorticity vector. Figures 2.7 and 2.8 demonstrate the above relationship and also the critical dependence of initial orientation on rotation path for a clast suspended in a given flow. Here we show the effect of different vorticity on the rotation path of a clast (4:2:1) with two different initial orientations. In the first case different boundary conditions ($W_k = 0.7$ vs. $W_k = 0.85$) lead to only slight modifications in the rotation path and an increase in the matrix strain required for the clast to closely approach its stable position. It is also clear from Fig. 2.7 that the clast is oriented with its a_1-axis close to the flow plane for a

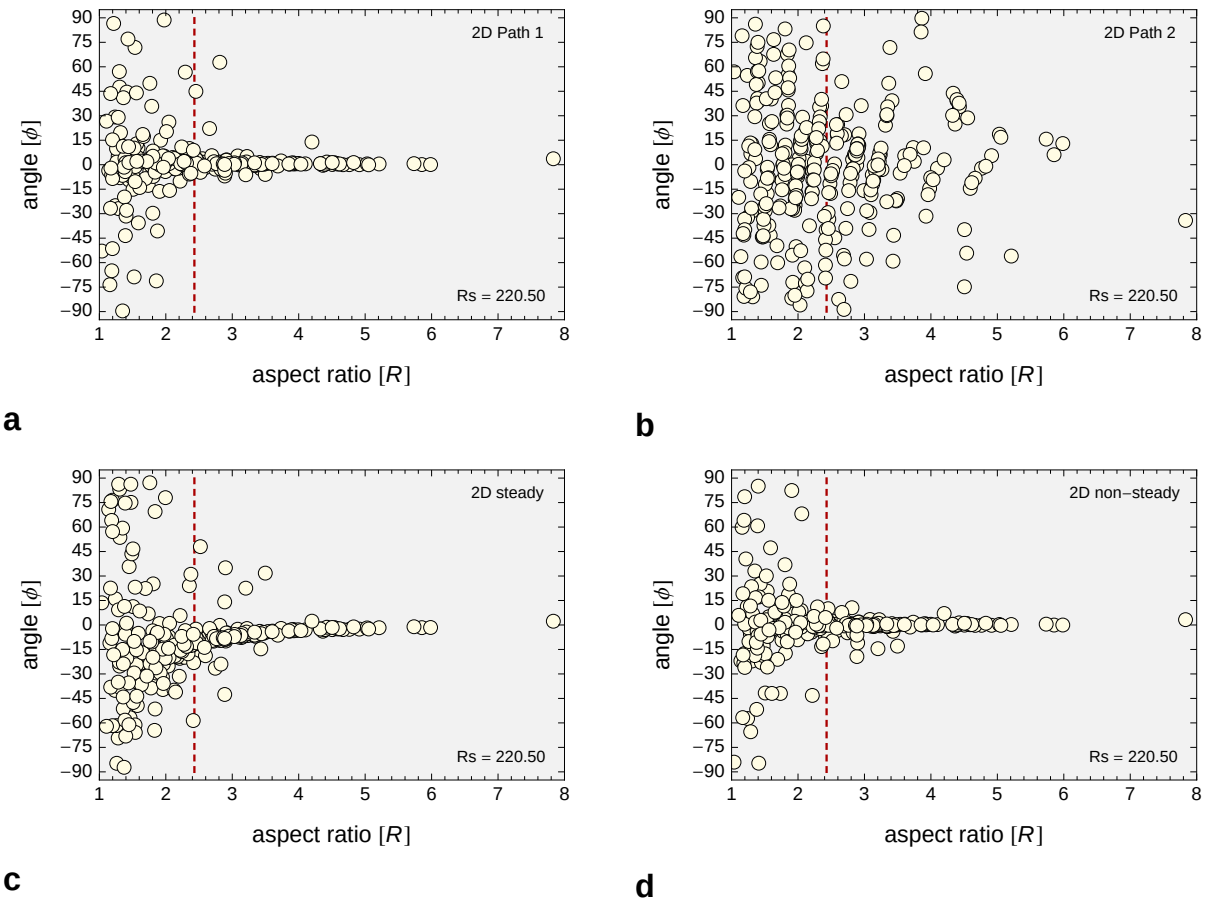

FIGURE 2.6. 2D model results for an offset of 20, $R_S \sim 220$. (a) Path 1; simple shear followed by pure shear. (b) Path 2; pure shear followed by simple shear. (c) Steady flow with $W_k = 0.71$. (d) Minimum strain path. Red dashed line indicates theoretical R_{crit} value for steady flow with kinematic vorticity number of $W_m \equiv W_k = 0.71$.

majority of the strain history. In contrast, Fig. 2.8 depicts a clast of identical axial dimensions but with a different initial orientation (one selected from our initial random 3D population). Here, small changes in the rotation component of the flow lead to dramatic modifications in the rotation path of the inclusion and lead to very large differences in the matrix strain required for the clast to rotate into its stable orientation. Again, as viewed on the VNS the clast's apparent long axis appears to lie close to the flow plane for a majority of the deformation history, however, in detail the inclusion's apparent aspect ratio on the VNS can be seen to increase then decrease and increase again, while the angle between the apparent clast long axis may rotate in a forward or backward sense during the deformation. The added complexity of an individual inclusion's rotation path may be viewed in animated evolutionary 3D models provided as supplementary material. For the particular cases shown in Figs. 2.7 and 2.8, the clast generally requires increasingly greater bulk strains to reach its

stable orientation for a higher rotational component in the flow. Thus, observation of orientations of apparent clast aspect ratios in R / ϕ plots as viewed on the VNS combined with equal-area projections of orientations of clast a_2 symmetry axes is a simple way to gauge how many clasts in a population have approached their stable orientation. See Giorgis and Tikoff (2004), Jiang (2007a) and Li and Jiang (2011) for a discussion of spheroidal or triaxial multi-clast populations of identical aspect ratio, respectively (Figs. 2.7, 2.8).

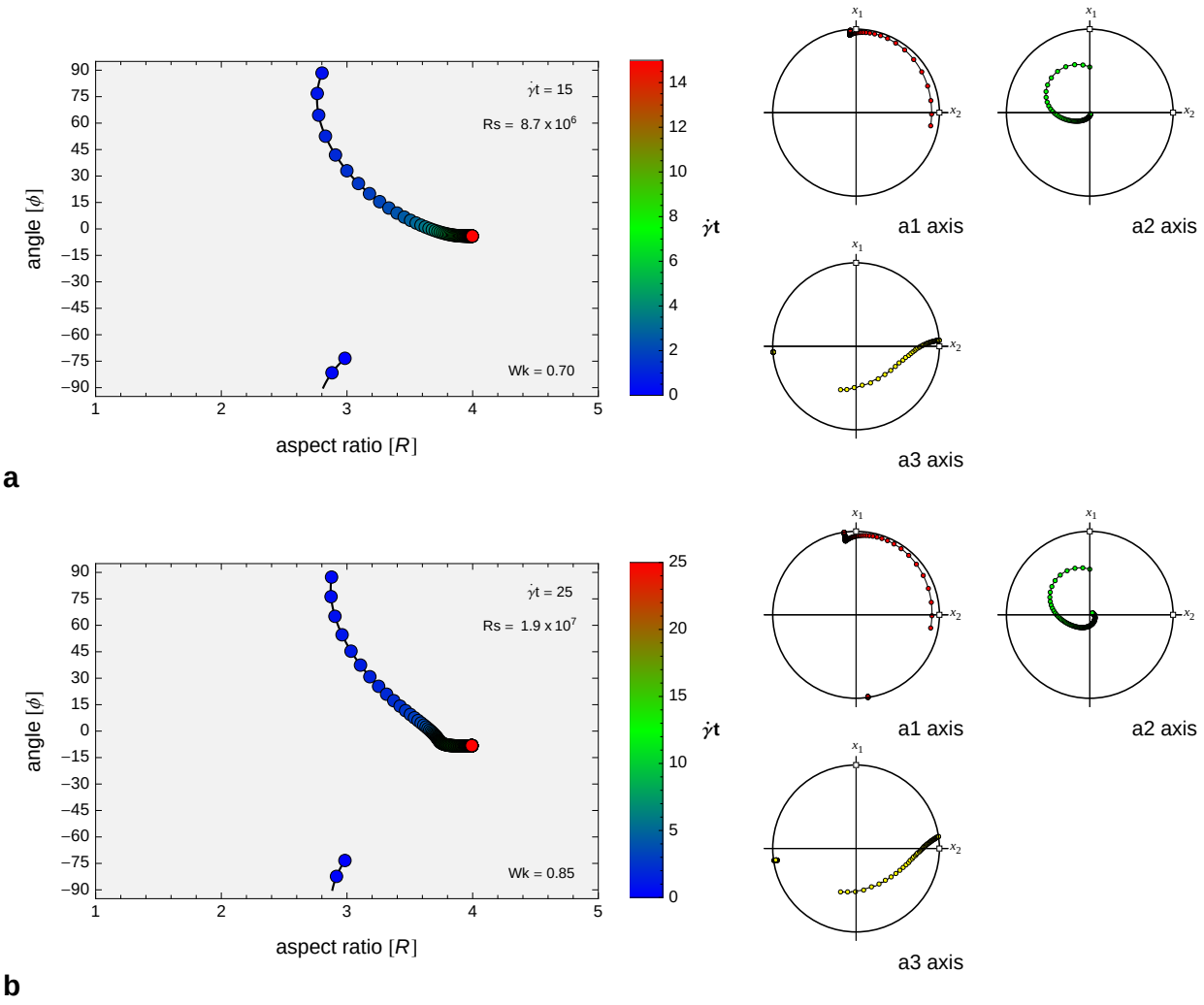

FIGURE 2.7. Calculated rotation path for triaxial ellipsoid with $a_1 : a_2 : a_3$ ratio defined as $4 : 2 : 1$ and initial orientation defined by a_1 axis plunging $10^\circ \rightarrow 100^\circ$, a_2 axis plunging $45^\circ \rightarrow 000^\circ$, and a_3 axis plunging $44^\circ \rightarrow 200^\circ$ (cf. Jiang, 2007a).

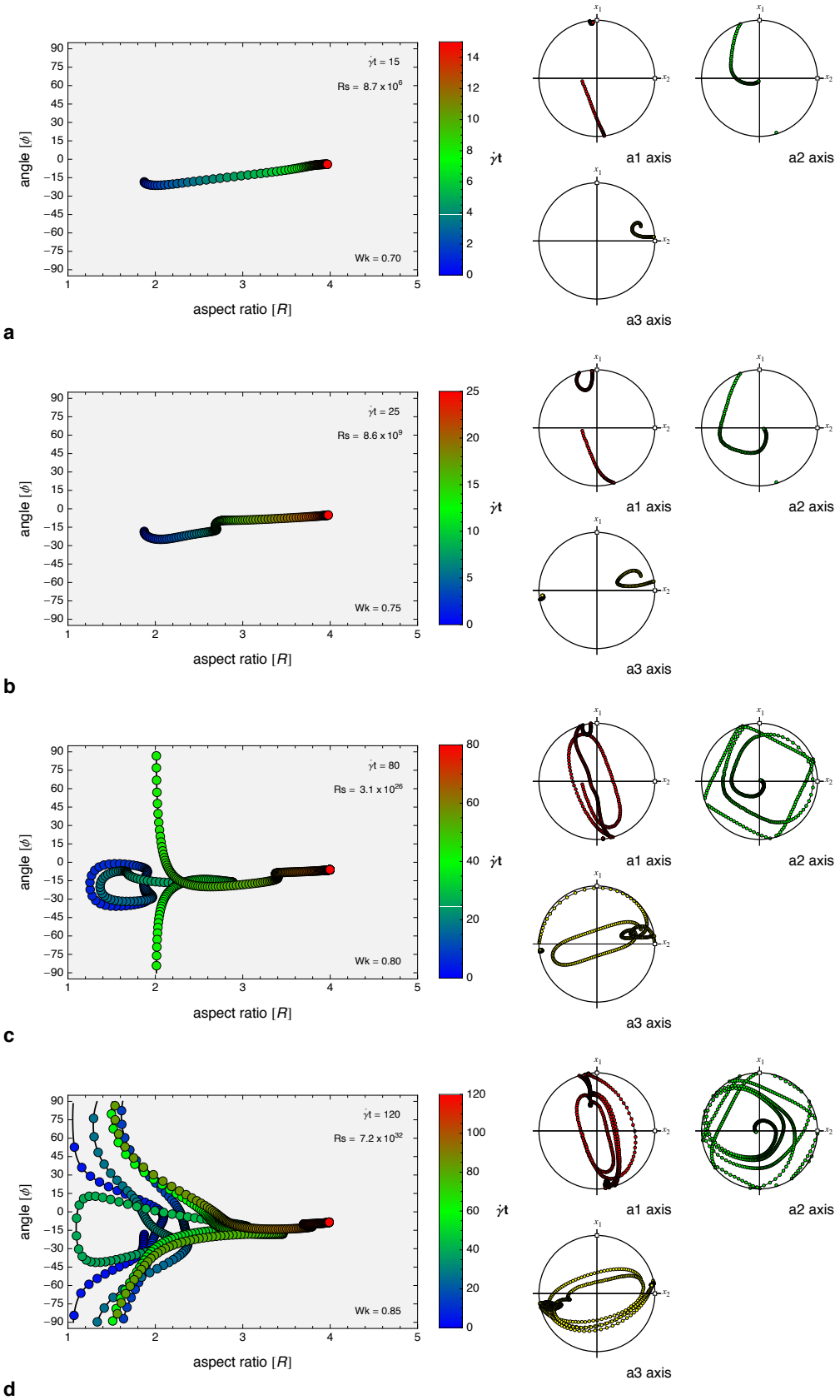

FIGURE 2.8. Calculated rotation path for triaxial ellipsoid with $a_1 : a_2 : a_3$ ratio defined as $4 : 2 : 1$ and initial orientation defined by a_1 axis plunging $69° \rightarrow 259°$, a_2 axis plunging $02° \rightarrow 163°$, and a_3 axis plunging $21° \rightarrow 072°$.

SPO of a population of 3D inclusions

From the above discussion it is clear that the rotational behavior of generally oriented 3D rigid inclusions is much more complex than the 2D Ghosh and Ramberg (1976) models can predict. As viewed on R / ϕ diagrams observed on the VNS during progressive deformation, clasts are not restricted to a single aspect ratio as they rotate in the flow; their apparent aspect ratio may decrease or increase during progressive deformation, depending on the 3D orientation of the inclusion. Additionally, clasts may appear to initially rotate forward with the sense of applied vorticity and subsequently rotate backward or against the vorticity, depending on their aspect ratio and orientation in the flow. This is true for the plane strain case considered here as well as more complex 3D flow types (e.g., Li and Jiang, 2011). Therefore, the final aspect ratio and orientation observed on a 2D section of any orientation through the deformed volume is a complex function of initial clast orientation, vorticity, and strain history.

For a given offset, our 3D models of a large clast population produce similar results, again with the exception of Path 2 (pure shear followed by simple shear). It is interesting to note that for our model strain Path 1 and the minimum strain path, both terminating with either a flow of very low W_k number or end-member pure shear, the majority of apparent long axes of clasts are oriented at very low angles to the flow plane as viewed on the VNS, but equal-area projections of their a_2-axes indicate that many are rather far removed from their actual stable orientation at the close of deformation.

Despite the complex rotational behavior of *individual* triaxial 3D inclusions, it is clear that details of the strain history do not have a significant influence on predicted final SPO of a *large population* of rigid clasts suspended in superposed or non-steady flows in the 3D models considered here, except perhaps for pure shear-dominated flows at the highest modeled matrix strains (e.g., $R_S \approx 220$). There appears to be little difference in model predictions for superposed flows and the minimum strain path at low- to moderate finite strains. The protracted pure shearing-dominated strain history only begins to become apparent in the SPO at rather high matrix strains ($R_S > 200$; (Figs. 2.9, 2.10, 2.11).

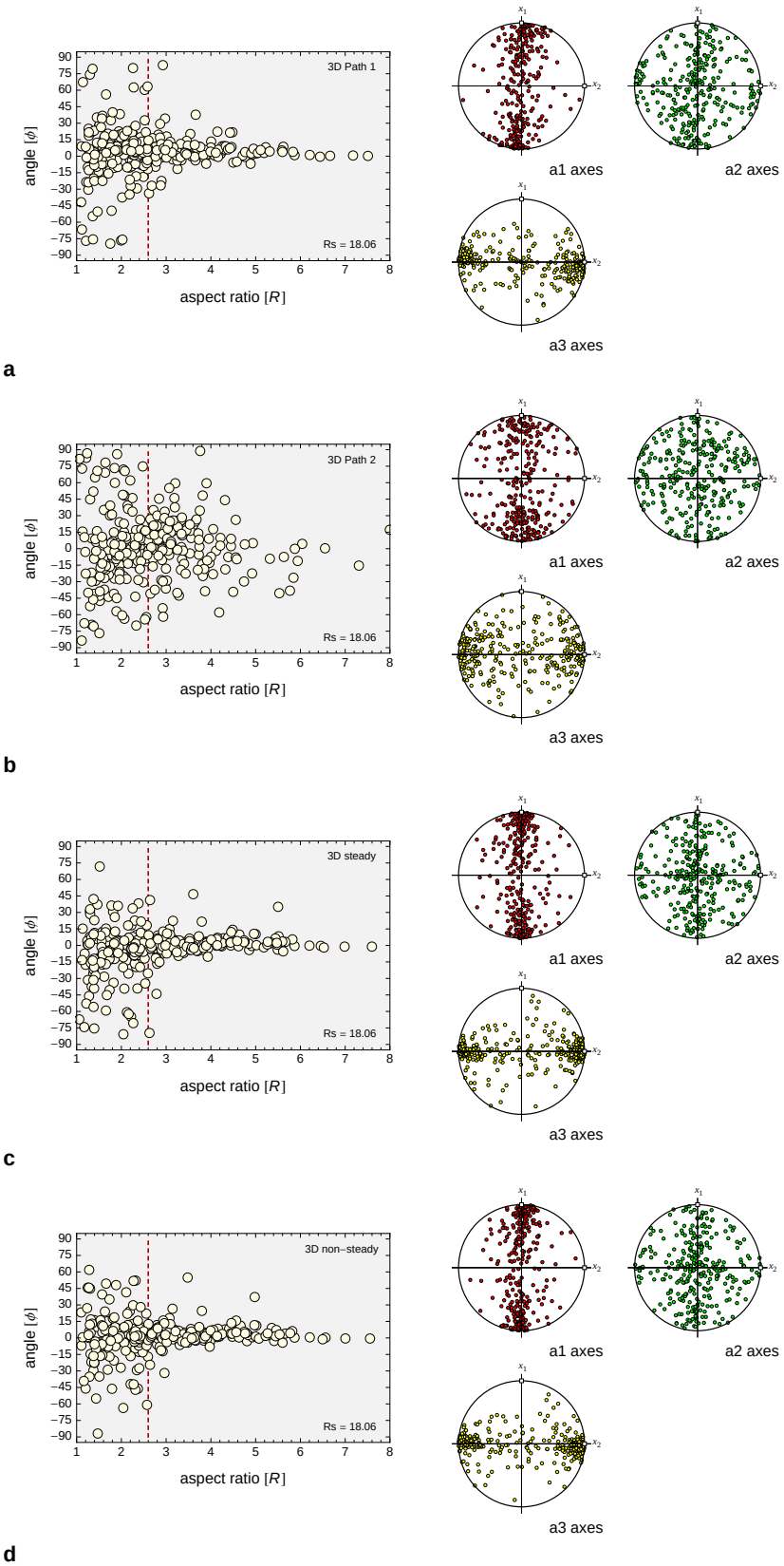

FIGURE 2.9. 3D model results for an offset of 5, $R_S \sim 18$. (a) Path 1; simple shear followed by pure shear. (b) Path 2; pure shear followed by simple shear. (c) Steady flow with $W_k = 0.71$. (d) Minimum strain path. Red dashed line indicates theoretical R_{crit} value for steady flow with kinematic vorticity number of $W_m \equiv W_k = 0.74$.

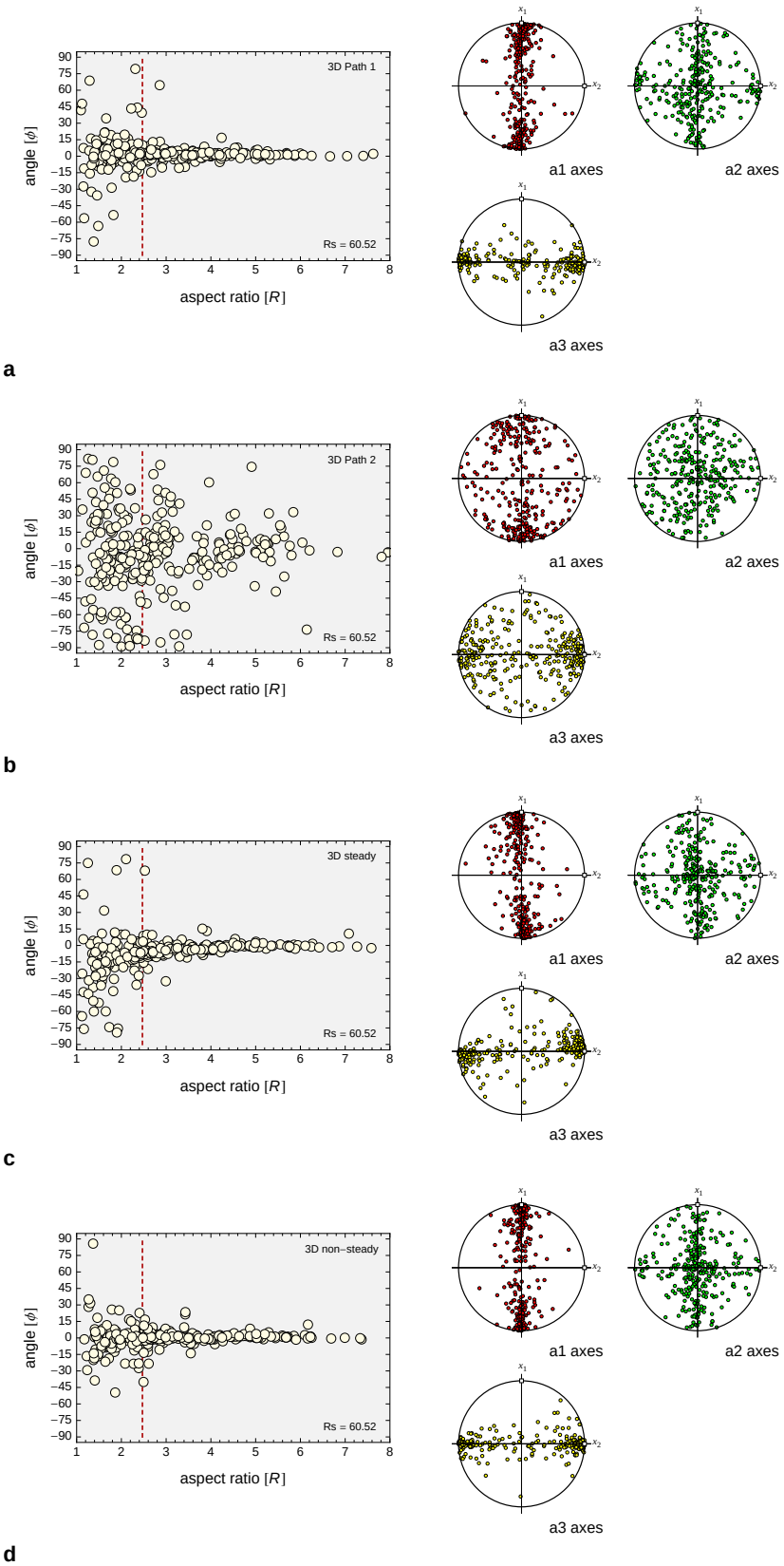

FIGURE 2.10. 3D model results for an offset of 10, $R_S \sim 60$. (a) Path 1; simple shear followed by pure shear. (b) Path 2; pure shear followed by simple shear. (c) Steady flow with $W_k = 0.71$. (d) Minimum strain path. Red dashed line indicates theoretical R_{crit} value for steady flow with kinematic vorticity number of $W_m \equiv W_k = 0.72$.

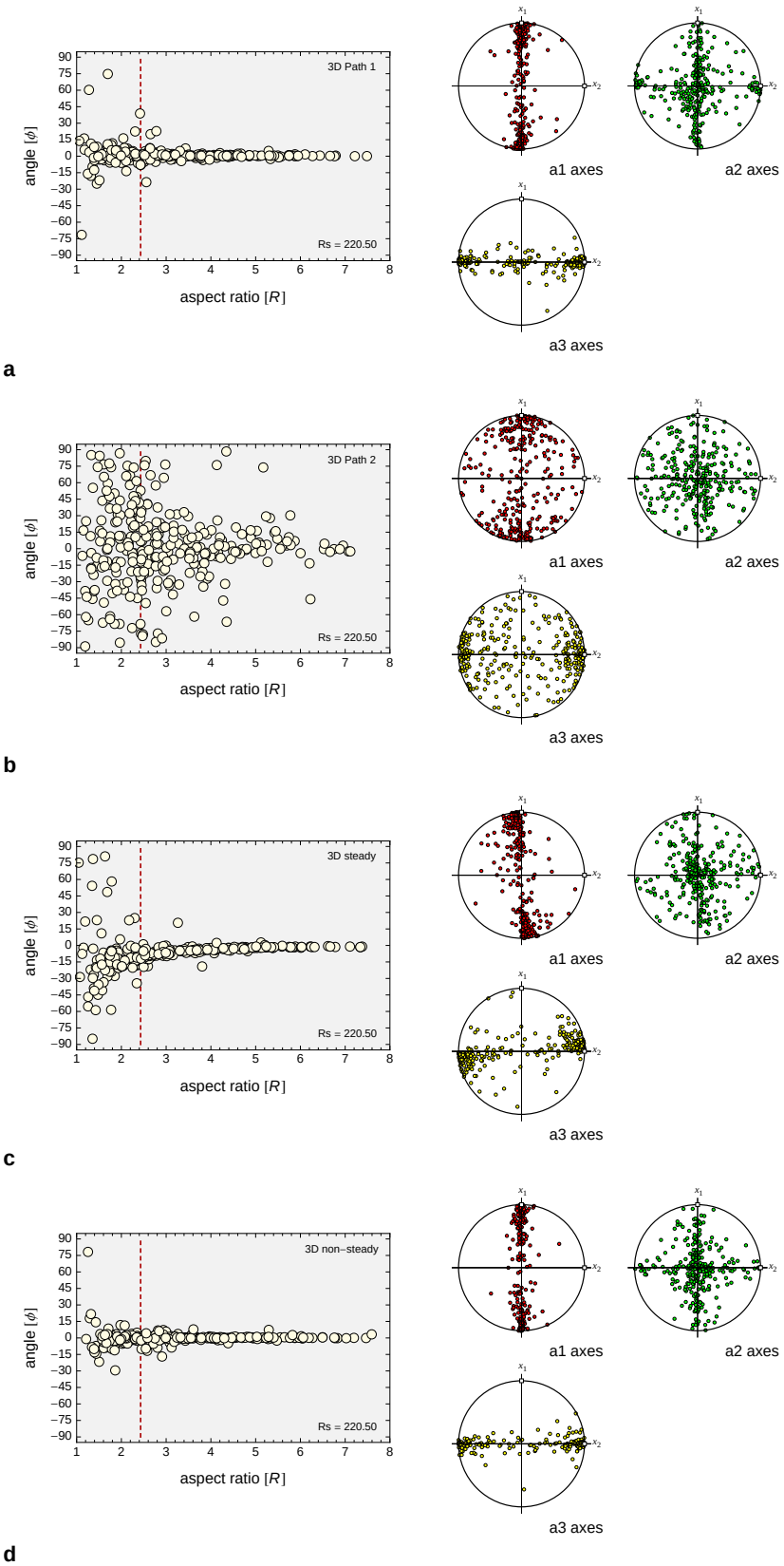

FIGURE 2.11. 3D model results for an offset of 20, $R_S \sim 220$. (a) Path 1; simple shear followed by pure shear. (b) Path 2; pure shear followed by simple shear. (c) Steady flow with $W_k = 0.71$. (d) Minimum strain path. Red dashed line indicates theoretical R_{crit} value for steady flow with kinematic vorticity number of $W_m \equiv W_k = 0.71$.

2.4 Discussion

2.4.1 2D models

Results from our modeling of a population of inclusions in superposed, steady, or non-steady flows are qualitatively similar even at rather large matrix strains. Our 2D models indicate the extended pure shearing-dominated flow history comprising the minimum strain path does not have a significant influence on the resultant clast SPO even at an offset of 20 ($R_S \approx 220$). This result is striking and counter to the expected gross behavior of inclusions typically assumed in application of clast-based vorticity gauges. All clasts with an aspect ratio $R \geq 1.02$ have a stable orientation at the close of the model minimum strain path (final kinematic vorticity number $W_k \approx 0.02$), but clearly many have not reached their stable position. This result shows explicitly that rigid inclusion SPO critically depends on finite strain magnitude experienced by a deformed rock volume, even for dominantly coaxial deformation, and less on the last incremental vorticity or the details of the sub-simple shearing flow path.

The visually estimated cut-off aspect ratio as used commonly in vorticity analysis for all modeled strain paths is similar for a given strain state, with the exception of Path 2 (Figs. 2.4–2.6). However, the similarity of 2D model results does not necessarily imply that clast SPO may be an appropriate tool to assess mean vorticity of a naturally deformed rock. Stahr and Law (2011) have shown that an apparent cut-off aspect ratio between 2.5 and 3.5, often well below the theoretical value, is common in many simple shear-dominated flows even at very high matrix strains, and deformation accumulated by steady flow of lower kinematic vorticity at low to moderate finite strain (see their figs. 9 and 12). Thus, clast SPO is not a unique indicator of kinematic vorticity.

2.4.2 3D models

In general, the bulk SPO resulting from randomly oriented 3D inclusions in plane strain flows is similar to those discussed above for 2D models. This is initially somewhat surprising due to the additional complexities involved in the rotation path of a generally oriented triaxial ellipsoid (see also Jiang, 2007a,b; Li and Jiang, 2011, among others). The most apparent difference is the slightly better ability for pure shear-dominated flows to re-orient low-aspect-ratio clasts that lie at moderate to high angles to the flow plane to more closely approach their stable orientation (e.g.,

Path 1 and minimum strain path, Figs. 2.9 and 2.11). Despite this, the visually estimated cut-off aspect ratio is similar to our 2D model results for the same flow at a given strain state, the only exception being the minimum strain path at an offset of 20 (i.e., $R_S \approx 220$).

2.4.3 Comparison to simple shear

Li and Jiang (2011) suggested that clast SPOs similar to those measured in naturally deformed mylonites can be produced by re-orientation of rigid inclusions in a steady simple shear flow. We tested this by calculating clast SPOs for our initial population in simple shear flows maintained to γ values of 5, 10, 15, and 20 (Figs. 2.12, 2.13). Because inclusions do not have a stable orientation in

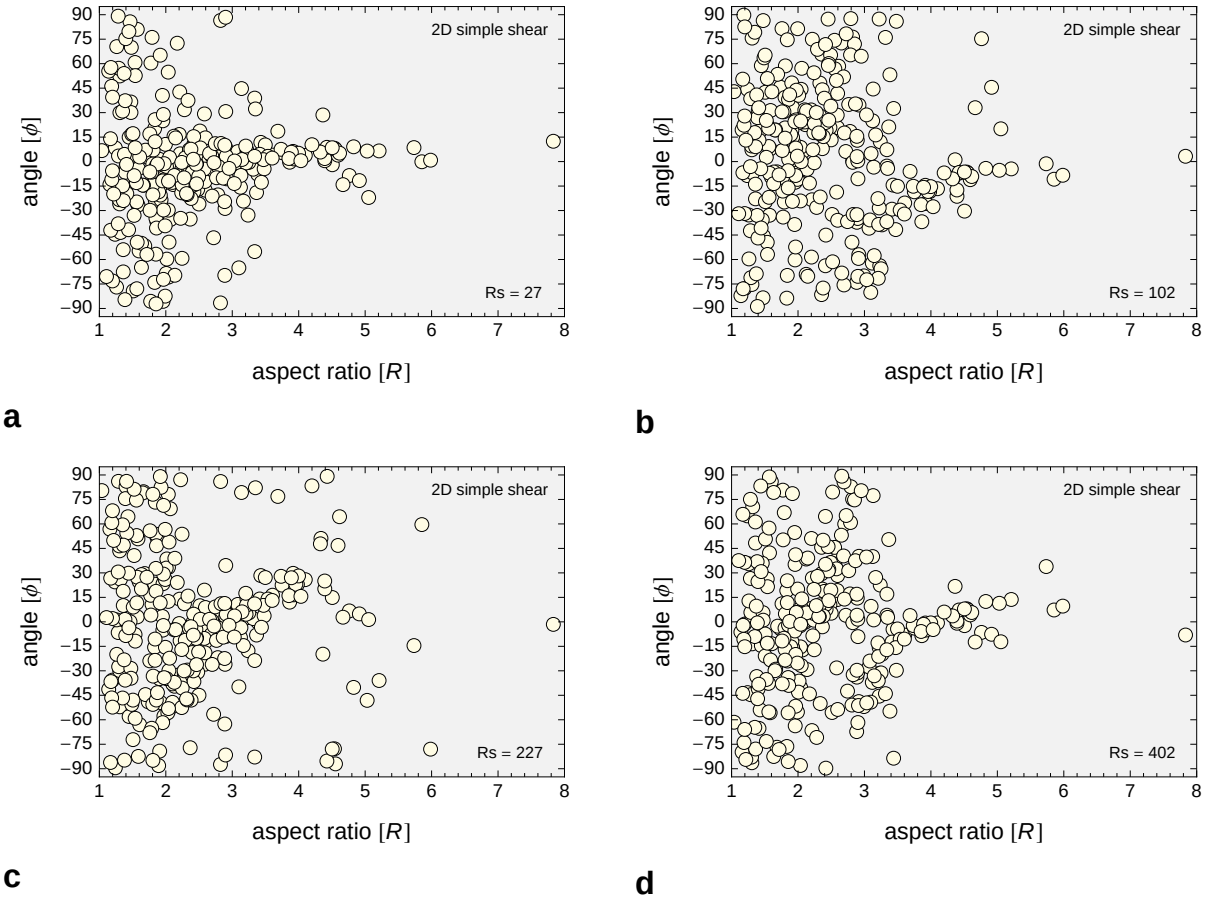

FIGURE 2.12. SPO development with 2D rigid inclusions in a simple shearing flow (Ghosh and Ramberg model). (a) $\gamma = 5$. (b) $\gamma = 10$. (c) $\gamma = 15$. (d) $\gamma = 20$.

simple shear, the SPO is periodic. SPO at some strain values does in fact resemble results from the modeled superposed or minimum strain path (see Figs. 2.4–2.6 and 2.9–2.11). We therefore support Li and Jiang's conclusion that clast SPOs commonly determined from naturally deformed rocks

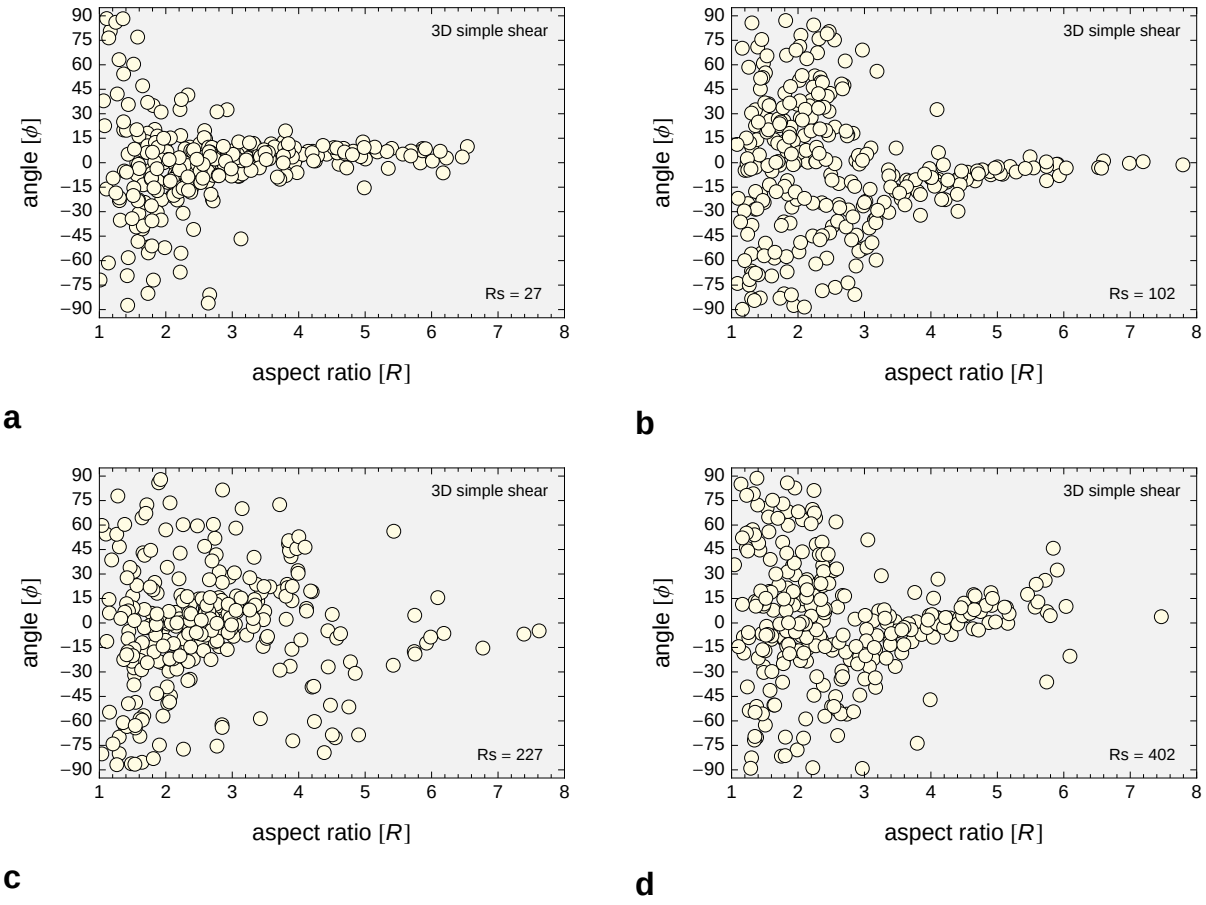

FIGURE 2.13. SPO development with 3D generally oriented triaxial inclusions in a simple shearing flow (Jeffery model). (a) $\gamma = 5$. (b) $\gamma = 10$. (c) $\gamma = 15$. (d) $\gamma = 20$.

could be produced by a single steady simple shear flow. It is interesting to note that Mancktelow (2013) arrived at an identical conclusion for the case of deformable inclusions.

2.4.4 Strain memory

Our modeling clearly demonstrates that a large population of initially randomly oriented rigid inclusions are unlikely to record kinematics of the latest deformation increments, as shown by both Path 1 (simple shear followed by pure shear) and the minimum strain path. Here, due to the nearly end-member pure shear at the close of deformation, nearly every clast in the model population has a stable orientation but few clasts have rotated into this position even after matrix strains as high as $R_S \approx 220$. Additionally, results from our 2- and 3D modeling show that strain paths with identical W_m may produce similar clast SPOs at similar finite strain states, but as illustrated by Path 2 (pure shear followed by simple shear), clast SPO does not always correspond to that of the W_m

of a given deformation. Thus, although individual inclusions are sensitive to boundary conditions and instantaneously respond to vorticity changes, they still require a possibly large amount of finite strain to rotate into orientations approaching their stable position.

2.5 Conclusions

We have investigated numerically the behavior of 2D and generally oriented 3D triaxial rigid inclusions in pure, simple, and sub-simple shear flow to gain insight into the outstanding question of strain memory of a large population of clasts and arrive at some understanding of the sensitivity of final clast orientations to the deformation path of a rock volume. Our modeling shows that most observed characteristics of existing shape preferred orientation analyses made on naturally deformed rocks can be reproduced by many of the superposed, non-steady, or steady 2- or 3D plane strain flow histories that lie within in the restricted range of mean vorticity number considered here (W_m = 0.74–0.71). Model results clearly indicate that rigid inclusion SPOs may be similar for non-steady flows of given W_m, but depending on the details of the strain path may also be significantly different.

Results of rigid clast analyses performed on naturally deformed rocks have been interpreted to record either the mean kinematic vorticity number (W_m) of an entire deformation event, or only the last deformation increments, essentially the instantaneous kinematic vorticity number (W_k) of the latest flow increments, for deformation zones inferred to have experienced temporally varying flow vorticity. It appears that the rotational behavior of rigid clasts suspended in a slowly flowing viscous fluid is more complex than either of the simple end-member hypotheses. The strain memory of clasts is a complex function of both strain path and finite strain. Results from rigid clast analysis are unlikely to yield unequivocal information on the mean kinematic vorticity or possible temporal variations in deformation path experienced by a naturally deformed rock volume.

For detailed investigations of the rotation path of individual clasts (e.g., for inclusion trails in synkinematic porphyroblasts) the full generality of Jeffery's equations for the rotation of a triaxial ellipsoid are clearly necessary (e.g., Jiang and Williams, 2004). However, despite the additional complexities predicted regarding rotation paths of individual inclusions, both the salient characteristics and inherent limitations of rigid clast-based techniques appear to be effectively captured for

a population of inclusions by the simplified 2D approach of Ghosh and Ramberg (1976).

Acknowledgments

Funding for this research was provided by National Science Foundation grant EAR 0711207 to RDL. Virginia Tech scholarship support to DWS is gratefully acknowledged.

References

Bailey, C.M., Francis, B.E., Fahrney, E.E., 2004. Strain and vorticity analysis of transpressional high-strain zones from the Virginia Piedmont, USA. In: Alsop, G.I., Holdsworth, R.E., McCaffrey, K.J.W., Hand, M. (Eds.), Flow Processes in Faults and Shear Zones. Geological Society of London, Special Publication, vol. 224, pp. 249–264.

Bhattacharyya, D., 1966. Orientation of mineral lineation along the flow direction in rocks. Tectonophysics 3, 29–33.

Bretherton, F., 1962. Slow viscous motion round a cylinder in a simple shear. Journal of Fluid Mechanics 12, 591–613.

Cladouhos, T., 1999a. A kinematic model for deformation within brittle shear zones. Journal of structural geology 21, 437–448.

Cladouhos, T., 1999b. Shape preferred orientations of survivor grains in fault gouge. Journal of Structural Geology 21, 419–436.

Fossen, H., Tikoff, B., 1997. Forward modeling of non-steady-state deformations and the 'minimum strain path'. Journal of Structural Geology 19, 987–996.

Freeman, B., 1985. The motion of rigid ellipsoidal particles in slow flows. Tectonophysics 113, 163–183.

Gay, N., 1968. Pure shear and simple shear deformation of inhomogeneous viscous fluids. 1. theory. Tectonophysics 5, 211–234.

Ghosh, S., Ramberg, H., 1976. Reorientation of inclusions by combination of pure shear and simple shear. Tectonophysics 34, 1–70.

Ghosh, S., Sen, G., Sengupta, S., 2003. Rotation of long tectonic clasts in transpressional shear zones. Journal of Structural Geology 25, 1083–1096.

Giorgis, S., Tikoff, B., 2004. Constraints on kinematics and strain from feldspar porphyroclast populations. In: Holdsworth, R.E., McCaffrey, K.J.W., Hand, M. (Eds.), Flow Processes in Faults and Shear Zones, vol. 224, pp. 265–286.

Glen, J., Donner, J., West, R., 1957. On the mechanism by which stones in till become oriented. American Journal of Science 255, 194–205.

Grasemann, B., Fritz, H., Vannay, J.C., 1999. Quantitative kinematic flow analysis from the Main Central Thrust Zone (NW-Himalaya, India): implications for a decelerating strain path and the extrusion of orogenic wedges. Journal of Structural Geology 21, 837–853.

Hooyer, T., Iverson, N., 2000. Clast-fabric development in a shearing granular material: Implications for subglacial till and fault gouge. Geological Society of America Bulletin 112, 683–692.

Jeffery, G., 1922. The motion of ellipsoidal particles immersed in a viscous fluid. Proceedings of the Royal Society of London. Series A 102, 161–179.

Jessup, M.J., Law, R.D., Searle, M.P., Hubbard, M.S., 2007. The rigid grain net (RGN): an alternative method for estimating mean kinematic vorticity number (W_m). Journal of Structural Geology 29, 411–421.

Ježek, J., 1994. Software for modeling the motion of rigid triaxial ellipsoidal particles in viscous flow. Computers & Geosciences 20, 409–424.

Ježek, J., Melka, R., Schulmann, K., Venera, Z., 1994. The behaviour of rigid triaxial ellipsoidal particles in viscous flows – modeling of fabric evolution in a multiparticle system. Tectonophysics 229, 165–180.

Ježek, J., Schulmann, K., Segeth, K., 1996. Fabric evolution of rigid inclusions during mixed coaxial and simple shear flows. Tectonophysics 257, 203–221.

Jiang, D., 2007a. Numerical modeling of the motion of deformable ellipsoidal objects in slow viscous flows. Journal of Structural Geology 29, 435–452.

Jiang, D., 2007b. Numerical modeling of the motion of rigid ellipsoidal objects in slow viscous flows: a new approach. Journal of Structural Geology 29, 189–200.

Jiang, D., 2012. A general approach for modeling the motion of rigid and deformable ellipsoids in ductile flows. Computers & Geosciences 38, 52–61.

Jiang, D., Williams, P.F., 2004. Reference frame, angular momentum, and porphyroblast rotation. Journal of Structural Geology 26, 2211–2224.

Johnson, S., Lenferink, H., Price, N., Marsh, J., Koons, P., West, D., Beane, R., 2009. Clast-based kinematic vorticity gauges: The effects of slip at matrix/clast interfaces. Journal of Structural Geology 31, 1322–1339.

Law, R.D., Searle, M.P., Simpson, R.L., 2004. Strain, deformation temperatures and vorticity of flow at the top of the Greater Himalayan Slab, Everest Massif, Tibet. Journal of the Geological Society of London 161, 305–320.

Li, C., Jiang, D., 2011. A critique of vorticity analysis using rigid clasts. Journal of Structural Geology 33, 203–219.

Mancktelow, N., 2011. Deformation of an elliptical inclusion in two-dimensional incompressible power-law viscous flow. Journal of Structural Geology 33, 1378–1393.

Mancktelow, N., 2013. Behaviour of an isolated rimmed elliptical inclusion in 2D slow incompressible viscous flow. Journal of Structural Geology 46, 235–254.

Marques, F., Coelho, S., 2003. 2-d shape preferred orientations of rigid particles in transtensional viscous flow. Journal of Structural Geology 25, 841–854.

Masuda, T., Michibayashi, K., Ohta, H., 1995. Shape preferred orientation of rigid particles in a viscous matrix: reevaluation to determine kinematic parameters of ductile deformation. Journal of Structural Geology 17, 115–129.

Mulchrone, K., 2007. An analytical solution in 2D for the motion of rigid elliptical particles with a slipping interface under a general deformation. Journal of Structural Geology 29, 950–960.

Passchier, C.W., 1986. Flow in natural shear zones. Earth and Planetary Science Letters 77, 70–80.

Passchier, C.W., 1988. Analysis of deformation paths in shear zones. Geologische Rundschau 77, 309–318.

Reed, L., Tryggvason, E., 1974. Preferred orientations of rigid particles in a viscous matrix deformed by pure shear and simple shear. Tectonophysics 24, 85–98.

Schmid, D., Podladchikov, Y., 2004. Are isolated stable rigid clasts in shear zones equivalent to voids? Tectonophysics 384, 233–242.

Simpson, C., De Paor, D.G., 1993. Strain and kinematic analysis in general shear zones. Journal of Structural Geology 15, 1–20.

Simpson, C., De Paor, D.G., 1997. Practical analysis of general shear zones using the porphyroclast hyperbolic distribution method: an example from the Scandinavian Caledonides. In: Sengupta, S. (Ed.), Evolution of Geological Structures in Micro- to Macro-scales. Chapman and Hall, pp. 169–184.

Stahr, III, D.W., Law, R.D., 2011. Effect of finite strain on clast-based vorticity gauges. Journal of Structural Geology 33, 1178–1192.

Sullivan, W.A., 2008. Significance of transport-parallel strain variations in part of the Raft River shear zone, Raft River Mountains, Utah, USA. Journal of Structural Geology 30, 138–158.

Tikoff, B., Fossen, H., 1993. Simultaneous pure and simple shear: the unifying deformation matrix. Tectonophysics 217, 267–283.

Wallis, S.R., Platt, J.P., Knott, S.D., 1993. Recognition of syn-convergence extension in the accretionary wedges with examples from the Calabrian Arc and the Eastern Alps. American Journal of Science 293, 463–495.

Willis, D., 1977. A kinematic model of preferred orientation. Geological Society of America Bulletin 88, 883–894.

Xypolias, P., 2010. Vorticity analysis in shear zones: A review of methods and applications. Journal of Structural Geology 32, 2072–2092.

Chapter 3

Coupled deformation and metamorphism within the Main Central Thrust zone, Sutlej Valley, NW India

Donald W. Stahr, III[1], Mark J. Caddick[1], Richard D. Law[1], Robert J. Tracy[1], Talat Ahmad[2]

[1]*Department of Geosciences, Virginia Polytechnic Institute and State University, Blacksburg, VA, 24061, USA*
[2]*Department of Geology, Delhi University, Delhi, India, 110091, India*

This article may be submitted to *Journal of Metamorphic Geology* for publication.

Abstract

The burial and exhumation history of a High Himalayan schist collected from within the Main Central Thrust (MCT) zone in the eastern Sutlej Valley of NW India is deduced from compositional zoning of large garnet porphyroblasts. Zoning patterns have not been significantly modified by diffusion during or after growth and correspond well to predictions of garnet fractional crystallization models. Detailed textural and microstructural analysis indicates that garnet overgrew an early S1 foliation that was subsequently folded and transposed into the dominant S2 transposition foliation during the main D2 deformation phase associated with Miocene top-SW, reverse-sense motion on the MCT. Waning stages of D2 deformation outlasted porphyroblast growth, and late top-NE shear bands related to extension in the MCT hanging wall locally overprint S2. Our calculated P–T path indicates rocks currently exposed within the MCT zone of Sutlej Valley experienced rapid burial with heating, continued heating during initial decompression, and rapid exhumation and cooling. The path is best explained by initial burial of rocks located in the footwall to the SW of the presently exposed MCT, followed by incorporation of these rocks into the hanging wall of the progressively southward-migrating MCT deformation front.

3.1 Introduction

The Himalayan orogen is the expression of Cenozoic crustal deformation related to continental collision of India and Asia that commenced ∼54–50 Ma (e.g., Hodges, 2000; Searle et al., 2007). As the largest and youngest orogenic belt on Earth, the Himalaya are the focus of active research into the thermal and mechanical response of continental lithosphere to the collision process. Studies of the crystalline core of the orogen provide critical insight into mid-crustal processes operating in response to large-scale collision tectonics. Many of the first-order constraints used in construction of both conceptual and quantitative geodynamic models (e.g., Channel Flow; Beaumont et al., 2004; Critical taper; Kohn, 2008) are derived from pressure, temperature, and temporal (P–T–t) data determined by detailed structural and petrologic studies of the Himalayan metamorphic core.

This contribution focuses on a single sample from the MCT zone in the eastern Sutlej Valley where prograde garnet growth zoning features are preserved. This specimen provides the best opportunity to integrate detailed textural and microstructural relationships with forward thermodynamic modeling to elucidate details of the early prograde metamorphic history in terms of the pressure–temperature–composition (P–T–X) evolution of rocks at this structural level of the High Himalayan Crystalline Sequence (HHCS). We then use our inferred P–T path and apply a coupled model of garnet growth and cation diffusion to demonstrate that the observed garnet compositional zoning is related to growth and has not been modified in the timescales available since collision

commenced. The path derived here for rocks in the MCT zone—heating during loading, followed by continued heating during initial unloading, and rapid cooling and exhumation—can be best explained by an initial burial phase of MCT footwall material followed by incorporation into the deformation zone and conductive heating and finally rapid exhumation as the rocks were entrained in the SW-directed flow as the locus of mylonitization continuously propagated to the southwest. The results provide new insights into the coupled nature of deformation and metamorphism in the MCT zone of the Sutlej Valley, and illustrate the importance of interdisciplinary structural and petrologic analysis in investigations into P–T paths and development of inverted metamorphic sequences.

3.1.1 Geologic framework

The Himalayan orogenic belt consists of a stack of distinct tectonostratigraphic units that display remarkable lateral continuity across the ∼2400 km length of the orogen (Fig. 3.1; e.g., Le Fort, 1996; Hodges, 2000). The HHCS, typically exposed as a 5–30 km thick northward-dipping slab of middle amphibolite to lower granulite facies pelitic to psammitic paragneiss intercalated with minor calc-silicate and orthogneiss, constitutes the metamorphic core of the orogen. The uppermost portion of the HHCS is intruded by variable amounts of leucocratic granitoids derived from partial melting during Miocene orogenesis. The HHCS is bounded by two subparallel north-dipping ductile shear zones of opposite shear sense that were both active broadly contemporaneously during Miocene time (e.g., Searle et al., 1999; Hodges, 2000); the MCT at its base and the South Tibetan Detachment System (STDS) of north-directed normal faults at the top. These major tectonic boundaries separate the crystalline core from typically low-grade to unmetamorphosed sedimentary rocks of the Lesser Himalaya (below) and Tethyan Himalaya (above).

3.1.2 Geology of the Sutlej River Valley

The Sutlej River is one of the largest trans-Himalayan rivers that cuts across the high topography of the crystalline core of the NW Himalayan range. This natural section exposes each of the major tectonostratigraphic units that comprise the orogen; from SW to NE, the Sub-Himalaya, Lesser Himalaya, Greater Himalayan Series or High Himalayan Crystallines, and Tethyan Himalaya. Our focus lies in the high-grade metamorphic core exposed in the easternmost Sutlej Valley, Himachal

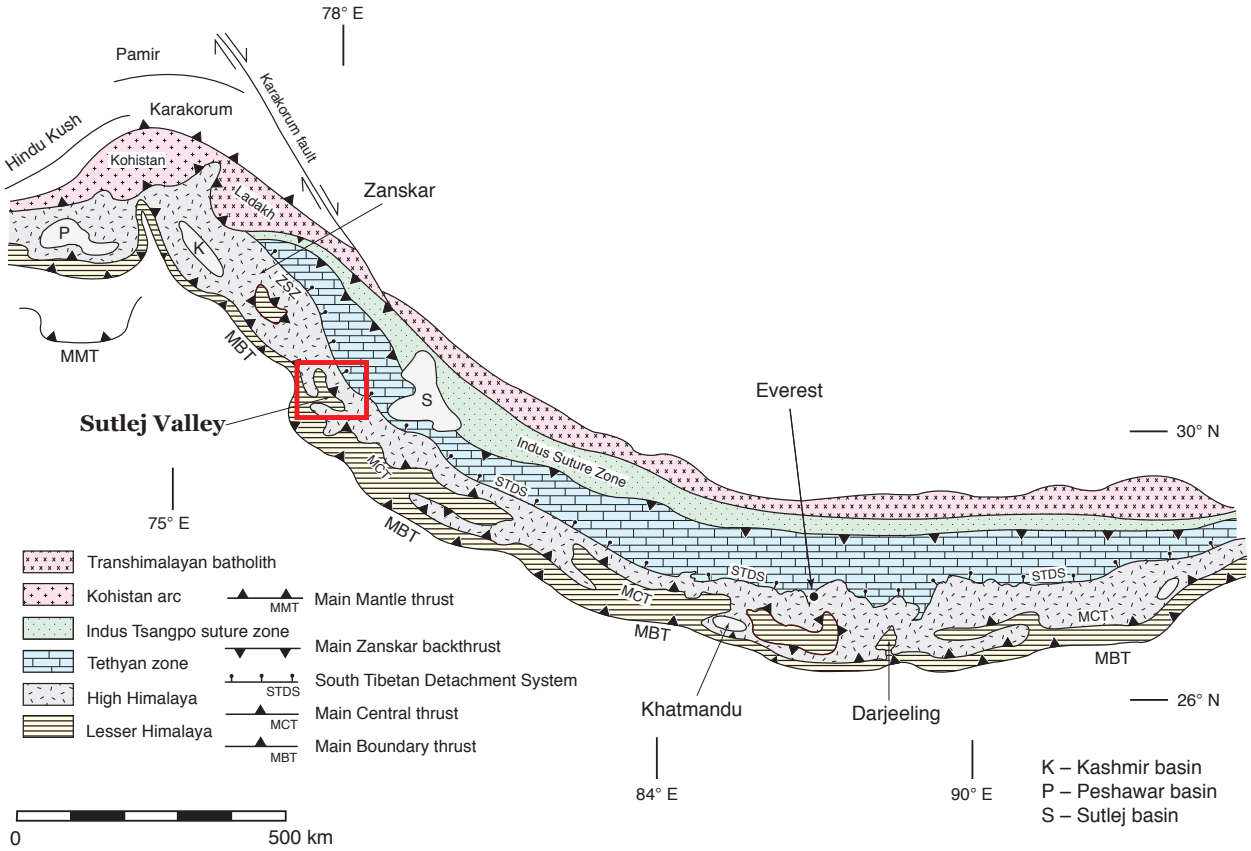

FIGURE 3.1. Simplified tectonic map of the Himalayan orogen showing the distribution of main tectonostratigraohic units and location of the Sutlej Valley area discussed in text. The Higher Himalayan Crystalline Series is bounded below by the Main Central Thrust (MCT) and above by the South Tibetan Detachment System (STDS). Inset box indicates location of Fig. 3.2. MBT–Main Boundary Thrust; MMT–Main Mantle Thrust; ZSZ–Zanskar Shear Zone; K–Kashmir basin; P–Peshawar basin; S–Sutlej basin; Modified from Law et al. (2004).

Pradesh, NW India (Fig. 3.2).

In this region the MCT is exposed as a gently folded shallow- to moderate southwest- to northeast-dipping 0.5–2 km thick mylonite zone with abundant top-SW (i.e., reverse-sense) kinematic indicators. The MCT in the Sutlej Valley is exposed in a series of klippen (Shimla Klippe) and in the cores of gentle upright synformal folds (Luhri syncline), allowing examination of the MCT and hanging wall HHCS rocks in several locations over an ∼100 km foreland–hinterland transect parallel to the inferred transport direction. Focus is given here to the easternmost exposed HHCS rocks in the Sutlej Valley, the upper panel of material forming the metamorphic core of the orogen.

The local structural framework in the Sutlej transect is complicated by the presence of two inverted metamorphic field gradients reaching mid-upper amphibolite facies in the hanging wall of

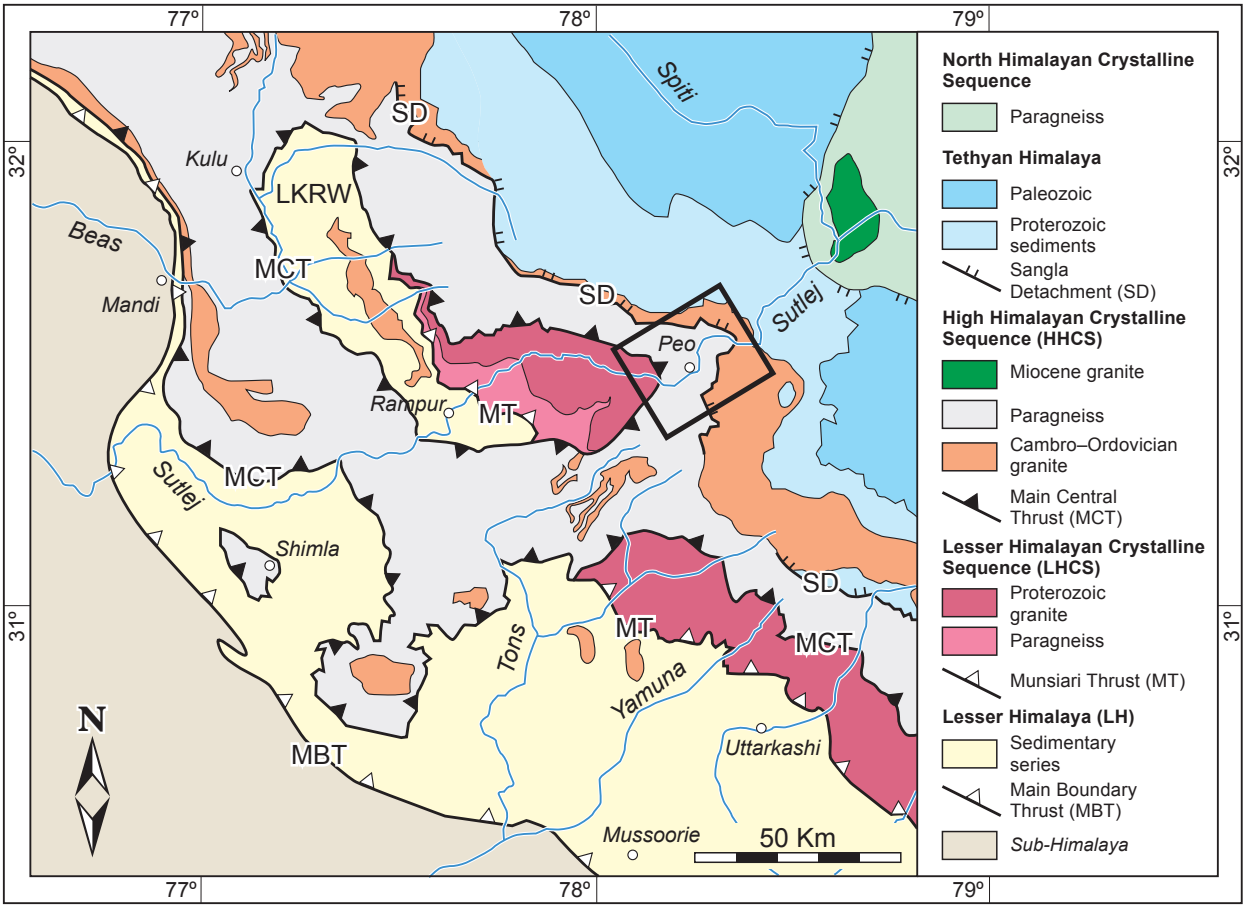

FIGURE 3.2. Regional geologic map of the Sutlej Valley and surrounding area showing distribution of main tectonostratigraphic units. Note exposure of MCT at several locations over ∼100 km parallel to the inferred SW tectoninc transport direction near Shimla, Rampur, and Peo. Inset box in eastern Sutlej Valley shows location of study area (Fig. 3.3). LKRW–Largi-Kulu-Rampur window. Modified from Vannay and Grasemann (1998); Vannay et al. (1999); Wiesmayr and Grasemann (2002); Vannay et al. (2004).

two ductile shear zones (Vannay and Grasemann, 1998; Vannay et al., 1999; Caddick et al., 2007). Paragneisses with appropriate bulk compositions to develop obvious indicators of metamorphic grade within these two inverted metamorphic sequences are separated by the ∼6–7 km thick, 1.80±0.01 Ga Wangtu orthogneiss (Miller et al., 2000), an augen gneiss that displays clear evidence for top-SW shear interpreted to be a result of Himalayan (Miocene) deformation (e.g., Vannay and Grasemann, 2001).

We adopt the convention of Vannay and Grasemann (2001), among others, and infer that the mylonitized upper contact of the Wangtu orthogneiss and overlying staurolite zone metasediments exposed in the eastern Sutlej Valley marks the position of the most hinterland exposure of the MCT (Fig. 3.2). In this framework the paragneiss that overlies the Wangtu gneiss is considered

the HHCS, whereas rocks at structurally lower levels in the footwall to the MCT constitute the Lesser Himalayan Crystalline Sequence (LHCS). The contact between the two (i.e., the MCT) is clearly tectonic, distinguished in the field by a zone of distributed shear with abundant reverse-sense kinematic indicators. The MCT zone is locally overprinted by later brittle-ductile fabrics (e.g., top-N shear bands, discrete m-scale cataclastic zones) associated with extension in the MCT hanging wall (Marquer et al., 2000; Vannay et al., 2004).

Recent work has demonstrated distinct metamorphic evolution of LHCS and HHCS tectonostratigraphic units in the Sutlej Valley. Contrasting P–T path geometry and timing of metamorphism (~10 Ma for LHCS vs. ~23 Ma for HHCS) have been documented for the LHCS in the Sutlej Valley by Caddick et al. (2006, 2007). Additionally, Richards et al. (2005) have demonstrated that the area under consideration yields isotopic systematics ($\varepsilon_{Nd} > -13$; corrected for a 500 Ma reference) and $^{87}Sr/^{86}Sr < 0.8$ distinct from those of the mapped footwall to the MCT ($\varepsilon_{Nd} < -16$ and $^{87}Sr/^{86}Sr > 0.8$). These isotopic values are similar to those in other areas and argue for a Neoproterozoic or younger source and thus Greater Himalayan affinity for hanging wall rocks.

Higher Himalayan Crystalline Series of the Sutlej Valley

The HHCS in the eastern Sutlej Valley is exposed as an ~10 km thick moderately north-dipping slab of mid-amphibolite facies to anatectic paragneiss (Fig. 3.3). In this area an inverted metamorphic field gradient is defined by staurolite zone rocks at the base, overlain by kyanite- and sillimanite-zone assemblages, and finally anatectic paragneiss at the top ~1 km of section below the Sangla Detachment (SD), the local strand of the STDS. General features of HHCS metamorphism have been presented elsewhere (for a summary see Vannay et al., 2004), therefore we outline briefly the most pertinent aspects of the geology to provide sufficient context for our analyses that are described in detail below.

Previous quantitative investigations into peak metamorphic conditions preserved in the HHCS in this region have utilized an array of techniques, including conventional and multi-equilibria thermobarometry, and oxygen isotope thermometry (see Vannay and Grasemann, 1998; Vannay et al., 1999; Vannay and Grasemann, 2001). Figure 3.4 presents new thermobarometric results from the present study for a transect through the entire HHCS together with a compilation of previous work. Calculations performed using the average PT function of THERMOCALC (v. 3.26)

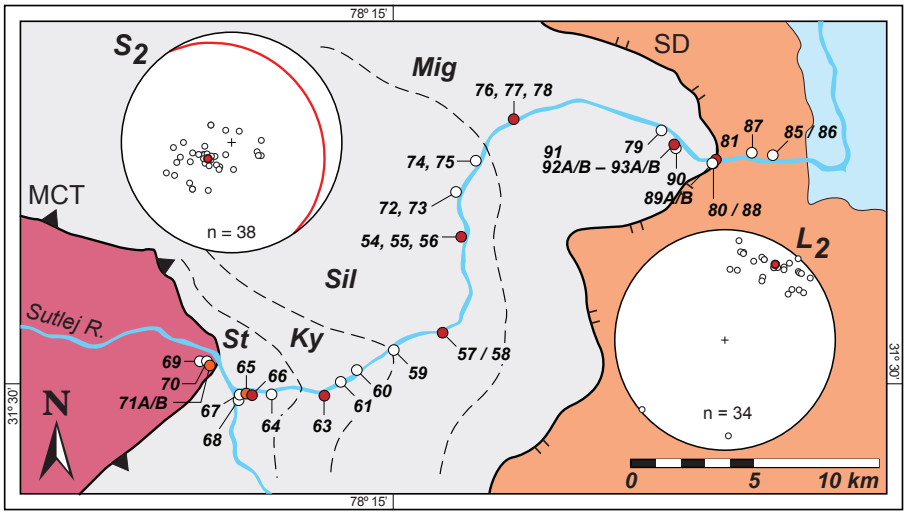

FIGURE 3.3. Geologic map of the eastern Sutlej Valley showing sample locations and approximate position of isograds. Inset lower hemisphere, equal-area projections of dominant foliation (S2) and stretching lineation (L2). Red circles in each projection indicate vector mean of foliation and lineation for the map area. Red great circle indicates orientation of mean foliation. Locations of samples used for microstructural observations (white circles), quartz petrofabric analysis (orange circles), and petrologic work (red circles) indicated on map. MCT–Main Central Thrust; SD–Sangla Detachment; St–staurolite zone; Ky–kyanite zone; Sil–sillimanite zone; Mig–onset of partial melting. Modified from Vannay and Grasemann (1998); Vannay et al. (1999).

and average matrix phase compositions of the inferred stable peak assemblage coupled with garnet rim or core compositions yield P and T estimates consistent with observed phase stability. Results from this and previous studies exhibit excellent agreement between methods and indicate that peak-T varies from ~550–600 °C at the level of the MCT to ~700–750 °C at approximately 3.5–4 km structurally above the MCT and appears to remain nearly constant or decrease slightly traced toward the SD (Fig. 3.4). While our new analyses appear to have slightly better precision than previous THERMOCALC analyses, they provide little further insight into the P–T conditions attending exhumation of HHCS rocks in the Sutlej Valley. Our new results confirm that the inverted T gradient is not associated with a statistically significant P gradient; all specimens appear to have equilibrated at roughly ~8–8.5 kbar (~30 km depth for an average crustal density of 2800 kg m^{-3}). Detailed structural, petrologic, and geochronologic investigations into the HHCS of the Sutlej Valley have yielded a wealth of information regarding the evolution of the region and provides context within which we interpret textural and microstructural observations and petrologic analyses (e.g., Vannay and Grasemann, 1998; Grasemann et al., 1999; Manickavasagam et al., 1999; Vannay et al., 1999; Vannay and Grasemann, 2001; Vannay et al., 2004; Caddick et al., 2007; Thakur and Tripathi, 2008; Chambers et al., 2009). Despite these detailed quantitative investigations however, significant

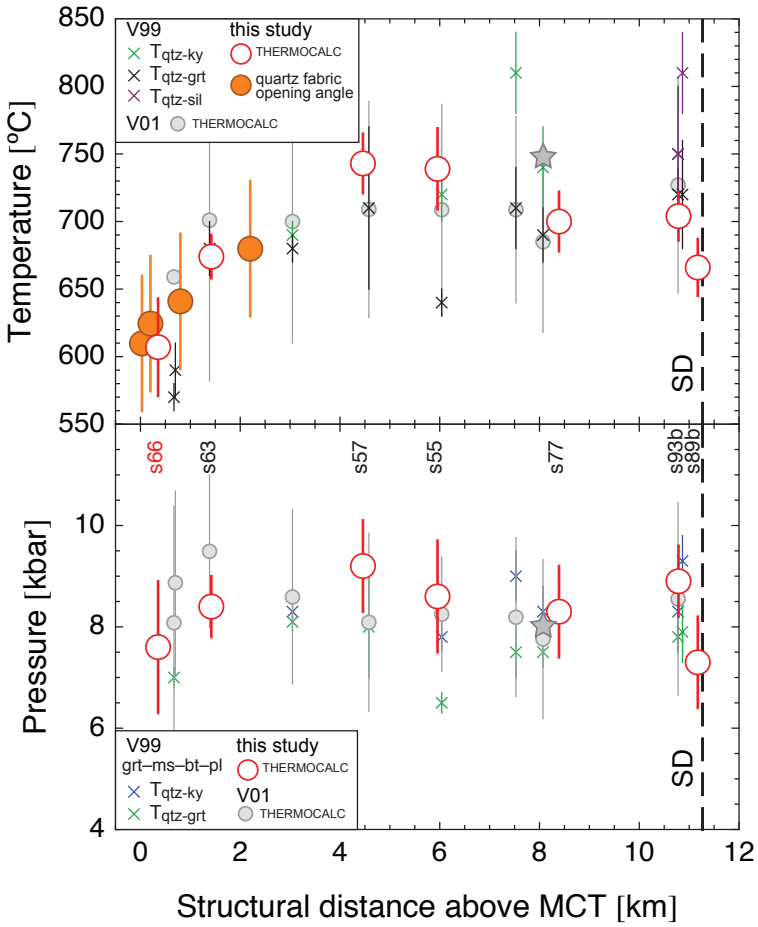

FIGURE 3.4. Compilation of temperature and pressure estimates from eastern Sutlej transect. Upper panel–near-peak metamorphic temperature estimates obtained from oxygen isotope thermometry and THERMOCALC multi-equilibria thermobarometry (Powell and Holland, 1994). Deformation temperatures (orange circles) calculated with the quartz *c*-axis fabric thermometer (Kruhl, 1998) shown for comparison. Results from each independent dataset define an approximately linear dependence of temperature on structural distance for 0 to ~3000 m above the MCT, while oxygen isotope and multi-equilibria thermometry results from above this structural level suggest no significant temperature gradient. Lower panel–pressure estimates. The data define an essentially isobaric array at ~8 kbar suggesting rocks in this transect equilibrated at largely similar crustal levels. Pressure estimates from Vannay et al. (1999) obtained by conventional Grt-Bt-Ms-Pl equilibria at temperature indicated by oxygen isotope analysis for a given sample. Star marks *P–T* path peak discussed in Vannay and Grasemann (1998). Error bars correspond to calculated 2σ and 1σ uncertainty on oxygen isotope and THERMOCALC results, respectively, and nominal 50 °C uncertainty estimated for the quartz *c*-axis fabric opening angle thermometer. Samples analyzed in this study indicated by sample number in lower panel. Sample S09-66 selected for detailed analysis in this work indicated by red typeface. Abbreviations as follows: V99–Vannay et al. (1999); V01–Vannay and Grasemann (2001).

portions of the metamorphic history of the HHCS remain uncertain, and little information exists regarding the interaction between deformation and metamorphism in the crystalline core here.

3.2 Analytical methods

Mineral chemistry was determined with a Cameca SX-50 electron microprobe at the Virginia Tech Electron Beam Laboratory using a 15 kV accelerating voltage and 20 nA beam current and a range of natural and synthetic standards. X-ray compositional mapping was performed using WDS stage scans with 2–10 μm step sizes for the elements Fe, Mn, Mg, and Ca. Mapping was conducted with a focused beam and 250–300 nA beam current and 20–50 ms dwell times. Major element bulk chemistry was determined by X-ray fluorescence spectroscopy (XRF) using a PANalytical 2404 X-ray fluorescence vacuum spectrometer at Franklin and Marshall College. XRF analysis was conducted on fused discs derived from an aliquot of powdered material ($\sim$10 cm^3 volume of sample material was powdered from which the aliquot was extracted).

Thermodynamic modeling was carried out in the 10 component system MnO-Na_2O-CaO-K_2O-FeO-MgO-Al_2O_3-SiO_2-H_2O-TiO_2 (MnNCKFMASHT) using the programs THERIAK-DOMINO (de Capitani and Brown, 1987; de Capitani and Petrakakis, 2010) with version ds5.5 of the Holland and Powell (1998) thermochemical database. Excess H_2O was assumed for equilibrium assemblage diagram calculations; a melt phase was not considered. Activity-composition models used are as follows: garnet, chlorite, staurolite, chloritoid, cordierite follow the formulation of Holland and Powell (1998) extended for Mn solid solution after Mahar et al. (1997); Ti-bearing biotite after Holland and Powell (1998) and White et al. (2000); white mica was modeled after Coggon and Holland (2002); ternary feldspar of Furhman and Lindsley (1988); and ilmenite was formulated with ideal mixing of phase components ilmenite, geikielite, and pyrophanite. The composition used for modeling was derived from the raw XRF bulk chemical data by omitting P_2O_5 and projecting from pyrrhotite.

Diffusion modeling of divalent cations in garnet followed the methodology outlined in Caddick et al. (2010) with garnet diffusion coefficients of Carlson (2006). Mineral abbreviations follow Kretz (1983) throughout the article with the exception of Wm for white mica.

3.3 Petrography

Sample S09-66 is a St–Grt–Bt–Wm–Qtz–Ilm schist collected from the HHCS. Accessory epidote and apatite together with ubiquitous tourmaline are also present in the matrix and as inclusions within porphyroblasts. The specimen was collected $\sim$350 m above the inferred position of the MCT

(Figs. 3.3, 3.4) near the confluence of the Sutlej and Baspa Rivers.

3.3.1 Microstructural relationships

At the lowest structural levels above the MCT, the dominant matrix foliation (S2) is a transposition fabric related to reverse-sense motion on the MCT. In outcrop, NE-dipping shear bands cross cut S2, suggesting a late phase of extension in the immediate hanging wall of the MCT (see also Marquer et al., 2000; Vannay et al., 2004). Garnet occurs as porphyroblasts 2–5 mm in diameter. Small (< 50 μm length) zoisite or clinozoisite inclusions occur in high-Ca cores of garnet porphyroblasts. Aligned linear to helicitic inclusion trails of quartz and ilmenite in garnet cores preserve an earlier (S1) foliation (Fig. 3.5a–c). Inclusion trails are invariably truncated by inclusion-poor garnet rims of variable thickness and cannot be traced into the adjacent matrix. The above relationships suggest some garnets nucleated and overgrew an early S1 foliation prior to D2 deformation associated with the transposition fabric in HHCS rocks of the eastern Sutlej section.

Similar features to those described above were observed in garnet-bearing specimens collected within ~1500 m of the MCT (Fig. 3.5). These microstructural relationships give way to more ambiguous textures and microstructures at higher structural levels. Porphyroblasts observed in specimens collected above the middle of the HHCS ($\geq$ 1500 m above the MCT) are wrapped by penetrative S2 fabric and locally preserve randomly oriented inclusions (typically quartz, rutile, ilmenite, but also rare biotite, apatite, plagioclase, and kyanite). Lack of unequivocal matrix–porphyroblast inclusion relationships frustrates attempts to relate mineral growth and reactions to the deformation history at mid-high structural levels of the HHCS.

In the uppermost 5 km of the HHCS in the Sutlej Valley, aluminum silicates (kyanite laths or fibrolitic sillimanite mats) are typically aligned within and partly define the matrix foliation and are locally drawn into shear bands. Undulatory extinction of these crystals indicates unrecovered lattice strain suggesting deformation continued after growth of the inferred peak metamorphic assemblage. Patchy replacement of garnet and staurolite by chlorite and local alteration of kyanite to cross cutting and non-aligned laths of muscovite indicate local availability of fluid during the retrograde cooling path following cessation of deformation (Fig. 3.5d–e).

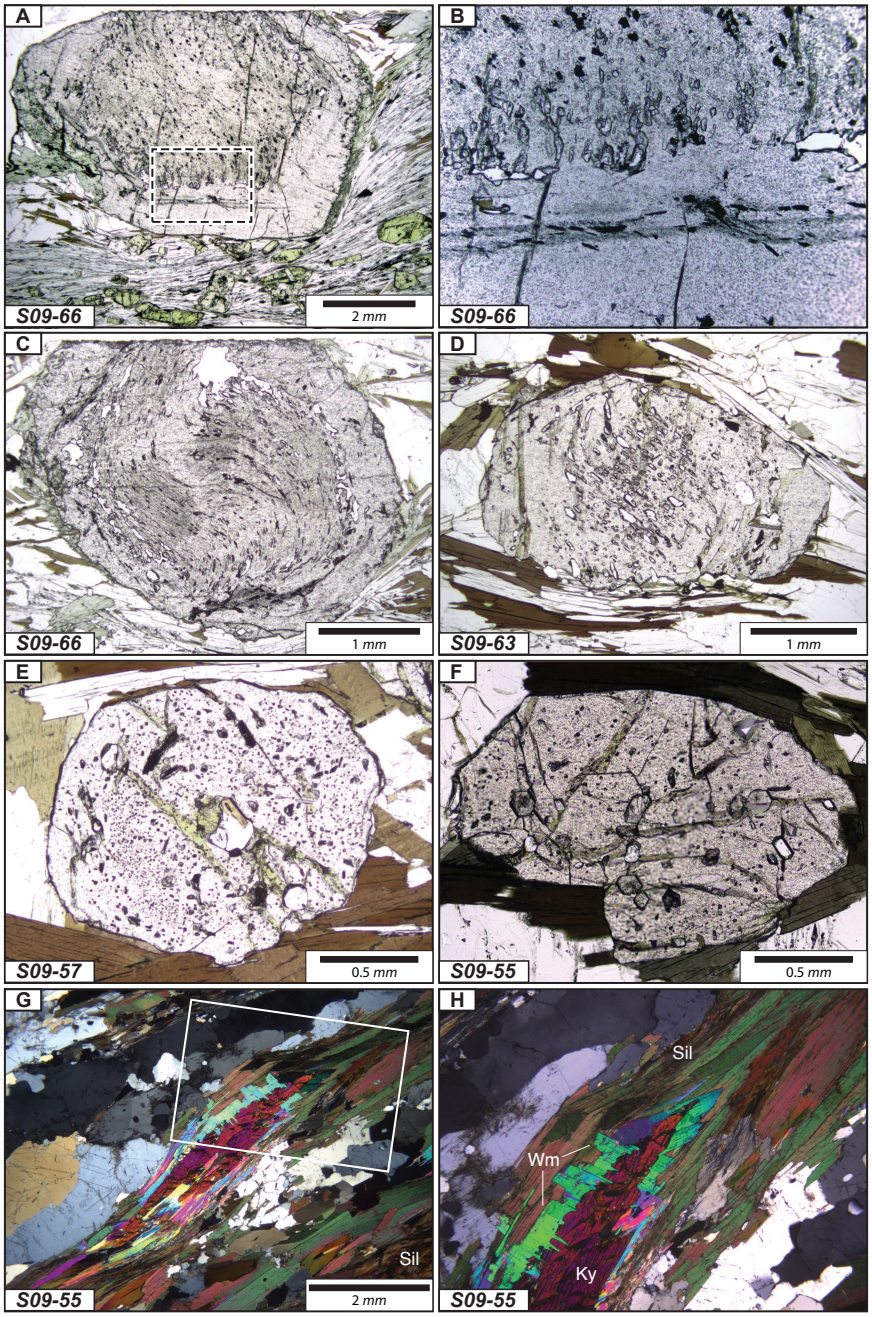

FIGURE 3.5. Representative HHCS porphyroblast–matrix relationships and microstructures from lower to middle-upper structural levels. (a) Garnet from S09-66. Note curvilinear trace of inclusion trails in core and thick inclusion-free rim. (b) Detail of area indicated in (a). Note 'textural unconformity' indicated by highly oblique inclusion trail orientations at core / rim junction. (c) Helicitic garnet from sample S09-66. Note truncation of curvilinear inclusion trails at thin inclusion-poor rim. (d) Garnet from sample S09-63 (∼1500 m above MCT). Inclusion-rich core and inclusion-poor rim similar to garnet observed at the level of the MCT. (e) Garnet from sample S09-57 (∼4200 m above MCT). Inclusions of ilmenite, rutile, biotite, and quartz display no preferred orientation. (f) Garnet from sample S09-55 (∼6000 m above MCT). Inclusions in garnet are quartz and aluminum silicate (kyanite). (g) Relict kyanite crystal in sillimanite zone rock. (h) Detail of area shown in (g). Note texturally late muscovite replacing kyanite. Muscovite laths grew oblique to S2 foliation and post-dates last increments of deformation. Plane-polarized light in (a–f), crossed polarizers in remaining micrographs. All sections viewed toward the north.

3.3.2 Textural zoning in garnet

Textural sector zoning is defined as intracrystalline compositional difference where the chemical zones are crystallographically controlled (e.g., Hollister, 1970; Kohn, 2004). Some garnets in sample S09-66 preserve evidence of textural sector zoning (Fig. 3.6a). In the best-developed instance, the

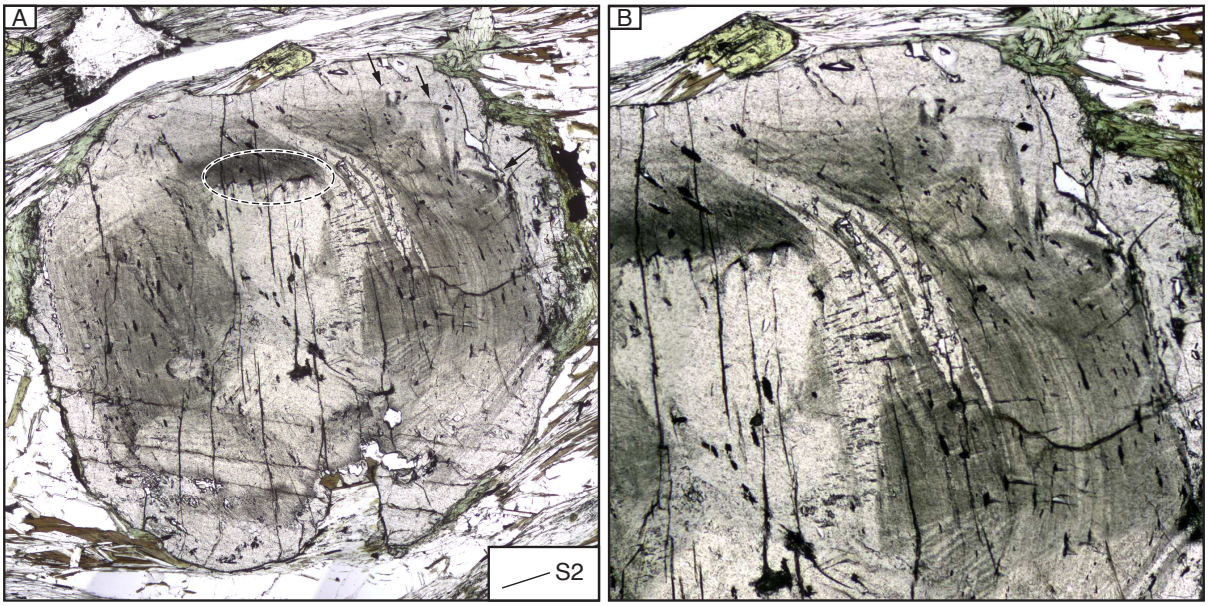

FIGURE 3.6. Example of textural sector zoning in MCT zone garnet from sample S09-66. (a) Large textural sector zoned garnet (diameter ~4 mm). Note relatively inclusion-free hourglass-shaped core extending into graphite-rich mantle. Ilm inclusion trails are aligned at a high angle to the external S2 foliation. The outermost graphite-rich mantle shows triangular faces terminating at the outermost thin inclusion-poor rim. The exterior morphology of the crystal mimics the geometry of these triangular facets suggesting they are former crystal faces that existed during garnet growth. Ellipse denotes area of graphite accumulation, arrows indicate location of crystal faces outlined by graphitic material at the outer right mantle of garnet. (b) Detail of core and rim of garnet shown in (a). Note small-scale triangular apophyses extending from hourglass-shaped core into graphite-rich mantle resulting in an apparent accumulation of graphite-rich material. Also within the graphite-rich interior notice the small wavelength open crenulations developed with the trace axial plane subparallel to the dominant S2 matrix fabric. Plane-polarized light. Section viewed toward the north.

presence of inclusion-poor cores partly bounded and defined by linear inclusion trails that radiate from the central region of the crystal define sector zones (Type 1 inclusions of Andersen, 1984). Textural sector zoned cores terminate in graphite-rich inclusion zones in the mantle of the crystal. Near the terminations, triangular promontories extend into and displace finely layered graphite-rich areas where concentrated zones of graphitic material have locally developed (Fig. 3.6b). Beyond this, at the outward margin of the graphite-rich mantle, apparent rational crystal faces defined by graphitic inclusion-rich zones extend outward from the inner mantle and terminate at thin outer rims of inclusion-free garnet. These zones are clearly apparent in X-ray compositional maps,

and they are observed to terminate at rims with distinctly lower concentration of X_{Grs} and X_{Sps}, and higher concentrations of X_{Alm} and X_{Prp} (see below). The outer inclusion-poor rim is often marked by a concentrically arranged zone of globular quartz inclusions. The observed textural relationships may indicate renewed garnet growth under different P–T conditions or a change in the garnet-producing reaction toward the end of garnet growth. No conclusive evidence exists for significant resorption of garnet near this textural and compositional discontinuity.

3.4 Garnet compositional zoning

Garnets in sample S09-66 consistently display three concentric zones (Fig. 3.7). A central zone (zone 1) is defined by flat to slightly decreasing concentration of X_{Grs} from a relatively enriched core (X_{Grs} = 0.22–0.20) to values of ∼0.18–0.16. Here X_{Sps} also decreases outward from ∼0.16 in the cores of large crystals to 0.07–0.05. X_{Alm} increases from core values of ∼0.60 to ∼0.73–0.70. In an intermediate zone (zone 2) corresponding to a thin to thick mantle, steep gradients of all components are observed. A steep drop is observed in X_{Grs} to values of ∼0.05. A concomitant increase in X_{Alm} to ∼0.82–0.80 and an increase in X_{Prp} is observed in this zone. X_{Sps} continues to decrease. The rim zone (zone 3) is of variable thickness and is characterized by flat to slightly increasing X_{Alm}, increasing X_{Prp} to values of ∼0.12–0.10; X_{Grs} typically levels out to a shoulder (200–500 μm thick) of constant composition, and X_{Sps} continues to decrease toward the rim. A high Y annulus is coincident with the X_{Grs} shoulder where present.

The zones described above are concentrically arranged about the central region of garnet cores and typically parallel the external crystal forms. In a few cases, however, narrow elongate ridges of higher X_{Grs} content trend radially outward from the garnet core region at a high angle to the general concentric zoning. Similar zoning features have been interpreted to indicate rapid garnet growth (e.g., Kohn, 2004; Moynihan and Pattison, 2013).

Growth zoning such as that described above is poorly preserved at higher structural levels of the HHCS. At the ∼1500 m structural level, evidence for diffusional modification or relaxation of chemical gradients becomes apparent (Fig. 3.8). Zoning observed in garnets from this area is complicated by core regions of significantly different composition than their mantle overgrowths. Several garnets from S09-63 display a local maximum in X_{Alm} and local minimum in X_{Grs} in the

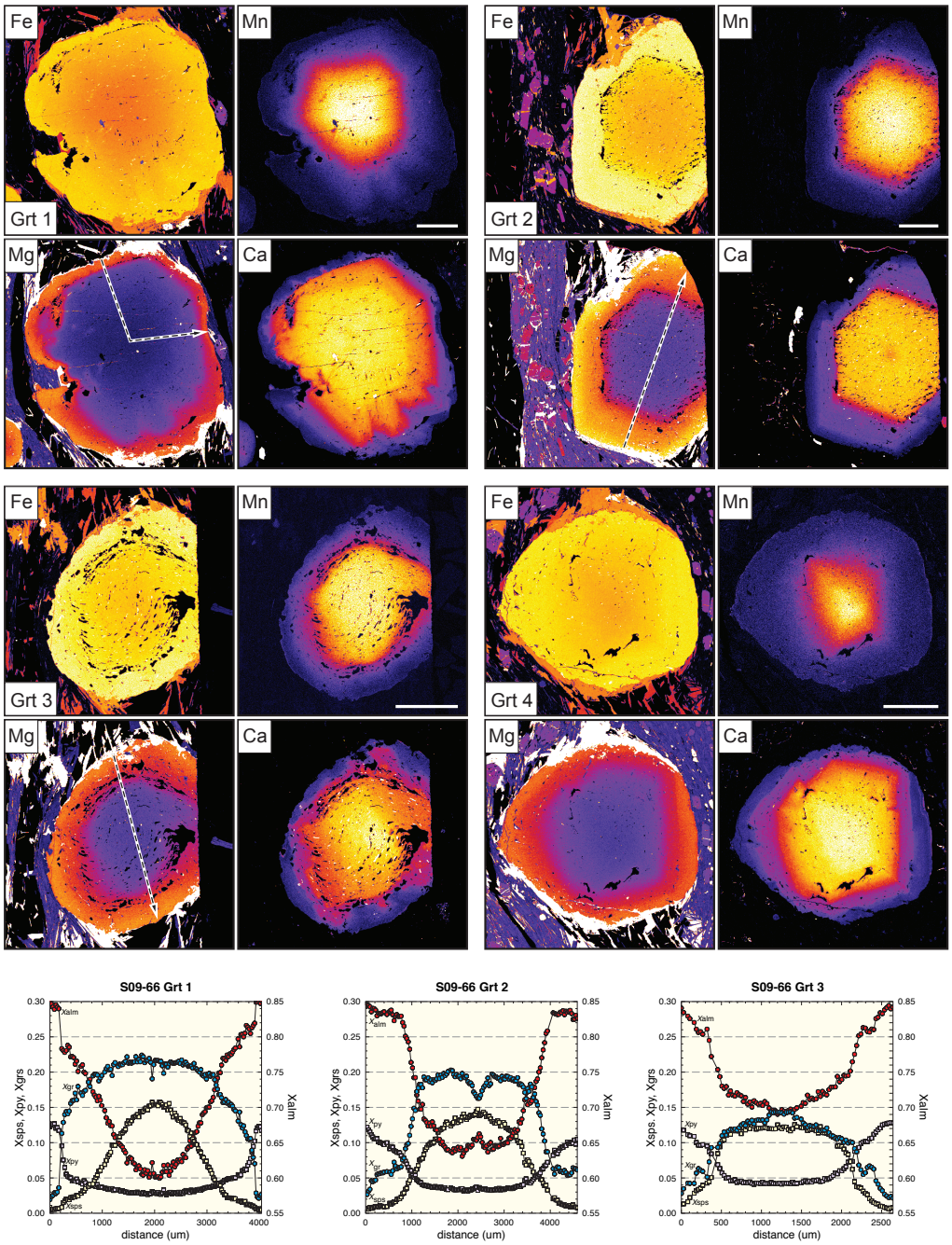

FIGURE 3.7. Garnets are characterized by high Mn, Ca and low Fe, Mg cores and high Fe, Mg and low Mn, Ca rims. Concentric compositional zones mirror external crystal faces of sub- to euhedral porphyroblasts. Note steep compositional gradients from core to rim in all garnets regardless of crystal radius. White bars represent 1 mm.

central region of the crystal. Such zoning relationships may be due to overgrowth of pre-Himalayan garnet cores or an otherwise complex P–T evolution. All garnet rims from this zone display a pronounced increase in X_{Sps} suggesting some amount of resorption.

Sample S09-63 preserves broadly similar microstructures to those from the MCT zone, in that

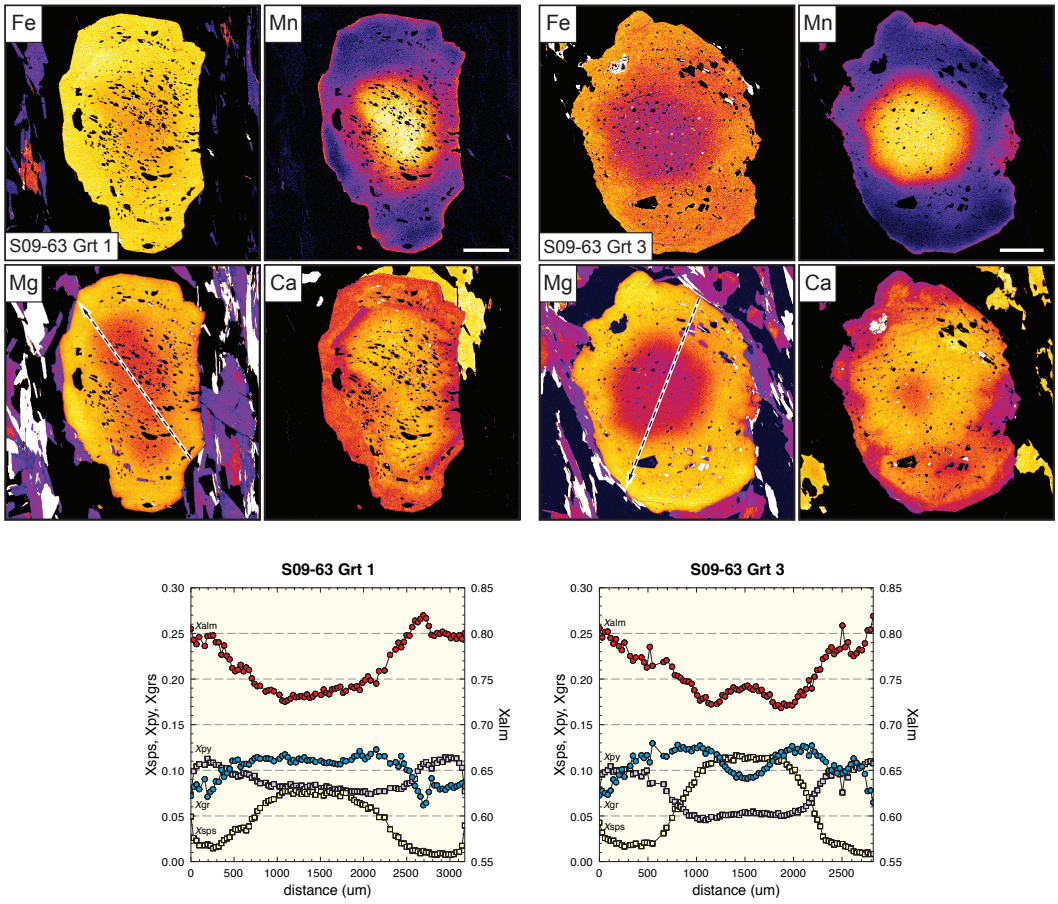

FIGURE 3.8. X-ray compositional maps and quantitative linescans of representative garnets from sample S09-63. The cause of the local minima of Ca, and local maxima of Fe and Mg is unknown. Rounding of high Mn core and increase of Mn at rims possibly indicating dissolution of minor amounts of garnet. Garnet rims are clearly distinguished from cores on the basis of sharp compositional changes. White bars represent 1 mm.

curvilinear inclusion-rich cores are overgrown by rims devoid of inclusions. Rims are distinct in X-ray compositional maps as well. At higher structural levels garnet zoning is consistent with diffusion upon cooling from peak-T (Fig. 3.9).

3.5 Thermodynamic modeling and P–T path analysis

The paucity of unequivocal porphyroblast–matrix relationships that can be related to the structural and metamorphic evolution, coupled with the modification or obliteration of growth zoning in garnet at mid–high structural levels in the eastern Sutlej Valley hinders attempts at extracting detailed quantitative information of the P–T history of samples from much of HHCS. However, observed textural and microstructural relationships from within the lower-grade MCT zone pro-

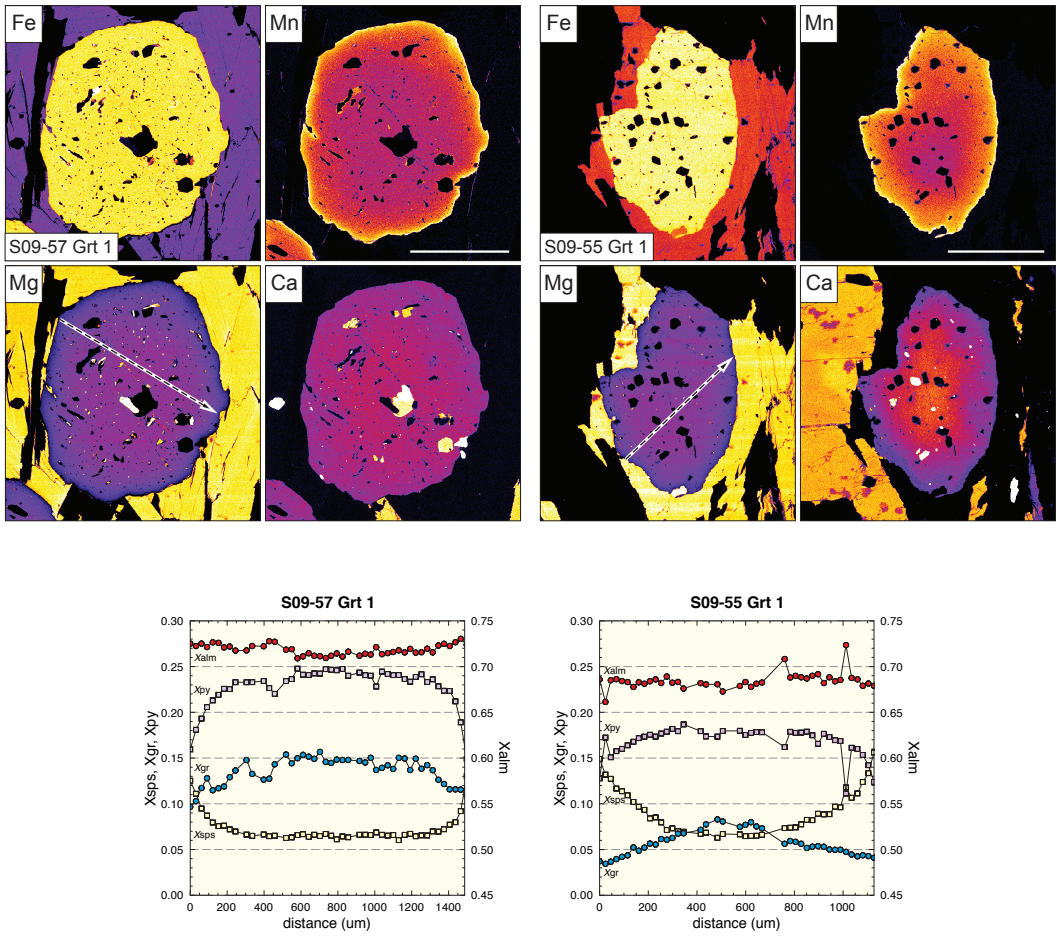

FIGURE 3.9. X-ray compositional maps of garnet from middle structural levels of the HHCS Zoning patterns reflect diffusion at high peak temperatures experienced by these rocks. White bars represent 1 mm.

vide significant insight into the thermal and deformation history experienced by rocks exposed at this structural position. Thus thermodynamic modeling was carried out in order to assess the significance of compositional zoning observed in garnet from sample S09-66 in terms of the *P*–*T* evolution of the sample. Modal analysis indicates the rock comprises: staurolite–4%; garnet–4%; biotite–14%; white mica–47%; quartz–30%; and ilmenite–2%.

A pure H_2O fluid phase was considered in excess in the modeling. The presence of graphite in the sample suggests that the actual fluid present during metamorphism was likely a mixed C-O-H fluid phase (Connolly and Cesare, 1993). At the *P*–*T* conditions relevant to the present study, this would likely shift phase boundaries a minor amount (see discussion in Tinkham and Ghent, 2005).

The inferred peak assemblage of St–Grt–Bt–Wm–Qtz–Ilm is stable over a relatively wide *P*–*T* range (550–650 °C and 3–9 kbar). Ubiquitous Ilm observed as inclusions in garnet and in the matrix

suggests $P < 9$ kbar for the entire burial history as rutile stability is restricted to $P > 9$ kbar at $T > 475$ °C. Plagioclase is predicted to be stable for maximum P between 8–4 kbar at $T > 600$ °C. Representative mineral chemical analyses are provided in Table 3.1.

TABLE 3.1. Representative mineral compositions of S09-66 recalculated by program AX.

Phase	SiO_2	TiO_2	Al_2O_3	Fe_2O_3	FeO	MnO	MgO	CaO	Na_2O	K_2O
garnet core (wt%)	36.31	0	20.99	1.21	26.10	6.71	0.65	7.30	0	0
(cpfu)	2.956	0	2.015	0.074	1.778	0.463	0.079	0.637	0	0
garnet rim	37.41	0	21.57	0	37.61	0.21	2.91	0.92	0	0
	2.994	0	2.035	0	2.518	0.014	0.347	0.079	0	0
staurolite	27.89	0.66	55.03	0	13.49	0.08	1.14	0	1.01	0
	7.631	0.136	17.752	0	3.087	0.019	0.337	0	0.536	0
biotite	36.28	1.59	19.54	0	20.94	0.02	8.36	0.01	0.22	8.86
	2.745	0.090	1.743	0	1.325	0.001	0.943	0.001	0.032	0.855
muscovite	45.47	0.50	36.02	0	1.19	0.01	0.66	0.01	1.01	9.37
	3.043	0.025	2.842	0	0.067	0.001	0.066	0.001	0.131	0.800
ilmenite	0.03	51.03	0	1.51	45.50	0.30	0.06	0	0	0
	0.001	0.985	0	0.029	0.976	0.007	0.002	0	0	0

3.5.1 Garnet core isopleth thermobarometry

Estimates of the P–T conditions of initial garnet nucleation and growth were obtained by plotting isopleths corresponding to measured core compositions of the linearly independent end members Alm, Grs, and Sps on the isochemical section determined for the XRF-derived bulk composition. Isopleths corresponding to measured values of the garnet core ($X_{Alm} = 0.60$, $X_{Sps} = 0.16$, $X_{Grs} = 0.22$) intersect tightly < 20 °C above the predicted equilibrium garnet-in line at ~510 °C, ~8.5 kbar (Fig. 3.10). The core isopleth intersection is near the Bt mode-zero line, in the field where Chl–Bt–Wm–Qtz–Ilm forms the stable assemblage. We interpret the tight intersection of core compositional isopleths of the largest garnets in the sample to indicate that relatively little of the early garnet growth history in this specimen is missing. Despite the good approximation of initial garnet growth, however, isopleths corresponding to the rim composition of garnet ($X_{Alm} = 0.84$, $X_{Sps} = 0.01$, $X_{Grs} = 0.03$) do not intersect in the model P–T space, indicating the effective bulk composition appropriate for late stages of garnet growth is different from that derived from XRF analysis of the hand sample (cf. Evans, 2004). To account for the shift of effective bulk composition

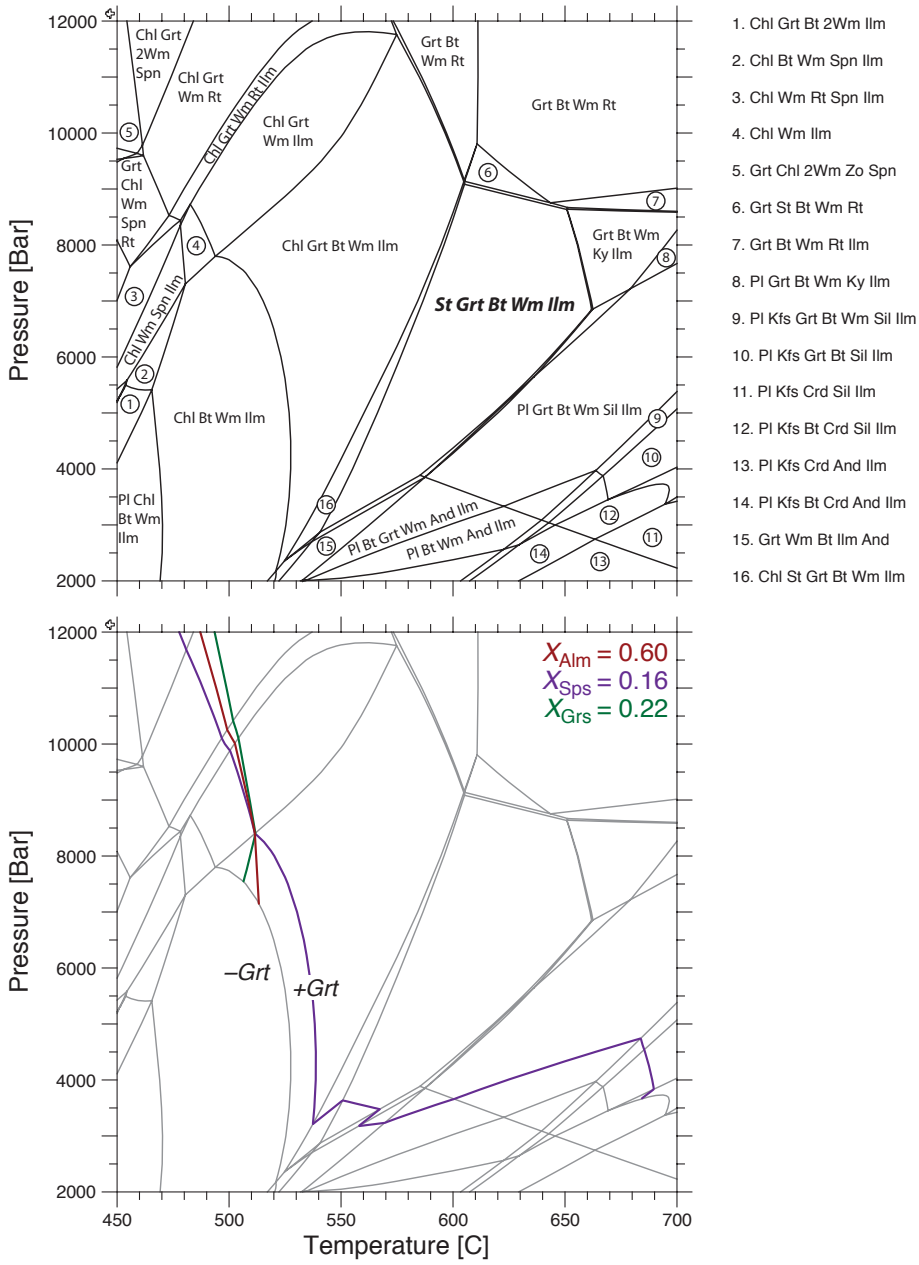

FIGURE 3.10. Equilibrium assemblage diagram for sample S09-66. (a) Phase stability fields for XRF-derived bulk composition. Peak assemblage (indicated by boldface) of St+Grt+Bt+Wm+Ilm (+Qtz+H_2O) is stable over a large region of P–T space, ∼550–650 °C and 3–9 kbar. (b) Intersection of linearly independent Alm, Sps, and Grs garnet end-member isopleths corresponding to measured core values. Tight intersection at ∼510 °C and 8.5 kbar suggests much of the garnet growth history is preserved in this specimen. Bulk chemistry used in the model (mol.%): MnO:0.10–Na_2O:0.66–CaO:0.56–K_2O:4.51–FeO:7.78–MgO:3.85–Al_2O_3:17.14–SiO_2:64.70–TiO_2:0.71.

during the metamorphic evolution we must consider fractional garnet crystallization during the metamorphic evolution of sample S09-66.

3.5.2 Garnet zoning and *P*–*T*–*X* evolution

Due to the importance of changing effective bulk composition during prograde metamorphism, we chose to model fractional crystallization of garnet using the Gibbs free energy minimization program THERIAK. The program calculates the phases, modal proportions, molar volumes, and other thermodynamic quantities at points along a user-defined P–T path assuming maintenance of thermodynamic equilibrium at every point on the path. We modeled garnet fractional crystallization by removing 100% of elements sequestered into garnet grown at every point where garnet was in the equilibrium assemblage. Additionally, H_2O liberated by dehydration along the path was removed from the bulk composition. Such an approach allows modeling of non-isochemical metamorphic rock evolution (e.g., Konrad-Schmolke et al., 2011). The amount of garnet grown at each step and its composition were used to model garnet growth. We chose a P–T path that crossed the equilibrium garnet-in reaction (i.e., assumed no reaction overstep). The total volume of garnet grown throughout the input path was converted to crystal radius assuming a spherical crystal geometry. A final crystal radius of 2.43 mm was prescribed for direct comparison with the largest crystal observed in thin section. Model garnet rim compositions were not modified during the retrograde path.

Fractional crystallization of garnet is path-dependent. We manually adjusted the input P–T path until the resulting garnet zoning profile resembled the measured compositional profile of one of the largest garnets in thin section, and calculated modal proportions closely matched point-counted modes. Subtle variations in the path may produce a locally better fit to the observed garnet zoning, however, an attempt at sensitivity analysis on input paths gives us confidence that the general geometry and position in P–T space is a robust approximation for the specimen.

The initial geometry of the P–T path is largely controlled by the steep dP/dT slopes of almandine, pyrope, and grossular phase components in garnet (Fig. 3.11). The early portion of the path thus corresponds to burial of ∼1 kbar and ∼20 °C T increase. Heating and decompression follows the initial burial stage to the metamorphic peak of ∼600 °C, 6.5 kbar. The thermal maximum is followed by cooling and continued exhumation (Fig. 3.10).

Figure 3.12 shows the predicted evolution of phase abundance along the prograde portion of the P–T path. Fractional garnet crystallization and H_2O liberation on the prograde path signifi-

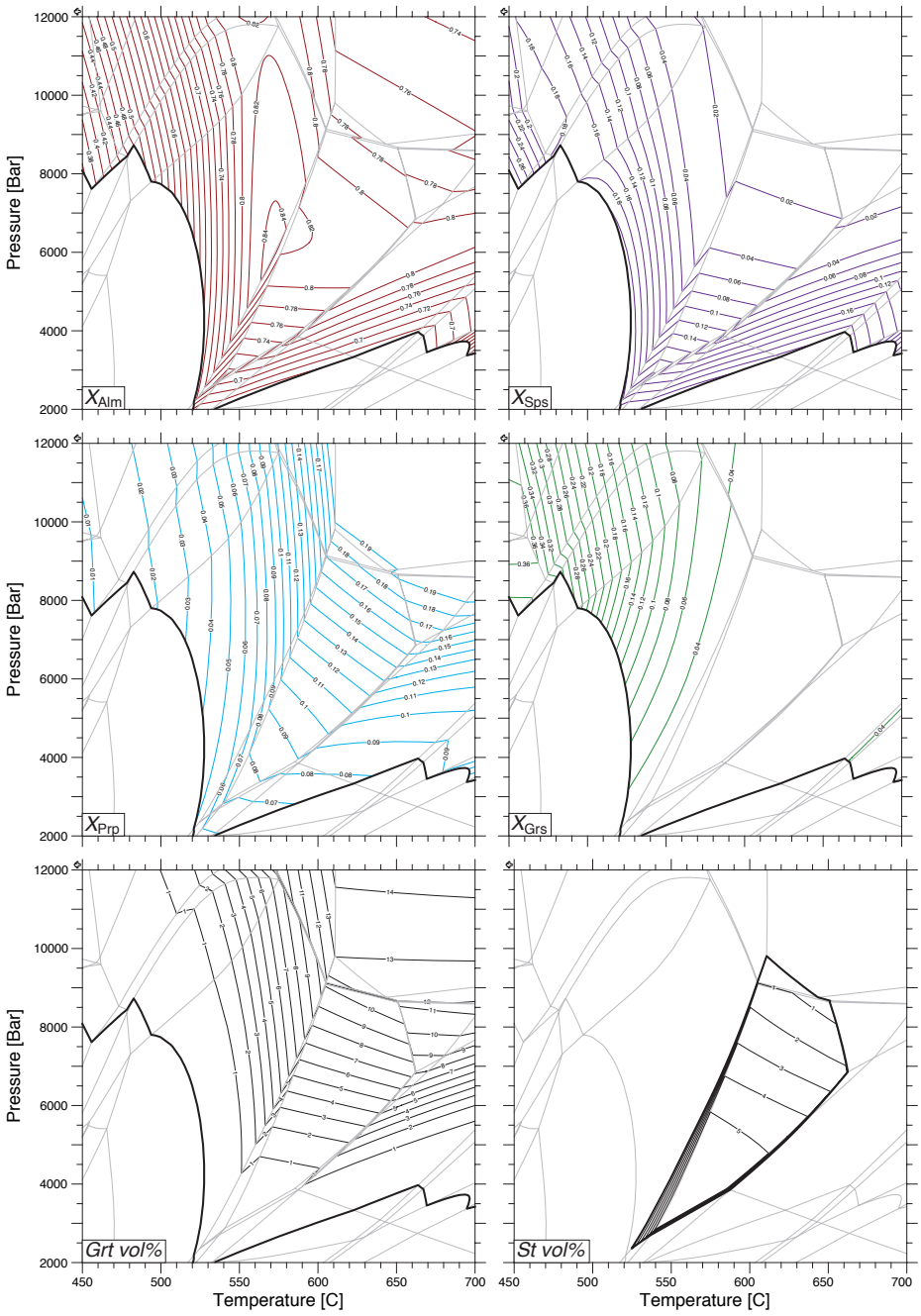

FIGURE 3.11. Calculated isopleths for Alm, Sps, Prp, and Grs garnet end-members, and modal proportion of both garnet and staurolite for XRF-derived bulk composition of S09-66. Note all end-members display steep dP/dT slopes at temperatures below staurolite zone. This is the dominant control on where garnet of measured composition in sample S90-66 reacts into the model assemblage.

cantly modifies the effective bulk composition of the sample. Therefore, we calculated equilibrium assemblage diagrams for the chosen sample after the last increment of garnet growth (Fig. 3.13). Element fractionation along the P–T path leads to significant modification of stable phase topology compared to that for the XRF-derived bulk composition. The major changes in the predicted phase

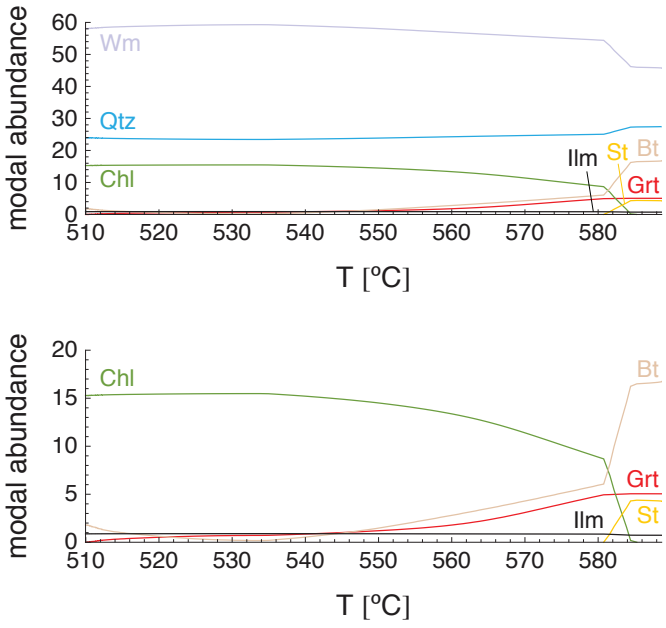

FIGURE 3.12. Evolution of modal abundance of phases along prograde portion of P–T path. Upper panel shows abundance of all phases. Lower panel is detail of lower portion shown above. In the model Grt growth ceases when St reacts into the assemblage. Bt+St grow at the expense of Chl+Wm.

stabilities between the fractionated and unfractionated bulk are the change in position of garnet-in and lack of a free fluid phase at low P–T; stability of staurolite to higher P; and the stability of chloritoid at low-T and moderate P. Positions of Fe-Ti oxide stability at $T \geq 550$ °C and terminal stability of staurolite ($T \sim 660$ °C) are largely unchanged.

Fractional garnet crystallization model results

General compositional zoning trends of the model garnet match the observed compositional zoning profile of large garnet from sample S09-66 (Fig. 3.14). The core displays relatively flat to slightly increasing Fe, Mg, and flat to decreasing Ca and Mn. The steep gradients observed in all components in zone 2 is apparent in the model crystal, as well as the flat to increasing Fe, Mg, and flat to decreasing Ca and Mn trends in zone 3. In the model, Mn is completely depleted at the garnet rim, whereas ∼1–2 mole % spessartine was measured in the sample. The model crystal core contains higher concentrations of Mn and lower Fe due to extrapolation of the path to lower P–T conditions for initiation of garnet growth at the equilibrium garnet-in reaction. Thus, our P–T path begins at a position which lies several degrees down-temperature of the core isopleth intersection (Fig. 3.10). X_{Sps} isopleths are roughly parallel to the modal proportion of garnet and nearly

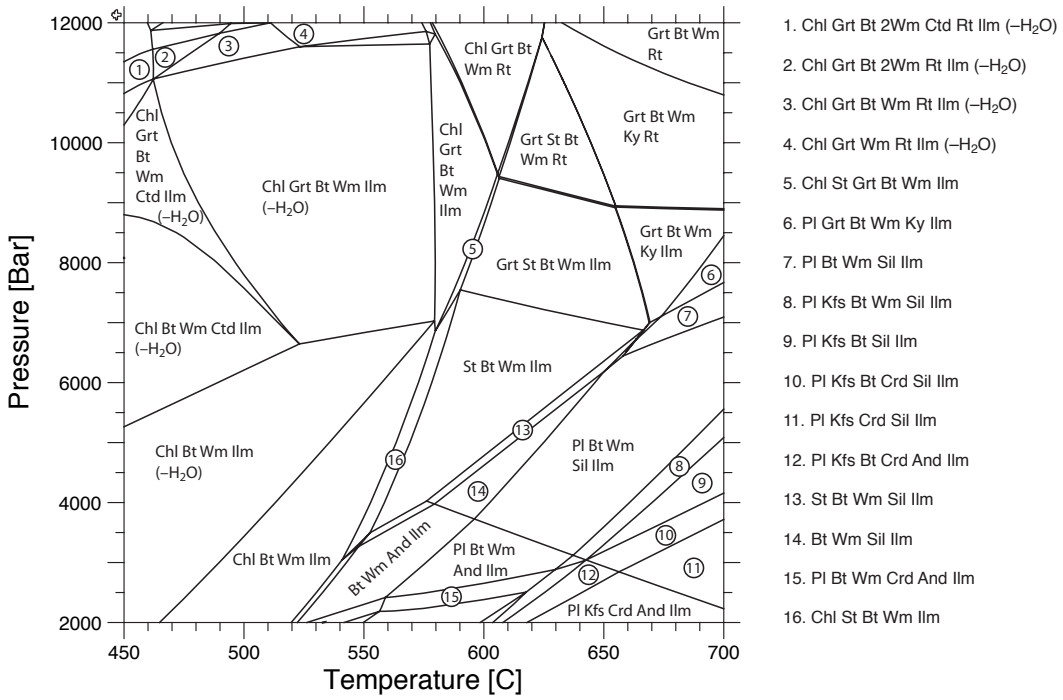

FIGURE 3.13. Equilibrium assemblage diagram for fractionated bulk composition. Bulk at the final P–T conditions of Grt stability. Positions of Grt-in is significantly different from that calculated for the XRF-derived bulk composition, but Fe–Ti oxide and terminal St stability are largely unchanged. Fractionated bulk chemistry (mol.%): MnO:0.0–Na_2O:0.66–CaO:0.34–K_2O:4.51–FeO:5.27–MgO:3.64–Al_2O_3:16.13–SiO_2:61.66–TiO_2:0.71.

perpendicular to the P–T path leading to high Mn content in the model garnet core. The model also predicts higher Fe, and lower Mg and Ca concentrations at the rims of garnet. Despite the misfit of absolute end-member concentrations, however, calculated compositional zoning for garnet grown on the chosen P–T path reasonably approximates the measured trends, and predicted modal proportions of phases are in good agreement with observation (Table. 3.2; Fig. 3.15).

TABLE 3.2. Measured and calculated mineral modes.

	Modal abundance (%)	
Phase	Measured	Calculated
garnet	3.62	5.04
staurolite	3.91	4.25
biotite	14.05	16.33
muscovite	46.62	46.09
quartz	29.90	27.48
ilmenite	1.91	0.82

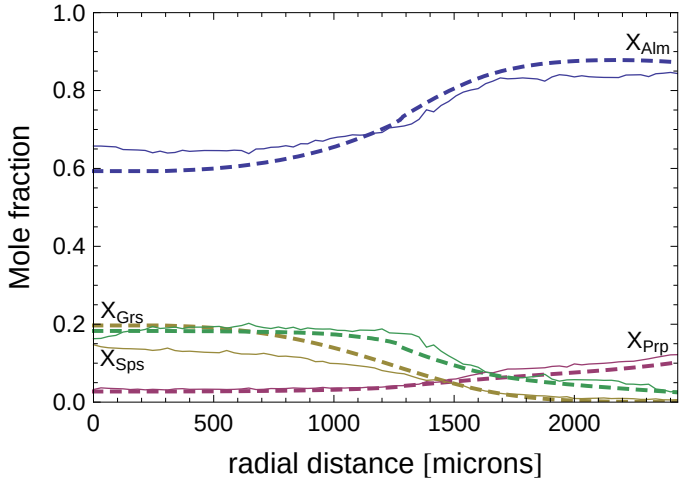

FIGURE 3.14. Calculated rim–core garnet compositional zoning profile for fractional crystallization along P–T path. All elements sequestered into garnet and any H_2O liberated at every step on the P–T path removed from the bulk composition. Absolute values of components do not everywhere match measured composition, but overall trend of predicted zoning agrees well with measured zoning trends.

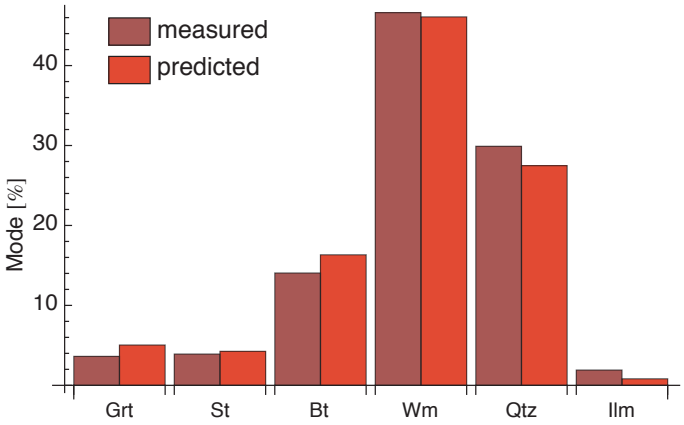

FIGURE 3.15. Comparison of measured and predicted mineral modes for sample S09-66.

3.5.3 Effect of diffusion on zoning patterns

A major assumption of this work is that the zoning observed in S09-66 garnet is related to growth on the prograde path and has not been significantly modified during or after growth by intracrystalline diffusion. Acceptance of this assumption allows us to interpret the observed compositional zonation in terms of changes in P, T, and bulk composition during garnet growth. To test the validity of this critical assumption we used the methodology discussed by Caddick et al. (2010) to calculate the effect of simultaneous growth of, and major element cation diffusion in, garnet along the chosen P–T path. The duration of the P–T path was modeled over four orders of magnitude (total durations of 10^6–10^9 yr) to assess the sensitivity of our model compositional profile at peak-T appropriate

for the specimen (∼600 °C).

Diffusion modeling results

The length scale of diffusion of divalent cations in garnet is predicted to be small for the low peak-T appropriate for sample S09-66 and timescale available for Himalayan metamorphism (e.g., Carlson, 2006; Caddick et al., 2010). Results of the modeling confirm that minor changes in the absolute values of concentration of end-members are expected to occur even for very low heating and cooling rates associated with long durations of burial, heating, and exhumation (Fig. 3.16). Thus these results, and the absence of compelling evidence for disequilibrium garnet growth at the

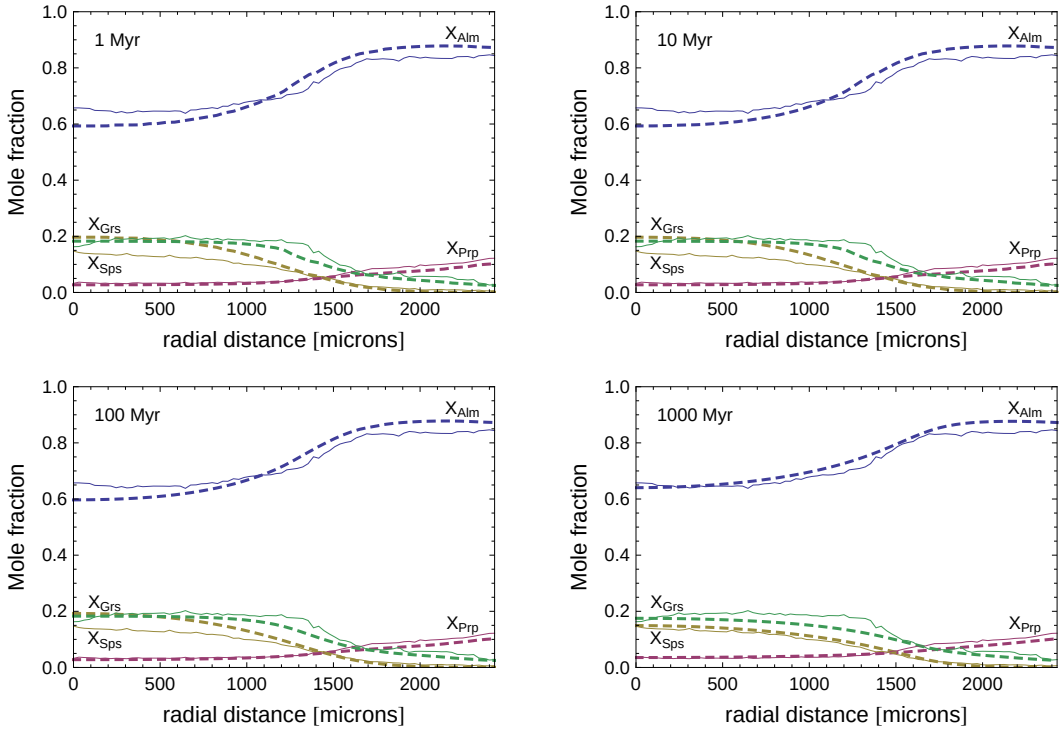

FIGURE 3.16. Comparison of rim–core garnet compositional profiles for 10^6, 10^7, 10^8, and 10^9 year duration of burial and exhumation. At the low peak-T attained by sample S09-66 cation diffusion does not modify core compositions at reasonable timescales for the Himalayan orogen (i.e., ∼50 Myr). Even for the extreme case of burial and exhumation path of 1000 Myr duration core Mn and Fe are modified by ∼5 mole percent.

thin section scale, suggest that garnet compositional zoning provides a relatively robust indication of the P–T–X evolution of sample S09-66 (Figs. 3.10–3.14).

3.6 Discussion

3.6.1 Model caveats

Our model garnet zoning is similar to that observed in large garnets in S09-66 suggesting the general geometry of the path is appropriate for rocks at the structural level of the MCT in the eastern Sutlej Valley. However, there are a number of factors involved in the modeling that should be addressed. The most significant are discussed below.

Constraints on model *P*–*T*–*t* path

Metamorphism of the HHCS is interpreted to have been a response to burial and subsequent heating related to crustal thickening associated with collision of India and Asia. This places a maximum age constraint on the beginning of burial of ∼54 Ma (Searle et al., 2007). Vannay et al. (2004) have determined $^{40}Ar/^{39}Ar$ muscovite cooling ages of ∼20–15 Ma for HHCS rocks in the Sutlej Valley with a younger age of ∼10 Ma for rocks at the MCT, which place a minimum age constraint on metamorphism and cooling through ∼450 °C. Thus the entire burial and exhumation history must span less than ∼40 Myr.

Limited geochronology exists for the HHCS of the Sutlej Valley, particularly for the earliest burial and heating phase. Caddick (unpublished PhD thesis) inferred peak-T at approximately 17 Ma based on matrix monazite U–Pb data for samples collected near the location of our specimen S09-66. This age coupled with the $^{40}Ar/^{39}Ar$ cooling ages imply cooling rates of ∼20 °C Myr^{-1} for rocks in the immediate MCT hanging wall in eastern Sutlej Valley. Assuming heating of sample S09-66 commenced with the initiation of continental collision of India and Asia (for maximum duration for diffusion to operate) gives a minimum heating rate during prograde garnet growth of ∼2–3 °C Myr^{-1}. This ignores time required for burial of the sample to ∼8 kbar (∼30 km depth) following initiation of collision and thus may severely underestimate likely heating rates for HHCS rocks. Thus, the maximum duration of burial and exhumation of sample S09-66 lies well between the 1 and 100 Myr path durations calculated in the diffusion modeling, and may be closer to the 10 Myr duration path. In any case, compositional zoning for 4–5 mm diameter garnets is clearly unaffected for the relevant temperatures and timescales under consideration.

Non-uniqueness of model path

As mentioned above, garnet fractional crystallization is path-dependent. In particular, contours of end-member compositional isopleths clearly demonstrate the composition of initially nucleated garnet is sensitive to the P–T conditions of initial garnet growth (see Fig. 3.11). Despite the path-dependent nature of fractional garnet crystallization we find that the P–T conditions toward the end of the paths we investigated have significantly less influence on later-crystallized garnet compositions. This is due in large part to the rapid radial growth of garnet early in the P–T evolution, as garnet radius and volume are related by a cubic relationship. Thus, the early stage of the P–T evolution is largely required to be similar to our chosen path since the predicted garnet zoning becomes less like the measured garnet compositional zoning if early P–T conditions or path trajectory vary significantly from that shown. Ultimately the general geometry of the initial and intermediate portions of the path are necessary to produce garnet compositions similar to those observed in the analyzed garnets.

3.6.2 Tectonic interpretation

Despite the caveats outlined above and potential limitations of the kind of (equilibrium) thermodynamic analysis employed in this study, our best-fit P–T path produces striking similarities in predicted garnet compositional zonation trends and modal phase proportions. The chosen path is consistent with burial of MCT footwall rocks, conductive heating, and subsequent exhumation by incorporation into a southwestward migrating deformation front (MCT zone). We envision a scenario whereby rocks currently exposed in the MCT zone were initially located to the SW (in the footwall) of an early MCT ductile shear zone. As the deformation front propagated from NE to SW, sample S09-66 was first buried and then entrained in the upper portion of the shear zone where it continued to heat by conduction from hotter overlying rocks. Top-SW shear continued and sample S09-66 was progressively exhumed toward the synorogenic topographic surface as the MCT zone was simultaneously cooled by juxtaposition and accretion of cooler footwall rocks.

The P–T path determined for MCT zone sample S09-66 does not closely resemble the only other published P–T history inferred for HHCS rocks of the Sutlej Valley. In that study Vannay and Grasemann (1998) applied the Gibbs method (Spear and Selverstone, 1983; Spear, 1993) to

infer a P–T path for migmatitic HHCS rocks near the top of the section. The resulting P–T path consisted of a period of isobaric heating at ∼8 kbar followed by cooling and decompression, forming a distinct 'hairpin' closure in P–T space. This path formed the basis for a tectonic model for the area incorporating extrusion of the HHCS wedge through a (fixed) thermal architecture of foreland-dipping isotherms with little or no relative vertical displacement between HHCS rocks throughout the section, ultimately resulting in the general shear extrusion of the crystalline core. Our P–T path may potentially support such an extrusion model if the lower boundary zone were permitted to migrate in space and time.

A path similar to the one derived here has been produced in orogen-scale continuum thermal–mechanical geodynamic models (Channel Flow model HT1) by Jamieson et al. (2004) for rocks now exposed in the immediate footwall to their model MCT. The particles that experienced this type of path and are predicted to be presently exposed at Earth's surface were assigned to the model Lesser Himalaya as they originated some 1500 km proward (i.e., toward the foreland) of the model suture (cf. path L3; their fig. 6). The P–T path calculated for sample L3 attains slightly lower peak-P (7.0 kbar) and higher peak-T (656 °C), but the geometry of the path bears a striking similarity to that independently inferred for sample S09-66. We have no way to infer where exactly sample S09-66 originated from within the Indian crust or quantify the lateral path experienced by it, but the striking similarity between our inferred tectonic evolution for MCT zone rocks and paths predicted for rocks in reasonably similar positions in the orogen suggest that the Channel Flow model may effectively capture first-order processes during the burial and exhumation of rocks from the HHCS in the Sutlej Valley.

3.7 Conclusions

1. An inverted metamorphic field temperature gradient exists in the HHCS of eastern Sutlej Valley. Near-peak-T increases from ∼600 °C at the base, to ∼750 °C in the core of the HHCS, and may decrease slightly to ∼660–700° C at the top of the 10 km thick section. Pressure at peak-T appears to be nearly constant at ∼8–8.5 kbar, defining an isobaric T gradient.

2. Porphyroblast / matrix relationships are best preserved at the lowest structural positions of

the HHCS and are particularly well-developed in staurolite zone schists within the MCT zone. Preserved relationships indicate garnet initially overgrew an early S1 fabric, and continued to grow during early D2 deformation and development of the S2 transposition fabric related to reverse-sense motion on the MCT. Deformation outlasted metamorphic recrystallization.

3. Zoning observed in MCT zone garnet is consistent with prograde growth, with little or no modification by cation diffusion or resorption on the retrograde path.

4. Salient features of observed compositional zoning in MCT zone garnets were successfully reproduced by modeling garnet fractional crystallization along a P–T path with distinct geometry. The path must include an initial burial phase with modest T increase, followed by a phase of heating during decompression, and terminates with a phase of cooling and exhumation.

5. Our best-fit P–T path is best explained by incorporation of footwall rocks into the south-westward propagating MCT deformation front and extrusion and exhumation during Late Miocene penetrative deformation associated with top-SW shearing.

6. Observed compositional zoning of MCT zone garnet, with relatively sharp corners in Mn concentration at intersections of crystal faces implies rapid timescales of metamorphism and insufficient time at near-peak-T for significant diffusion to occur. Quantitative cation diffusion modeling does not place additional constraints on likely duration of burial and exhumation for these rocks.

References

Andersen, T., 1984. Inclusion patterns in zoned garnets from Magerøy, north Norway. Mineralogical Magazine 48, 21–26.

Beaumont, C., Jamieson, R.A., Nguyen, M.H., Medvedev, S., 2004. Crustal channel flows: 1. Numerical models with applications to the tectonics of the Himalayan-Tibetan orogen. Journal of Geophysical Research 109, B06406.

Caddick, M., Bickle, M., Harris, N., Holland, T., Horstwood, M., Parrish, R., Ahmad, T., 2007. Burial and exhumation history of a Lesser Himalayan schist: Recording the formation of an inverted metamorphic sequence in NW India. Earth and Planetary Science Letters 264, 375–390.

Caddick, M., Bickle, M., Harris, N., Parrish, R., 2006. Contrasting depth–temperature–time histories of the High and Lesser Himalaya of NW India. Journal of Asian Earth Sciences 26, 129.

Caddick, M.J., Konopásek, J., Thompson, A.B., 2010. Preservation of garnet growth zoning and the duration of prograde metamorphism. Journal of Petrology 51, 2327–2347.

de Capitani, C., Brown, T.H., 1987. The computation of chemical equilibrium in complex systems containing non-ideal solutions. Geochimica et Cosmochimica Acta 51, 2639–2652.

de Capitani, C., Petrakakis, K., 2010. The computation of equilibrium assemblage diagrams with Theriak/Domino software. American Mineralogist 95, 1006–1016.

Carlson, W.D., 2006. Rates of Fe, Mg, Mn, and Ca diffusion in garnet. American Mineralogist 91, 1–11.

Chambers, J., Caddick, M., Argles, T., Horstwood, M., Sherlock, S., Harris, N., Parrish, R., Ahmad, T., 2009. Empirical constraints on extrusion mechanisms from the upper margin of an exhumed high-grade orogenic core, Sutlej valley, NW India. Tectonophysics 477, 77–92.

Coggon, R., Holland, T., 2002. Mixing properties of phengitic micas and revised garnet-phengite thermobarometers. Journal of Metamorphic Geology 20, 683–696.

Connolly, J., Cesare, B., 1993. C-O-H-S fluid composition and oxygen fugacity in graphitic metapelites. Journal of metamorphic geology 11, 379–388.

Evans, T., 2004. A method for calculating effective bulk composition modification due to crystal fractionation in garnet-bearing schist: implications for isopleth thermobarometry. Journal of Metamorphic Geology 22, 547–557.

Furhman, M., Lindsley, D., 1988. Ternary-feldspar modelling in thermobarometry. Am. Mineral 37, 201–215.

Grasemann, B., Fritz, H., Vannay, J.C., 1999. Quantitative kinematic flow analysis from the Main Central Thrust Zone (NW-Himalaya, India): implications for a decelerating strain path and the extrusion of orogenic wedges. Journal of Structural Geology 21, 837–853.

Hodges, K.V., 2000. Tectonics of the Himalaya and southern Tibet from two perspectives. Geological Society of America Bulletin 112, 324–350.

Holland, T., Powell, R., 1998. An internally consistent thermodynamic data set for phases of petrological interest. Journal of metamorphic Geology 16, 309–343.

Hollister, L.S., 1970. Origin, mechanism, and consequences of compositional sector-zoning in staurolite. American Mineralogist 55, 742–766.

Jamieson, R., Beaumont, C., Medvedev, S., Nguyen, M., 2004. Crustal channel flows: 2. Numerical models with implications for metamorphism in the Himalayan-Tibetan orogen. Journal of Geophysical Research 109, B06407.

Kohn, M.J., 2004. Oscillatory-and sector-zoned garnets record cyclic (?) rapid thrusting in central Nepal. Geochemistry, Geophysics, Geosystems 5.

Kohn, M.J., 2008. P-T-t data from central Nepal support critical taper and repudiate large-scale channel flow of the Greater Himalayan Sequence. Geological Society of America Bulletin 120, 259–273.

Konrad-Schmolke, M., Obrien, P.J., Zack, T., 2011. Fluid migration above a subducted slabconstraints on amount, pathways and major element mobility from partially overprinted eclogite-facies rocks (Sesia Zone, Western Alps). Journal of Petrology 52, 457–486.

Kretz, R., 1983. Symbols for rock-forming minerals. American Mineralogist 68, 277.

Kruhl, J., 1998. Reply: Prism- and basal-plane parallel subgrain boundaries in quartz: A microstructural geothermabarometer. Journal of Metamorphic Petrology 16, 142–146.

Law, R.D., Searle, M.P., Simpson, R.L., 2004. Strain, deformation temperatures and vorticity of flow at the top of the Greater Himalayan Slab, Everest Massif, Tibet. Journal of the Geological Society of London 161, 305–320.

Le Fort, P., 1996. Evolution of the himalaya. In: Yin, A., Harrison, T. (Eds.), The Tectonic Evolution of Asia. Cambridge University Press, New York, pp. 95–109.

Mahar, E.M., Baker, J., Powell, R., Holland, T., Howell, N., 1997. The effect of Mn on mineral stability in metapelites. Journal of Metamorphic Geology 15, 223–238.

Manickavasagam, R.M., Jain, A.K., Singh, S., Asokan, A., 1999. Metamorphic evolution of the northwest Himalaya, India: Pressure-temperature data, inverted metamorphism, and exhumation in the Kashmir, Himachal, and Garhwal Himalayas. In: Macfarlane, A., Sorkhabi, R.B., Quade, J. (Eds.), Himalaya and Tibet: Mountain Roots to Mountain Tops, Geological Society of America Special Paper 328.

Marquer, D., Chawla, H., Challandes, N., 2000. Pre-alpine high grade metamorphism in High Himalaya. Eclogae Geologicae Helvetiae 93, 207–220.

Miller, C., Klötzli, U., Frank, W., Thöni, M., Grasemann, B., 2000. Proterozoic crustal evolution in the NW Himalaya (India) as recorded by circa 1.80 Ga mafic and 1.84 Ga granitic magmatism. Precambrian Research 103, 191–206.

Moynihan, D., Pattison, D., 2013. An automated method for the calculation of P–T paths from garnet zoning, with application to metapelitic schist from the Kootenay Arc, British Columbia, Canada. Journal of Metamorphic Geology .

Powell, R., Holland, T., 1994. Optimal geothermometry and geobarometry. American Mineralogist 79, 120.

Richards, A., Argles, T., Harris, N., Parrish, R., Ahmad, T., Darbyshire, F., Draganits, E., 2005. Himalayan architecture constrained by isotopic tracers from clastic sediments. Earth and Planetary Science Letters 236, 773–796.

Searle, M., Waters, D., Dransfield, M., Stephenson, B., Walker, C., Walker, J., Rex, D., 1999. Thermal and mechanical models for the structural and metamorphic evolution of the Zanskar High Himalaya. Geological Society, London, Special Publications 164, 139.

Searle, M.P., Stephenson, B., Walker, J.D., Walker, C.B., 2007. Restoration of the Western Himalaya: implications for the metamorphic protoliths, thrust and normal faulting, and channel flow models. Episodes 304, 242–257.

Spear, F.S., 1993. Metamorphic Phase Equilibria and Pressure-Temperature-time Paths. Mineralogical Society of America, Washington, D.C.

Spear, F.S., Selverstone, J., 1983. Quantitative P-T paths from zoned minerals: Theory and tectonic applications. Contributions to Mineralogy and Petrology 83, 348–357.

Thakur, S., Tripathi, K., 2008. Regional metamorphism in the Haimanta Group of rocks, Sutlej river valley, NW Himalaya, India. Current Science 95, 104.

Tinkham, D.K., Ghent, E.D., 2005. Estimating PT conditions of garnet growth with isochemical phase-diagram sections and the problem of effective bulk-composition. The Canadian Mineralogist 43, 35–50.

Vannay, J.C., Grasemann, B., 1998. Inverted metamorphism in the High Himalaya of Himachal Pradesh NW India: phase equilibria versus thermobarometry. Schweizerische Mineralogische und Petrographische Mitteilungen 78, 107–132.

Vannay, J.C., Grasemann, B., 2001. Himalayan inverted metamorphism and syn-convergence extension as a consequence of a general shear extrusion. Geological Magazine 138, 253–276.

Vannay, J.C., Grasemann, B., Rahn, M., 2004. Miocene to Holocene exhumation of metamorphic crustal wedges in the NW Himalaya: Evidence for tectonic extrusion coupled to fluvial erosion: Evidence for tectonic extrusion coupled to fluvial erosion. Tectonics 23, doi:10.1029/2002TC001429.

Vannay, J.C., Sharp, Z.D., Grasemann, B., 1999. Himalayan inverted metamorphism constrained by oxygen isotope thermometry. Contributions to Mineralogy and Petrology 137, 90–101.

White, R., Powell, R., Holland, T., Worley, B., 2000. The effect of TiO_2 and Fe_2O_3 on metapelitic assemblages at greenschist and amphibolite facies conditions: mineral equilibria calculations in the system K_2O-FeO-MgO-Al_2O_3-SiO_2-H_2O-TiO_2-Fe_2O_3. Journal of Metamorphic Geology 18, 497–512.

Wiesmayr, G., Grasemann, B., 2002. Eohimalayan fold and thrust belt: Implications for the geodynamic evolution of the NW-Himalaya (India). Tectonics 21, 1058.

Chapter 4

Deformation temperatures at the top of the Higher Himalayan Crystallines, Zanskar, NW India

Donald W. Stahr, III[1], Richard D. Law[1]

[1]*Department of Geosciences, Virginia Polytechnic Institute and State University, Blacksburg, VA, 24061, USA*

This article may be submitted to *Journal of Structural Geology* for publication.

Abstract

We report new quantitative deformation temperature data, based on quartz *c*-axis fabric opening angles, for Higher Himalayan Crystalline Sequence (HHCS) rocks in the Zanskar region of NW India. Quartz crystallographic fabrics developed during penetrative deformation associated with Miocene normal-sense motion on the Zanskar Shear Zone (ZSZ), the westernmost strand of the South Tibetan Detachment System of normal faults. Quartz fabrics record an apparent temperature gradient of ~275 °C km^{-1} for the interval 300–500 m structurally beneath the detachment. Microstructural criteria such as inferred quartz recrystallization regime and feldspar deformation microstructures, support the elevated deformation temperatures indicated by quartz petrofabric analysis. Dip-slip displacement estimates of 15–40 km based on a simple geometric model of heterogeneous simple shear parallel to the overlying detachment supports earlier estimates from barometric data collected from the HHCS in SE Zanskar. Our results support models for extrusion of uppermost HHCS material from mid-crustal levels during moderate- to high-temperature top-SW shearing associated with Miocene normal-sense motion on the ZSZ.

4.1 Introduction

The highest-grade metamorphic rocks in the Himalayan orogen, the Higher Himalayan Crystalline Sequence (HHCS), also referred to as the Greater Himalayan Sequence, are exposed as a north-dipping ~5–30 km thick slab of penetratively deformed and metamorphosed igneous and sedimentary rocks typically flanked by low-grade or unmetamorphosed sedimentary rocks (Fig. 4.1). The HHCS is bounded everywhere by tectonic contacts; at the base by the Main Central Thrust (MCT), and at the top by the South Tibetan Detachment System (STDS) of normal faults. The nature of the crustal-scale high strain zones bounding the HHCS has received considerable attention in recent literature, and the geometry, timing, and kinematics of these structures is now reasonably understood along much of the length of the orogen (e.g., Law et al., 2006, and citations therein). The MCT is characterized by a zone of inverted metamorphism and is commonly interpreted to be the lower boundary of an extruded wedge or channel of mid-crustal material (e.g., Searle and Rex, 1989; Grujic et al., 1996; Vannay and Grasemann, 2001; Searle et al., 2008). The STDS forms the structural top of the wedge and was active simultaneously with the MCT (e.g., Godin et al., 2006, and references therein). Metamorphic isograds observed at upper levels of the HHCS in the immediate footwall of the STDS are consistently right-way-up. The coupled normal- and reverse-sense motion on these ductile shear zones facilitated rapid extrusion and exhumation of the mid-crustal HHCS during Miocene times (e.g., Hodges, 2000).

The inverted and right-way-up isograd sequences associated with the MCT and STDS form a

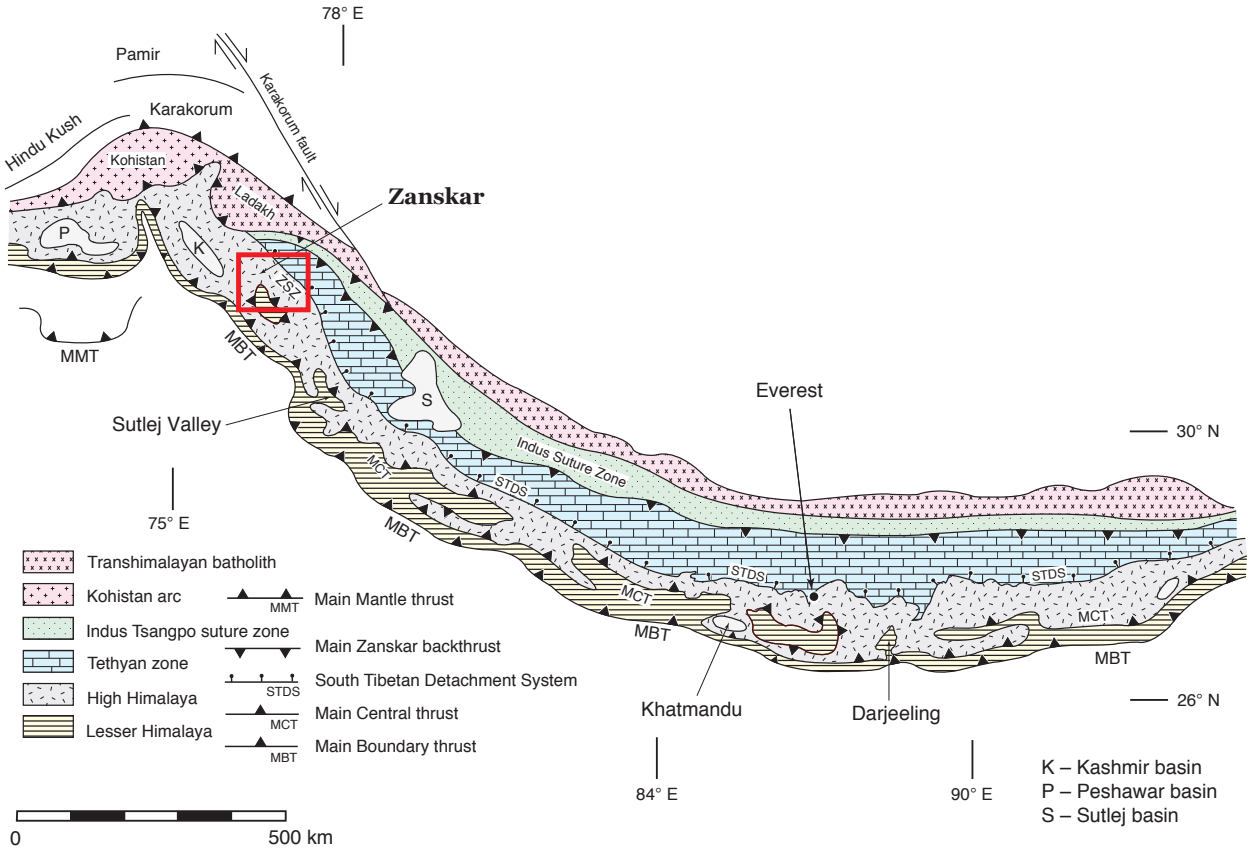

FIGURE 4.1. Simplified tectonic map of the Himalayan orogen showing the distribution of main tectonostratigraohic units and location of the Sutlej valley area discussed in text. The Higher Himalayan Crystalline Series is bounded below by the Main Central Thrust (MCT) and above by the South Tibetan Detachment System (STDS). Inset box indicates location of Fig. 4.2. MBT–Main Boundary Thrust; MMT–Main Mantle Thrust; ZSZ–Zanskar Shear Zone; K–Kashmir basin; P–Peshawar basin; S–Sutlej basin; Modified from Law et al. (2004).

large fold closure in the Zanskar region of NW India (Searle and Rex, 1989). The isograd sequences are strongly condensed (telescoped) at both lower and upper margins suggesting that deformation and shearing post-dated growth of the index mineral assemblages that define the isograds; however, no quantitative data exist on the conditions attending shearing on the STDS in this region, so it remains unknown whether deformation occurred at elevated temperatures immediately following metamorphic peak and 'freezing-in' of the isograds, or at significantly lower temperature later in the exhumation history.

In this contribution we report new quantitative data on deformation temperatures associated with north-directed (normal-sense) motion on the Zanskar Shear Zone (ZSZ), the westernmost strand of the STDS. Quartz fabrics were obtained from specimens demonstrably deformed during normal-sense motion on the ZSZ and therefore represent conditions attending Miocene extrusion

and exhumation of the HHCS. Quartz recrystallization mechanisms are described following the criteria of Stipp et al. (2002). Deformation temperatures are estimated using the quartz *c*-axis fabric opening angle thermometer (Kruhl, 1998). Finally, we use the inferred thermal architecture to estimate minimum dip-slip magnitudes of footwall rocks of the ZSZ.

4.2 Geologic framework

The South Tibetan Detachment in the Zanskar region (Fig. 4.2) of northern India (locally referred to as the Zanskar Shear Zone; ZSZ) separates the amphibolite facies and anatectic metamorphic core from the weakly to non-metamorphosed Tethyan Himalaya (Indian passive continental margin sequence; TH). Tethyan rocks in the hanging wall of the ZSZ are exposed as kilometer-scale S-verging, tight, upright to overturned and recumbent folds often separated by S-directed imbricated thrust faults. At the deepest levels exposed in the Zanskar HHCS elliptical to nearly circular domal uplifts cored by granitic gneisses and mantled by migmatitic gneisses are common (e.g., Kundig, 1989). These late domes are commonly framed by concentric mylonitic high-strain zones, and field mapping indicates that M_2 metamorphic isograds are warped around them indicating the domes developed after peak metamorphism (see Walker et al., 1999; Robyr et al., 2002, 2006; Searle et al., 2007). At higher structural levels, large-scale S-vergent recumbent folds or nappes separated by S-directed thrusts similar to those described from the TH are also observed (e.g., Tapshah, Donara, Phojal nappes). These structures likely formed contemporaneously with those observed in the TH during early crustal shortening and thickening associated with continental collision between India and Asia (e.g., Searle et al., 1992; Walker et al., 1999). S-facing recumbent folds in the HHCS have clearly been folded by the domes developed at lower structural levels (see discussion in Searle et al., 1992; Walker et al., 1999). At the highest structural levels mylonitic fabrics with abundant kinematic indicators overprint earlier microstructures and textures of footwall HHCS rocks (e.g., S–C fabrics, asymmetric pressure shadows, rotated porphryoblasts). Macro- and microstructures indicate ductile shearing associated with the ZSZ was top-N (normal-sense displacement). Locally, late stage brittle faults cut the mylonitic foliation in the ZSZ indicating the structure remained active at higher crustal levels (see Herren, 1987; Walker et al., 1999).

Microstructural relationships are closely related to the complex multi-stage macrostructural

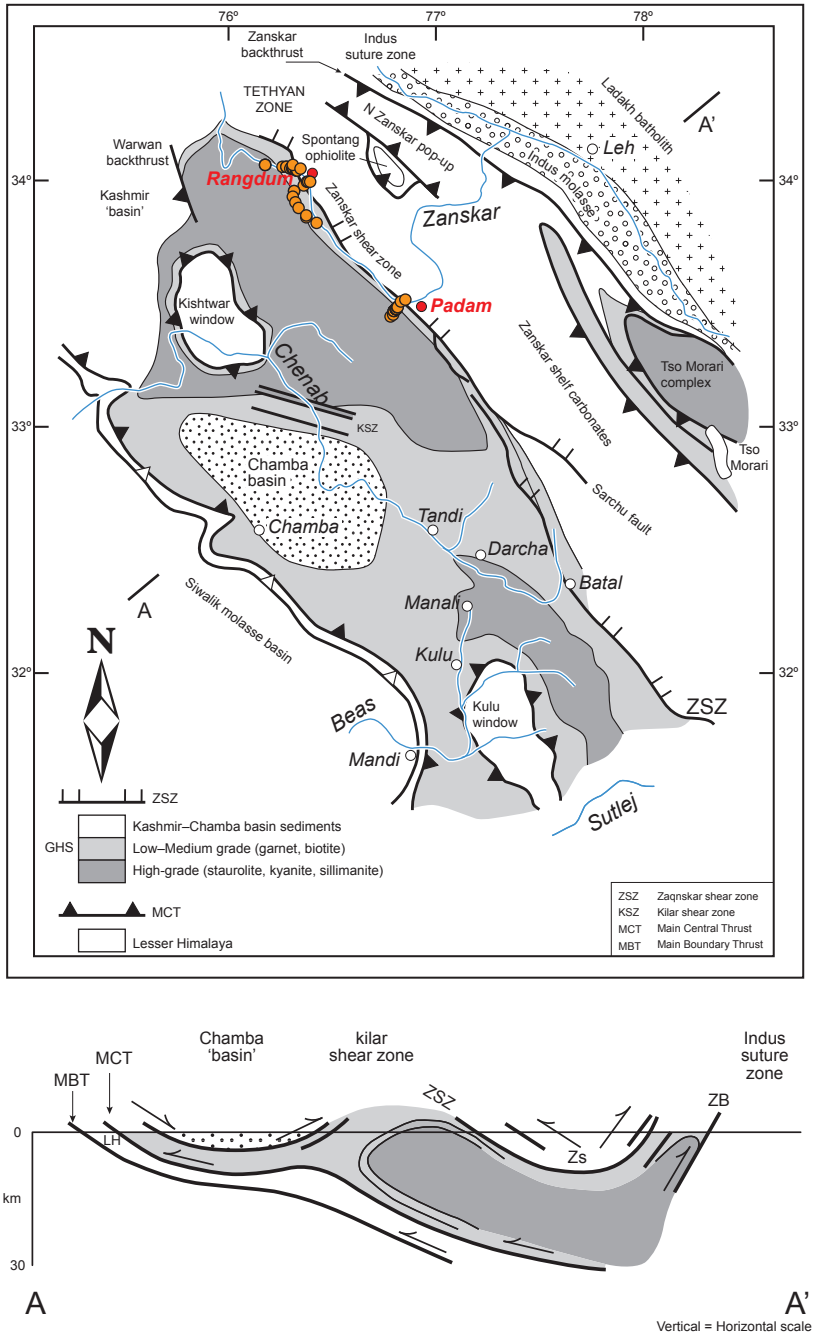

FIGURE 4.2. Simplified tectonic map of the Zanskar region. Distribution of major lithotectonic units indicated. Orange circles indicate locations of collected specimens. Cross section shows general geometry of HHCS and folded isograd surfaces. Modified from Searle et al. (2007).

evolution of the Zanskar region. Searle et al. (1992) and Walker et al. (2001) have provided detailed descriptions of microstructures from the Suru valley and surrounding area that they have used as a context to interpret a detailed metamorphic history. Metapelites preserve a variety of textures and microstructures (e.g., inclusion assemblages, porphyroblast–matrix relationships) re-

flecting the larger-scale structural evolution of the Zanskar region throughout the Eocene–Miocene. Key microstructural observations relating deformation events to distinct metamorphic episodes are briefly described below.

Two metamorphic events in the Zanskar region, M_1 and M_2, have been discussed as discrete events by Searle et al. (1992) in their development of a tectonic chronology of the Zanskar region. Although these are likely events experienced during a single protracted and relatively continuous HHCS metamorphism, we adopt this terminology for consistency here. The first recognized metamorphic event, M_1, was a result of burial and heating due to building overburden as stacking of D_1 folds and thrusts thickened the crust on the northern Indian passive margin. Porphryroblasts overgrew an early S_1 foliation, associated with D_1 folding and crustal thickening. S_1 is preserved as straight to sigmoidal inclusion trails in garnet and other porphyroblast cores. Early S_1 foliation may be continuous with the dominant S_2 matrix fabric suggesting syntectonic garnet growth during continually changing P–T conditions and re-orientation of (planar) fabric elements during progressive deformation. Kyanite porphyroblasts often overgrow matrix foliation indicating they formed late in the D_1 / M_1 evolution. These microstructural observations provide support of field relationships that the M_1 peak post-dated large-scale D_1 folding and thrusting at high structural levels in the HHCS. Quantitative P–T estimates for M_1 metamorphism are 650–680 °C and 9–10 kbar (Walker et al., 1999).

The dominant matrix foliation, S_2, was developed during D_2 thrusting on the MCT. Various geochronometers indicate that during this time the ZSZ was also active, and contributed to efficiently exhuming mid-crustal material to shallower crustal levels by acting as a passive roof fault. D_2 is expressed as a zone of localized ductile strain at the level of the MCT (with abundant top-to-S kinematic indicators), and is associated with the N–NE-dipping penetrative foliation developed throughout the HHCS. Top-S shear sense gives way to top-N kinematics in the upper 1–2 km of the HHCS affected by development of the ZSZ.

In the deepest exposed structural levels in Zanskar, along the axis of high-grade HHCS, a later M_2 metamorphic event overprints early M_1 kyanite-zone assemblages. M_2 is observed as sillimanite + muscovite and sillimanite + K-feldspar assemblages associated with migmatization and emplacement of leucogranites. M_2 metamorphism is interpreted to be associated with late D_2 deformation and is related to coeval motion on the MCT and ZSZ which rapidly exhumed HHCS

rocks from ∼9 to 5 kbar (i.e., from ∼30 to 15 km depth) without significant cooling. This resulted in decompression melting of metapelitic lithologies and generation and emplacement of leucogranites at high structural levels of the HHCS (see e.g., Walker et al., 1999). Also associated with latest D_2 deformation (i.e., post M_2 peak) is the formation of domes cored by granitic gneisses and mantled by high-grade metasediments discussed above. *P–T* estimates for peak M_2 metamorphism indicate equilibration at 700–750 °C and 4–7 kbar. Leucogranites associated with M_2 are dated at 21–19.5 Ma (Noble and Searle, 1995; Walker et al., 1999). Granite crystallization ages provide a maximum age constraint of latest ductile shearing along the ZSZ.

4.3 Analytical methods

Microstructural and crystal fabric data are reported from thin sections cut perpendicular to foliation and parallel to the NE-SW-trending stretching lineation. Lower hemisphere equal-area projections show the data as viewed toward the north, so that top-N (normal-sense) motion on the ZSZ is indicated by dextral shear sense. Quartz *c*-axis crystallographic fabrics were measured using a petrographic microscope equipped with a Leitz universal stage. Raw crystallographic orientation data were reduced using a Microsoft Excel (2001) routine written by S. Mulcahy.

We used quartz fabric opening angles, a technique first proposed by Kruhl (1998), to estimate temperatures attending deformation. Skeletal analysis (Lister and Williams, 1979) of quartz *c*-axis data was used to determine opening angles between the leading and trailing edge of the fabric skeleton. The precision of calculated deformation temperatures is not well-constrained and a nominal ± 50 °C uncertainty is assigned implicitly to all estimates reported here (see also Law et al., 2004).

4.4 Microstructural relationships

A suite of oriented samples for which we have excellent control on structural distance beneath the ZSZ was chosen for petrofabric analysis (Fig. 4.3). Locations of all samples collected are listed in 4.1. The selected specimens are dominated by plastically deformed and metamorphosed quartzofeldspathic psammitic rocks and granitoid of presumed Cambrian–Ordovician age. Quartz is modally abundant (commonly ≥ 30 vol%) in these rocks, but is not necessarily the most abundant

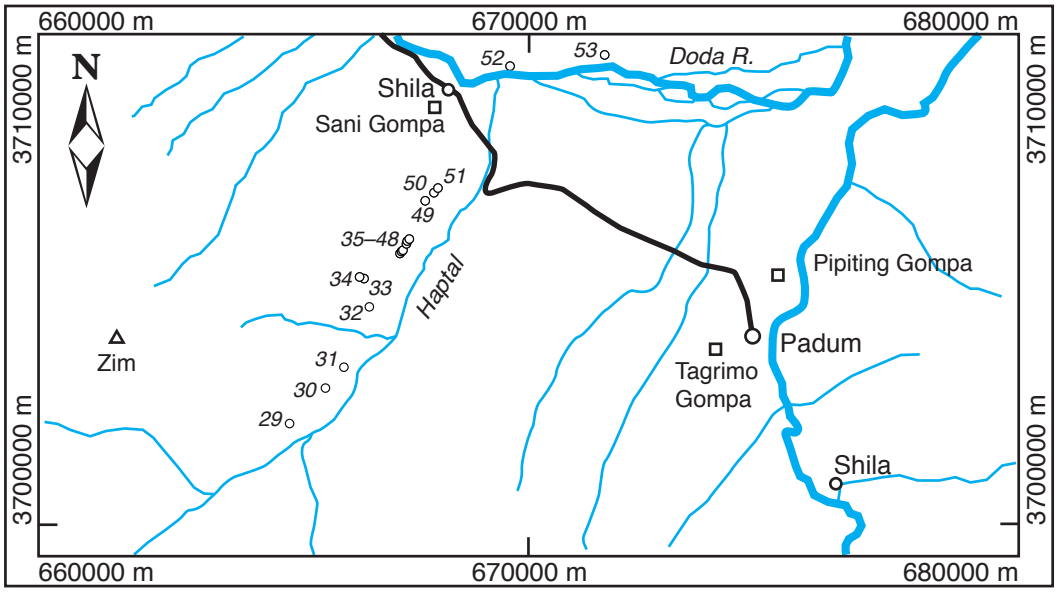

FIGURE 4.3. Map illustrating sample locations from the Padum section.

constituent of an individual specimen. The presence of alkali and plagioclase feldspars allows additional independent assessment of deformation mechanisms and inferred conditions active during deformation.

4.4.1 Quartz microstructures

Above the ZSZ slates of the Phe Formation contain relict quartz grains in a matrix of finer grained quartz and mica. Diffusive mass transfer (e.g., pressure solution) appears to have been an important mechanism accommodating strain as seams of insoluble material partially define the slaty cleavage.

At the structurally highest levels beneath the ZSZ quartz is dynamically recrystallized and displays evidence for recrystallization by subgrain rotation recrystallization (SGR) accompanied by grain boundary migration recrystallization (GBM). Sample Z09-49, a greenschist facies granitoid in the immediate footwall of the ZSZ, has the smallest recrystallized quartz grain size (∼10–30 μm) indicating recrystallization under high-stress conditions. Lenses of finely recrystallized quartz and feldspar wrap large (∼1 mm to 1 cm) feldspar augen. These microstructures correspond to the transition between regimes 2 and 3 of Hirth and Tullis (1992). According to Stipp et al. (2002) this recrystallization microstructure corresponds to minimum deformation temperatures of ∼500 °C at average geologic strain rates. White mica at this structural level is gently folded and displays undulose extinction.

At lower structural levels well-foliated quartz-rich granitoid and paragneisses are characterized by microstructures indicative of high-temperature grain boundary migration recrystallization. Quartz grains observed from structural levels ∼300–500 m below the ZSZ are dominated by deeply sutured grain boundaries indicative of GBM I or II of Stipp et al. (2002) (regime 3 of Hirth and Tullis, 1992). Such microstructures indicate minimum deformation temperatures of ∼550 °C at natural strain rates (Stipp et al., 2002). Quartz grain size is largely controlled by the local proportion of secondary phases. In regions where quartz is the dominant phase, recrystallized grain sizes are large (300–1500 μm) and display lobate and deeply sutured grain boundaries. In several samples from this structural level quartz is not the most modally abundant phase and often does not form an interconnected weak phase network. In specimens where quartz does form an interconnected network, ribbons or layers one grain (∼100–300 μm) thick are common. Accessory phases such as apatite and tourmaline are fractured and boudinaged with quartz in-filling the fractures.

At the deepest structural levels investigated, ≥ 1500 m beneath the ZSZ, rectangular and blocky quartz grains form monomineralic quartz ribbons and layers ≥ 300 μm thick, with single grains locally ≥ 3 mm in their longest dimension parallel to foliation. Evidence for simultaneous operation of prism-[c] and basal ¡a¿-slip (i.e., chessboard extinction patterns) is present but not pervasive. Quartz in monomineralic layers may display subgrain boundaries and sweeping extinction, but more commonly appears recovered and strain-free.

4.4.2 Feldspar microstructures

Alkali and plagioclase feldspars display a range of deformation-induced microstructures that correlate with structural distance beneath the detachment. In the immediate footwall of the ZSZ alkali and plagioclase feldspar display evidence for both brittle fracture and intracrystalline plasticity (Fig. 4.4).

TABLE 4.1. Zanskar sample locations

Sample	Latitude			Longitude			Elevation	Foliation		
	Deg	Min	Sec	Deg	Min	Sec	m	Strike	Dip	Dip dir
Z-09-01	33	58	53.28	76	22	3.66	4277	020	25	E
Z-09-02A/B	34	03	6.06	76	16	2.28	4065	006	40	E

Continued on next page

Table 4.1 – *Continued from previous page*

Sample	Latitude			Longitude			Elevation	Foliation		
	Deg	Min	Sec	Deg	Min	Sec	m	Strike	Dip	Dip dir
Z-09-03A/B	34	03	19.14	76	17	3.78	4210	012	28	E
Z-09-04	34	03	23.70	76	17	6.36	4246	025	38	E
Z-09-05A/B	34	03	21.72	76	18	35.58	4013	001	58	E
Z-09-06	34	03	22.98	76	18	58.62	4017	155	36	E
Z-09-07	33	57	30.54	76	19	21.60	4094	178	42	E
Z-09-08A/B	33	57	29.82	76	19	16.74	4080	007	38	E
Z-09-09	33	56	13.98	76	19	0.24	4124	150	32	E
Z-09-10	33	54	29.16	76	19	44.10	4263	160	26	E
Z-09-11	33	53	20.94	76	20	32.52	4531	165	44	E
Z-09-12A/B	float blocks at Pensi La									
Z-09-13	33	51	1.20	76	22	51.84	4142	125	44	E
Z-09-14	33	51	15.36	76	22	49.02	4287	127	45	E
Z-09-15	34	02	42.24	76	18	12.36	4015	005	31	E
Z-09-16	34	02	46.56	76	18	45.78	4005	020	40	E
Z-09-17	34	02	46.68	76	19	6.18	3995	173	34	E
Z-09-18	34	02	46.08	76	19	9.72	3998	160	30	E
Z-09-19	34	02	45.60	76	19	12.72	3998	155	42	E
Z-09-20	34	02	21.96	76	19	57.96	4091	166	42	E
Z-09-21	34	02	18.60	76	20	1.08	4123	167	44	E
Z-09-22	34	02	12.42	76	20	9.96	4148	157	40	E
Z-09-23	33	59	31.74	76	23	0.36	4162	150	41	E
Z-09-24	33	59	32.04	76	23	18.06	4186	171	51	E
Z-09-25	33	59	41.70	76	23	56.40	4144	000	49	E
Z-09-26	34	03	57.54	76	19	3.18	4035	168	55	E
Z-09-27	34	03	2.64	76	21	13.50	4014	168	52	E
Z-09-28	33	27	6.36	76	47	10.68	3824	unoriented		
Z-09-29	33	26	42.78	76	46	42.24	3884	000	28	E
Z-09-30A/B	33	27	20.28	76	47	25.32	3773	120	28	E
Z-09-31	33	28	0.36	76	47	45.48	3860	155	47	E
Z-09-32	33	28	19.14	76	47	41.28	4064	005	60	E
Z-09-33	33	28	20.22	76	47	37.74	4125	090	44	S
Z-09-34	33	28	20.22	76	47	37.74	4125	042	40	W
Z-09-35	33	28	35.82	76	48	9.78	3831	147	27	E
Z-09-36	33	28	37.14	76	48	10.98	3824	005	25	E
Z-09-37	33	28	37.98	76	48	12.12	3820	147	28	E
Z-09-38	33	28	42.24	76	48	14.88	3814	097	27	E
Z-09-39A/B	33	28	44.10	76	48	15.54	3817	115	24	E
Z-09-40	33	28	45.42	76	48	17.16	3802	157	21	E
Z-09-41	33	28	47.94	76	48	20.34	3786	128	29	E
Z-09-42	33	28	47.94	76	48	20.34	3786	122	28	E
Z-09-43	33	28	47.94	76	48	20.34	3786	130	30	E
Z-09-44	33	28	47.94	76	48	20.34	3786	125	30	E
Z-09-45	33	28	47.94	76	48	20.34	3786	140	31	E

Continued on next page

Table 4.1 – *Continued from previous page*

Sample	Latitude			Longitude			Elevation	Foliation		
	Deg	Min	Sec	Deg	Min	Sec	m	Strike	Dip	Dip dir
Z-09-46	33	28	47.94	76	48	20.34	3786	110	28	E
Z-09-47	33	28	47.94	76	48	20.34	3786	130	28	E
Z-09-48	33	28	47.94	76	48	20.34	3786	unoriented		
Z-09-49	33	29	10.86	76	48	29.76	3829	132	18	E
Z-09-50	33	29	16.20	76	48	36.72	3807	138	47	E
Z-09-51	33	29	19.32	76	48	39.84	3795	147	55	E
Z-09-52	33	30	36.90	76	49	37.02	3596	005	75	E
Z-09-53	33	30	44.34	76	50	52.02	3592	013	83	E
Z-09-54	33	49	42.54	76	25	37.44	4074	020	32	E
Z-09-55	34	03	49.98	76	11	12.12	3943	045	65	N
Z-09-56	34	03	49.98	76	11	12.12	3943	147	77	W
Z-09-57	34	03	49.98	76	11	12.12	3943	090	52	S

Many smaller porphyroclasts in the same specimen, however, appear completely recrystallized. Myrmekite is developed on margins of alkali feldspar porphyroclasts, indicating deformation under at least mid–upper greenschist facies conditions (e.g., Simpson and Wintsch, 1989; Tullis, 2002). All of the largest alkali feldspar augen display pervasive undulatory extinction, and some clasts appear to have internal fractures that may or may not be associated with small recrystallized grains at the fracture margins. Smaller alkali or plagioclase feldspar porphyroclasts isolated in dynamically recrystallized quartz layers have locally deformed by fracture as well. Other alkali feldspar clasts appear to be stretched into ribbon-like grains (up to 1.5 cm in longest dimension) and flattened into the foliation. Low-angle subgrain boundaries are clearly visible in some plagioclase grains. The difference in deformation mechanism of these feldspar augen may be due to several factors including orientation in the flow (e.g., whether critical resolved shear stress required for slip on favorably-oriented cleavage planes is realized) and relative competence of surrounding material. Much of the large, presumably primary, white mica in this sample is aligned within the foliation and warped into gentle low-wavelength folds. These white mica porphyroclasts display undulatory extinction, and some appear to show incipient recrystallization at their margins or in the hinges of folds.

Between ∼300 and 500 m beneath the ZSZ feldspar is characterized by sweeping undulatory extinction, deeply sutured and lobate grain boundaries, deformation-induced mechanical twins, strain-

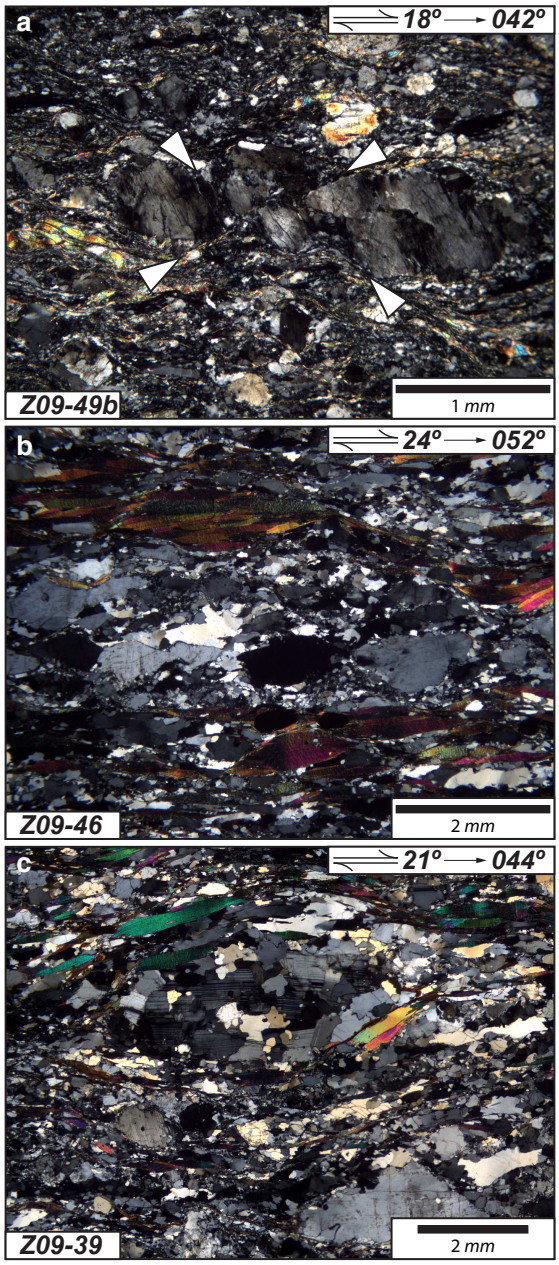

FIGURE 4.4. Representative feldspar microstructures from high structural levels of the HHCS. (a) Alkali feldspar augen from sample collected < 10 m beneath detachment. Note pervasive undulatory extinction and brittle fracture displacing grain fragments (arrows). Recrystallized quartz + feldspar matrix grain size 10–30 μm. (b) Partially recrystallized porphyroclast from sample collected ∼300 m beneath detachment. Note lobate margins of both quartz and feldspar and larger recrystallized quartz grain size. (c) Similar microstructure as in (b), from sample collected ∼500 m beneath detachment. Crossed polarizers.

induced myrmekite at high-stress, foliation-parallel grain boundaries, subgrain development, and core and mantle structure (recrystallization into finer-grained aggregates at porphyroclast margins). Albite-law twins are occasionally truncated at subgrain boundaries in plagioclase porphyroclasts. Many clasts show a consistent relationship with pericline-law twins cross cutting and deflecting

earlier-formed polysynthetic albite-law twins where both are developed in the same grain (Fig. 4.5). Rarely, flame-shaped exsolution lamellae developed in alkali feldspar porphyroclasts. Relict

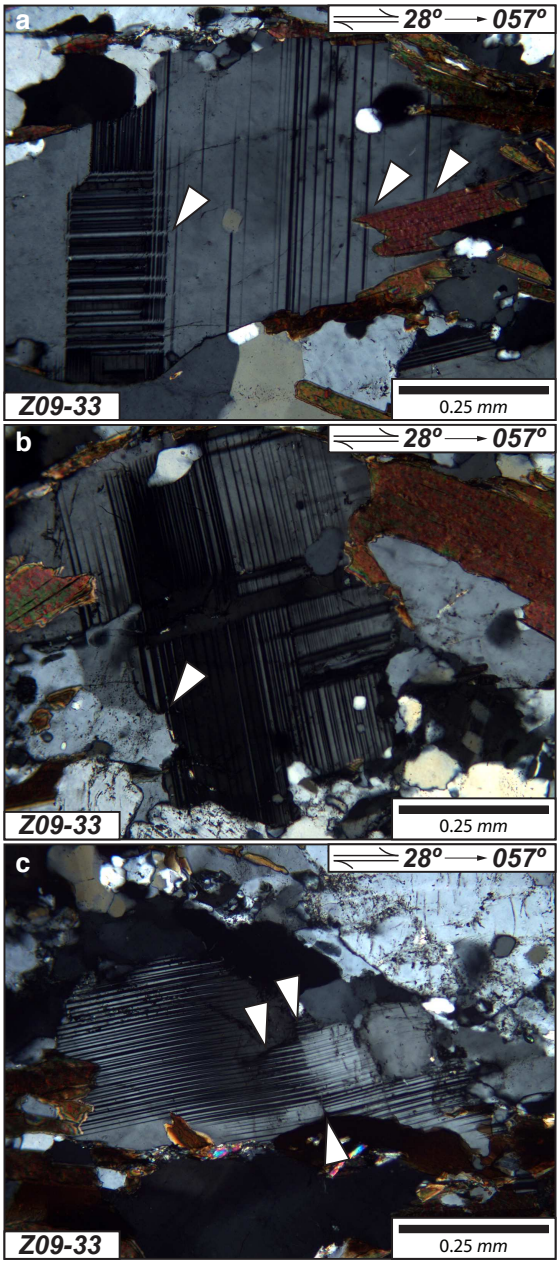

FIGURE 4.5. Representative feldspar microstructures from middle structural levels of the HHCS. Bent crystal lattices and strain-induced mechanical twins in plagioclase. (a) Deformation-induced albite- and pericline-law twins in plagioclase. Note deflection of earlier-formed albite-law twins where intersected by later pericline-law twins. (b) Cuspate-lobate boundaries and truncation of twins by plagioclase, biotite, and quartz indicates grain boundary mobility. (c) Deflection or truncation of deformation twins at deformation band boundary. Crossed polarizers.

plagioclase phenocrysts have commonly partially or totally recrystallized into a mosaic of recrystallized grains (200–500 μm) of different orientation (Fig. 4.4). Ribbons of recrystallized quartz

and feldspar partly define the penetrative foliation. In many samples from this structural interval quartz and mica are minor modal constituents do not form an interconnected weak-phase network.

At ~900 m beneath the ZSZ plagioclase appears to be flattened into the foliation and locally displays deformation-induced mechanical twins following the albite (dominant) and pericline (rare) laws. Occasionally the same temporal relationship described above can be deduced when a single grain contains both albite and pericline twins. Plagioclase-plagioclase grain boundaries are sutured and lobate presumably due to grain boundary migration, and are not in an equilibrium configuration.

At the deepest structural levels investigated ($\geq$ 1500 m beneath the detachment) widespread crystal plasticity is observed in alkali and plagioclase feldspar (Fig. 4.6). Primary white mica is no longer present in metagranitoid specimen Z09-30 (~2200 m beneath ZSZ); the peak assemblage is plagioclase–alkali feldspar–biotite–quartz–sillimanite plus accessory phases. Sillimanite is aligned into and partly defines the fabric and shear bands that cross cut foliation. Large relict primary alkali feldspar with simple twins are enveloped by recrystallized feldspar (core and mantle structure) and are wrapped by quartz ribbons and sillimanite±biotite folia (Figs. 4.6, 4.7). Grain boundaries are deeply sutured, and totally recrystallized relict alkali feldspar augen are present with aligned, blocky rectangular recrystallized grains that define an oblique grain-shape foliation Fig. 4.6). These recrystallized alkali feldspar grains are approximately the same size (~300–600 μm) or slightly smaller than GBM recrystallized quartz in ribbons throughout the thin section. Some completely recrystallized alkali feldspar augen display 120° triple junctions of recrystallized grains, suggesting the grain boundaries have migrated into an equilibrium configuration. Similar grain size of recrystallized quartz and feldspar at this level beneath the ZSZ may indicate there was no significant rheologic contrast between these phases during deformation and exhumation of the HHCS (Rosenberg and Stünitz, 2003).

4.5 Quartz crystallographic fabrics

Quartz fabrics developed at ~300–500 m beneath the ZSZ show well-developed asymmetric cross-girdle fabrics (Lister, 1977) in which the central girdle intersects the foliation plane perpendicular to the penetrative NE-plunging stretching lineation. Such a relationship has been produced in

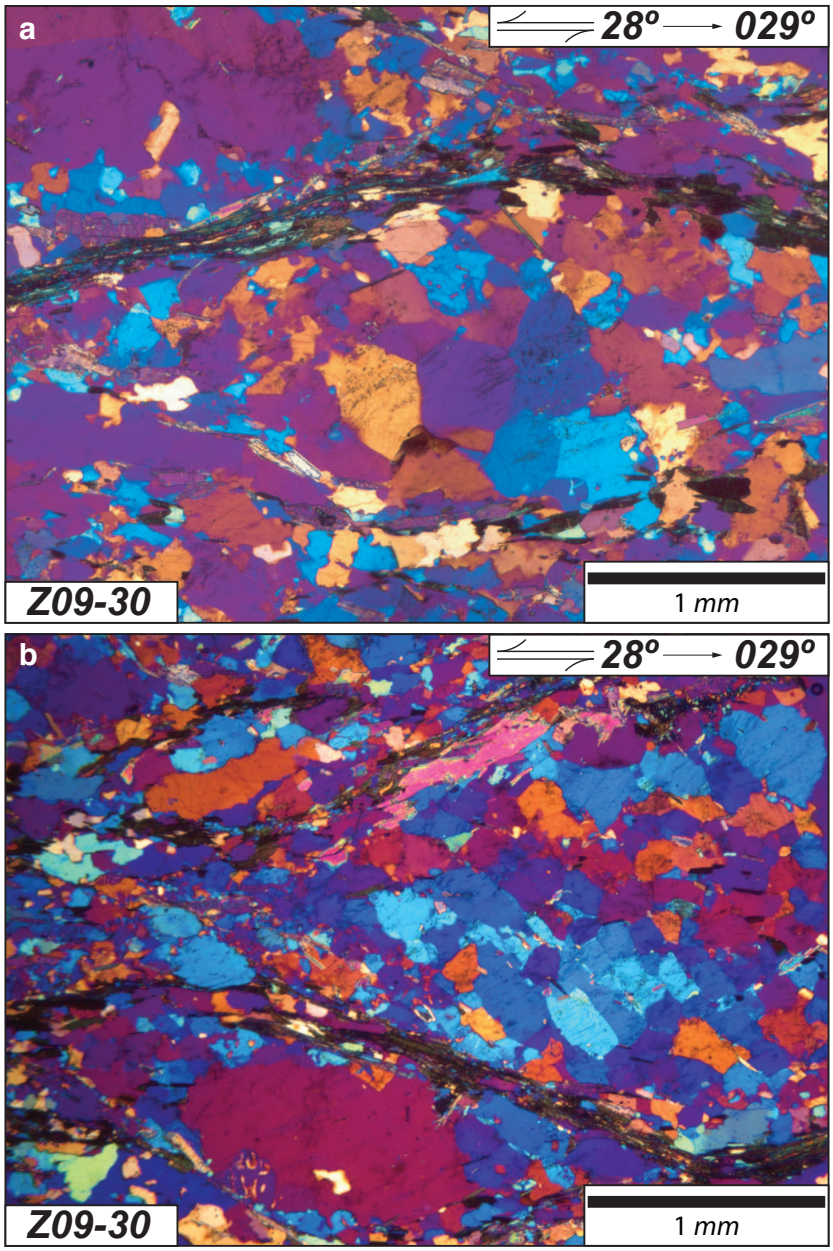

FIGURE 4.6. Representative feldspar microstructures from deepest structural levels of HHCS. (a) Fully recrystallized alkali feldspar augen from sample collected ~2.2 km beneath detachment. Note 120° triple junctions indicating attainment of equilibrium. (b) Fully recrystallized alkali feldspar augen from same sample as in (a) displaying oblique recrystallized grain shape defined by aligned recrystallized alkali feldspar grains. Note the oblique recrystallized grain shape alignment suggests top-SW shear sense. Crossed polarizers and 550 nm accessory plate inserted.

numerical simulations of deformed quartzites (Lister et al., 1978; Lister and Hobbs, 1980; Etchecopar and Vasseur, 1987) and supports the interpretation that the stretching lineation observed in ZSZ rocks reflects the orientation of maximum principal stretch and therefore is a close approximation to the tectonic transport direction. Quartz *c*-axis fabrics such as those observed in ZSZ mylonites

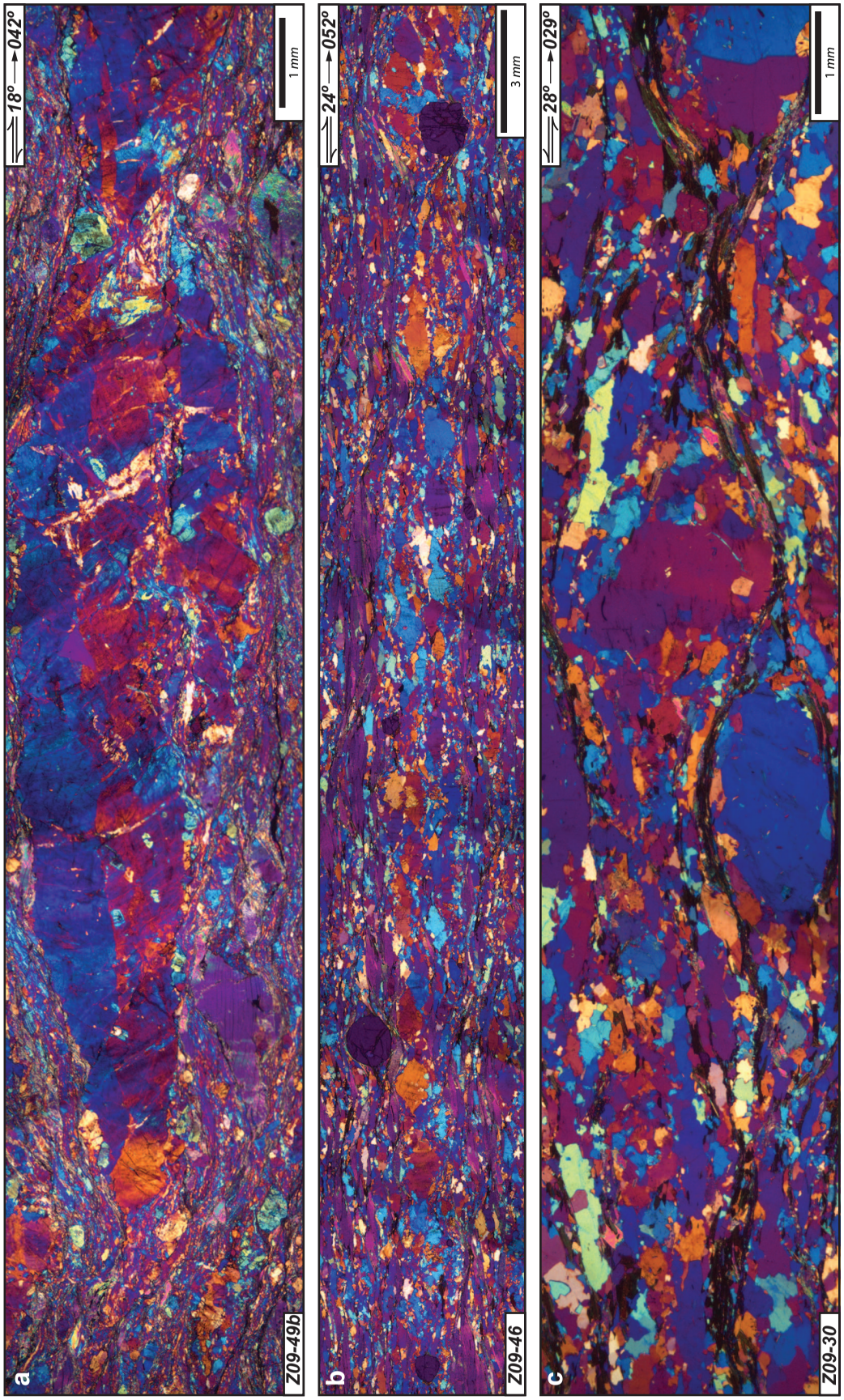

FIGURE 4.7. Composite micrograph images of selected samples from HHCS. (a) Sample from approximate level of ZSZ. Large (∼1 cm) fractured alkali feldspar porphyroclast. Recrystallized 10–30 μm feldspar grains occur in fractures and matrix. (b) Felspar-rich layer in sample from ∼500 m beneath ZSZ. Feldspar occurs as deeply sutured and partially to totally recrystallized grains, wrapped by large ($\leq$ 1000 μm long) dynamically recrystallized quartz and smaller feldspar. (c) Sample from ∼2200 m beneath ZSZ. Note large ($\leq$ 300 μm) recrystallized feldspar grain size. Relict alkali feldspar augen wrapped by dynamically recrystallized quartz $\geq$ 1 mm in longest dimension and biotite + sillimanite folia.

also support the assertion that deformation was likely approximately plane strain. Asymmetry in the *c*-axis distribution indicates a top-NE (i.e., normal-sense) shear consistent with kinematic indicators (e.g., rotated feldspar clasts, S–C fabric, extensional shear bands) observed in the field and thin section.

4.6 Deformation temperatures

Results of quartz *c*-axis fabric analyses are presented in Figure 4.8. A linear dependence of opening angle (and therefore deformation temperature) versus structural distance is apparent at the structural interval investigated (Fig. 4.9). Here inferred deformation temperature decreases with decreasing structural distance below the ZSZ, consistent with observed right-way-up metamorphic isograds and a metamorphic sequence of normal polarity observed at the top of the HHCS elsewhere in the orogen (e.g., Searle and Rex, 1989; Vannay et al., 1999; Hodges, 2000). The linear dependence results in an apparent thermal field gradient of ~275 °C km^{-1} for this structural interval.

4.7 Telescoping of syn-deformation isotherms

Telescoping of deformation temperatures observed in the uppermost HHCS can be accomplished in a number of ways. Here we provide calculations of minimum dip-slip displacement on the ZSZ based on a simplified geometry and end-member pure and simple shear strain paths.

4.7.1 Pure shear flattening

If the observed spacing between the 600 and 625 °C deformation isotherms (~200 m) is due to a vertical pure shear, then the amount of strain required to produce this final state may be calculated if the initial thermal gradient at the time of deformation is known (see e.g., Law et al., 2011). We have no way of determining the thermal gradient in the ZSZ at the time of deformation, but for our calculations we use values of 25 and 40 °C km^{-1} for both a standard and somewhat elevated linear geothermal gradient to assess the likely range of strain required to produce the observed spacing. For these geothermal gradients, a vertical flattening of 80 and 68%, respectively, is required to produce the observed spacing of deformation isotherms (Fig. 4.10). These result in strain ratios of

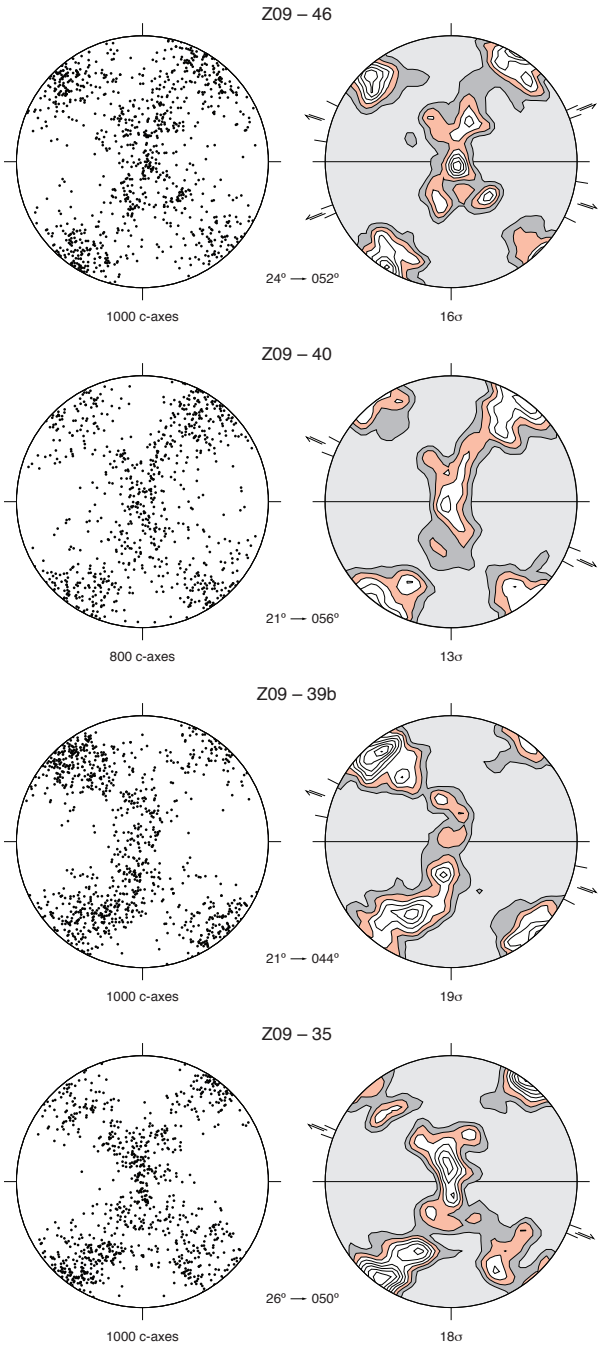

FIGURE 4.8. Lower hemisphere, equal area projections of quartz *c*-axes from HHCS rocks of the Padum area. Contoured using a modified version of Kamb's (1959) method (Vollmer, 1995). Contour interval is 2σ beginning at 3σ. Maximum concentration indicated.

25 and 10, and finite maximum principle stretches of 400 and 212.5% perpendicular to the flattening plane, respectively.

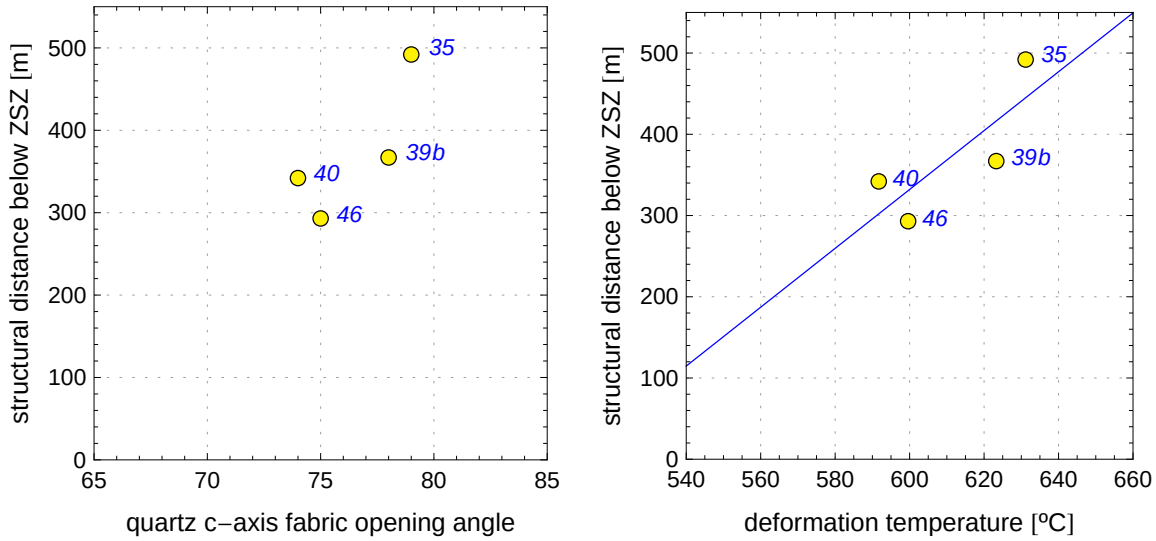

FIGURE 4.9. Calculated deformation temperatures for Padum section. Plots indicate measured quartz *c*-axis fabric opening angles and corresponding deformation temperature. Linear regression through data indicate an apparent gradient of ~276 °C km^{-1}.

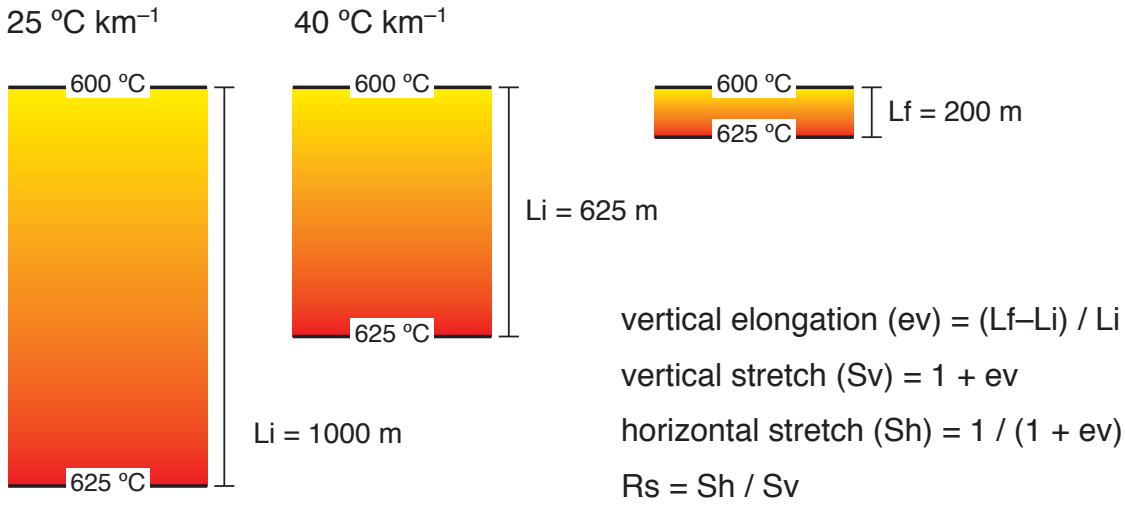

FIGURE 4.10. Pure shear model for telescoping isograds. Geothermal gradients of 25 and 40 °C km^{-1} shown, as well as final spacing as observed in Padum. General calculations used for vertical shortening and horizontal stretch indicated. Finite strain ratios required to produce the observed spacing between the 600 and 625 °C particle are 25 and 10, respectively. These finite strains result in a transport-parallel stretch of 400 and 212.5%, respectively.

4.7.2 Heterogeneous simple shear

We next examine predictions of a model where telescoping of isograds is the result of heterogeneous simple shear parallel to the overlying ZSZ. In this model particles originating at different depths, based on their deformation temperature and again assuming a horizontal geothermal gradient, are displaced a variable distance in the transport direction until they attain their observed spacing. The lower 625 °C particle comes to rest at a level in the crust corresponding to 300 °C (i.e.,

approximately at the brittle–ductile transition). Again, instantaneous geothermal gradients of 25 and 40 °C km^{-1} were assumed for comparison to the above pure shear model predictions. Our simple shear model predicts dip-slip displacements of 15–36 km for the upper (600 °C) particle, and 16–38 km for the lower (625 °C) particle, depending on geothermal gradient and detachment dip (30° vs. 20° here) used in the calculations (Fig. 4.11). The differential displacement between

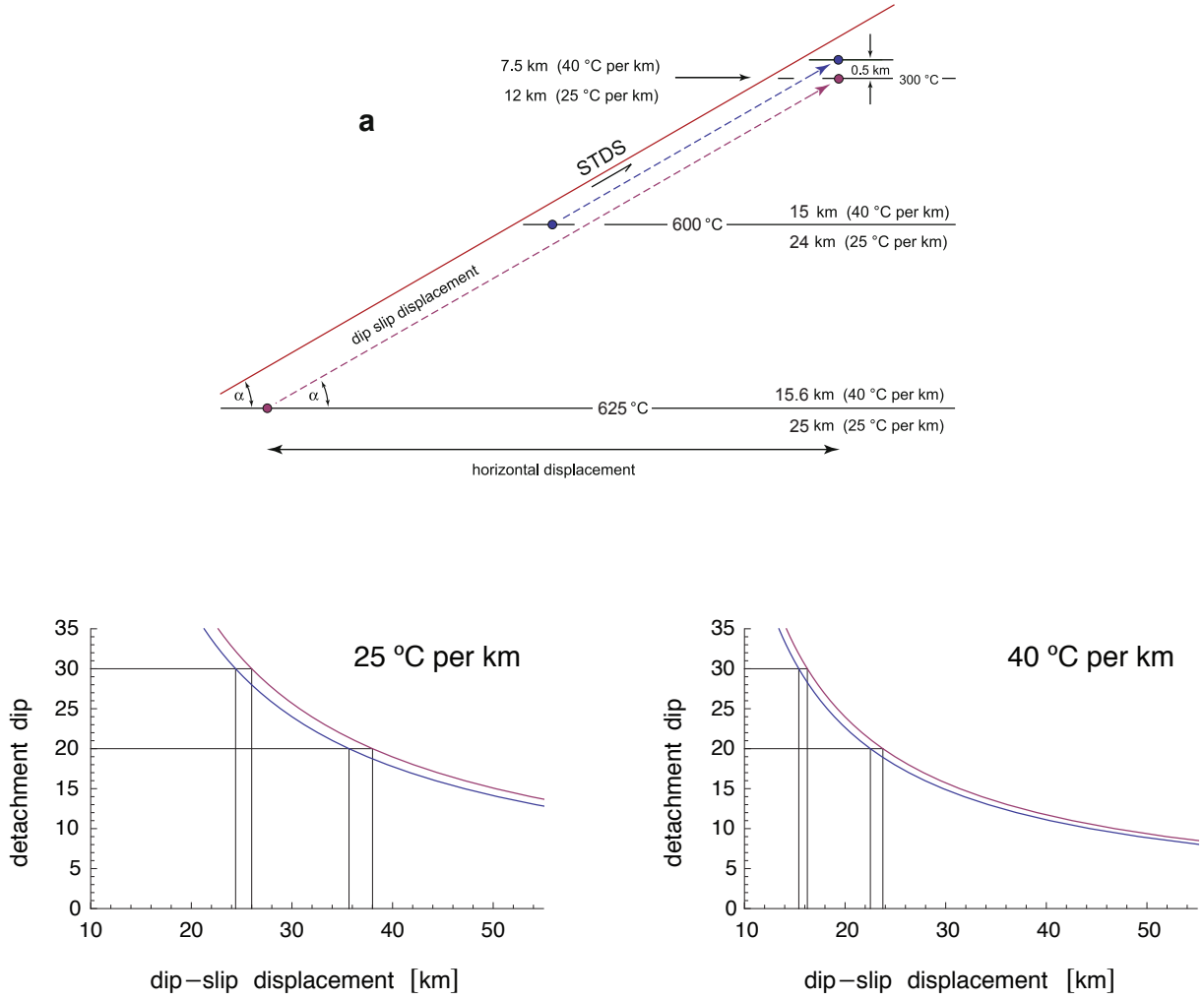

FIGURE 4.11. Differential particle displacement model for telescoping isograds. (a) Geometrical relationships used in calculations. Model assumes simple shear parallel to overlying ZSZ and that lower 625 °C particles is displaced up to 300 °C (approximate brittle-ductile transition). (b) Plots illustrating required dip-slip displacement of upper 600 °C and lower 625 °C particle for geothermal gradients of 25 and 40 °C km^{-1}.

the two particles is small, with the lower 625 °C particle experiencing only ∼1–2 km additional displacement due to the relatively small temperature difference at the top and bottom of the section. Collectively, a differential particle displacement path model assuming heterogenous simple shear parallel to the detachment requires slip magnitudes on the order of 15–40 km to explain the

observed telescoping of deformation isotherms in the Padum section.

4.8 Discussion

4.8.1 Deformation temperature estimates

Our estimates of the magnitude of telescoping of the preserved thermal architecture would not be possible for the section investigated (Haptal Nala, SW of Padum) by other commonly used analytical methods such as quartz recrystallization regimes, or spacing of mapped isograds because: i) microstructures are relatively consistent across the structural interval investigated here; and ii) HHCS rocks in this section are dominated by metamorphosed granitic to psammitic rocks with a characteristic high thermodynamic variance. Therefore, we suggest that the methodology adopted here may be useful in regions where conventional indicators of either the thermal setting attending deformation or the preserved thermal structure of an area are not obvious in the field.

Results of our microstructural and quartz petrofabric analyses indicate an apparent thermal gradient of ~276 °C km^{-1} for the structural interval between 300–500 m below the detachment near Padum. The calculated deformation temperatures (600–625 °C) are consistent with observed quartz recrystallization mechanisms (dominantly regime 3 of Hirth and Tullis, 1992; GBM I and II of Stipp et al., 2002) and clear evidence of ubiquitous feldspar plasticity. Apparent metamorphic field gradients have been recently estimated in the eastern Himalaya (southern Tibet, Cottle et al., 2011; Law et al., 2011; Bhutan, Kellett et al., 2010). Kellett et al. (2010) have determined a metamorphic field gradient of ~210 °C km^{-1} for an 850 m section of upper Greater Himalayan Series rocks based on thermobarometric analysis. Cottle et al. (2011) have estimated a condensed metamorphic field gradient of ~310 °C km^{-1} for the 1 km-thick STDS in the Dzakaa Chu section based on Raman spectroscopy on carbonaceous material and phase equilibria modeling. Our deformation temperature gradient results are consistent with both of these studies for similar stuctural positions using independent methods to assess near-peak metamorphic temperatures of the High Himalaya.

While the apparent deformation temperature gradient extracted in this work and previous studies of the metamorphic field gradient of the uppermost section of Higher Himalayan Crystallines are high, all are moderately to significantly lower than the 395 ± 25 °C km^{-1} obtained by Law et al. (2011) in the interval 0–500 m below the STDS in the Rongbuk area ~1000 km to the east.

Law et al. (2011) indicated that the relative hinterland versus foreland positions of the STDS in the southern Tibetan and Bhutan Himalaya above are not easily determined, and the Padum section of this work is ∼1000 km along strike to the west and its relative hinterland position in relation to the above works is equally uncertain. What is most striking about these studies into the preserved thermal architecture of the upper structural levels of the Himalayan metamorphic core is the broad agreement among several independent techniques into peak metamorphism and temperatures attending deformation. These studies to date have consistently resulted in similar estimates of the field gradients of observed temperatures (within a factor of 2) for $\leq$ 200 m (this study, Law et al., 2011) to 1 km of structural section (Cottle et al., 2011). Strongly condensed thermal field gradients across the orogen therefore must be a reflection of first-order processes and the importance of the role of the STDS for exhumation / extrusion of the Higher Himalayan Crystallines.

4.8.2 Zanskar Shear Zone dip-slip displacement estimates

Despite the simplified geometrical approach to our estimates of dip-slip displacement on the ZSZ, results of the calculations are consistent with others for nearby sections across the shear zone derived from independent criteria (Herren, 1987; Dèzes et al., 1999; Walker et al., 1999). Herren (1987) offered the first quantitative displacement estimate by using observed changes in spacing of mapped isograd surfaces in western Zanskar to estimate ∼25 km of slip in the dip direction on the ZSZ. Subsequently, Walker et al. (1999) used barometric data to infer displacements on the order of 40–60 km for samples near the Gumburanjon dome in southeastern Zanskar. These results are similar to the 35±9 km estimate of Dèzes et al. (1999) for the same area based on similar barometric analysis. Our dip-slip displacement estimates of 15–40 km based on heterogeneous simple shear parallel to the ZSZ and spacing of telescoped deformation temperatures are consistent with the above estimates from independent datasets.

4.9 Conclusions

1. Penetrative fabric and quartz microstructures developed during top-NE shearing and extrusion / exhumation of Higher Himalayan Crystallines in the Zanskar region.

2. Deformation temperatures inferred from quartz *c*-axis fabrics from 300–500 m structurally beneath the ZSZ range from 600 to 625 °C, resulting in an apparent thermal gradient of ~275 °C km^{-1} for this structural interval.

3. Elevated deformation temperatures are consistent with observed dynamic recrystallization regimes of quartz and inferred deformation mechanisms in feldspar.

4. Calculated dip-slip displacement of upper HHCS rocks of 15–40 km are consistent with previous estimates based on independent criteria (Herren, 1987; Dèzes et al., 1999; Walker et al., 1999).

References

Cottle, J., Waters, D., Riley, D., Beyssac, O., Jessup, M., 2011. Metamorphic history of the South Tibetan Detachment System, Mt. Everest region, revealed by RSCM thermometry and phase equilibria modelling. Journal of Metamorphic Geology 29, 561–582.

Dèzes, P.J., Vannay, J.C., Steck, A., Bussy, F., Cosca, M., 1999. Synorogenic extension: Quantitative constraints on the age and displacement of the Zanskar shear zone (northwest Himalaya). Geological Society of America Bulletin 111, 364–374.

Etchecopar, A., Vasseur, G., 1987. A 3-d kinematic model of fabric development in polycrystalline aggregates: comparisons with experimental and natural examples. Journal of Structural Geology 9, 705–717.

Godin, L., Grujic, D., Law, R., Searle, M., 2006. Channel flow, ductile extrusion and exhumation in continental collision zones: an introduction. In: Law, R.D., Searle, M.P., Godin, L. (Eds.), Channel Flow, Ductile Extrusion and Exhumation in Continental Collision Zones, vol. 268, pp. 1–23.

Grujic, D., Casey, M., Davidson, C., Hollister, L.S., Kündig, R., Pavlis, T., Schmid, S., 1996. Ductile extrusion of the Higher Himalayan Crystalline in Bhutan: evidence from quartz microfabrics. Tectonophysics 260, 21–43.

Herren, E., 1987. Zanskar shear zone: Northeast-southwest extension within the Higher Himalayas (Ladakh, India). Geology 15, 409–413.

Hirth, G., Tullis, J., 1992. Dislocation creep regimes in quartz aggregates. Journal of Structural Geology 14, 145–159.

Hodges, K.V., 2000. Tectonics of the Himalaya and southern Tibet from two perspectives. Geological Society of America Bulletin 112, 324–350.

Kamb, W.B., 1959. Ice petrofabric observations from Blue Glacier, Washington, in relation to theory and experiment. Journal of Geophysical Research 64, 1891–1909.

Kellett, D., Grujic, D., Warren, C., Cottle, J., Jamieson, R., Tenzin, T., 2010. Metamorphic history of a syn-convergent orogen-parallel detachment: The South Tibetan detachment system, Bhutan Himalaya. Journal of Metamorphic Geology 28, 785–808.

Kruhl, J., 1998. Reply: Prism- and basal-plane parallel subgrain boundaries in quartz: A microstructural geothermabarometer. Journal of Metamorphic Petrology 16, 142–146.

Kundig, R., 1989. Domal structures and high-grade metamorphism in the Higher Himalayan Crystalline, Zanskar Region, north-west Himalaya, India. Journal of Metamorphic Geology 7, 43–55.

Law, R., Jessup, M., Searle, M., Francsis, M., Waters, D., Cottle, J., 2011. Telescoping of isotherms beneath the South Tibetan Detachment System, Mount Everest Massif. Journal of Structural Geology 33, 1569–1594.

Law, R.D., Searle, M.P., Godin, L., 2006. Channel flow, ductile extrusion and exhumation in continental collision zones. Geological Society of London, Special Publication, vol. 268, 620 pp.

Law, R.D., Searle, M.P., Simpson, R.L., 2004. Strain, deformation temperatures and vorticity of flow at the top of the Greater Himalayan Slab, Everest Massif, Tibet. Journal of the Geological Society of London 161, 305–320.

Lister, G., 1977. Discussion: Crossed-girdle c-axis fabrics in quartzites plastically deformed by plane strain and progressive simple shear. Tectonophysics 39, 51–54.

Lister, G., Hobbs, B., 1980. The simulation of fabric development during plastic deformation and its application to quartzite: the influence of deformation history. Journal of Structural Geology 2, 355–370.

Lister, G., Paterson, M., Hobbs, B., 1978. The simulation of fabric development in plastic deformation and its application to quartzite: the model. Tectonophysics 45, 107–158.

Lister, G., Williams, P., 1979. Fabric development in shear zones: theoretical controls and observed phenomena. Journal of Structural Geology 1, 283–297.

Noble, S., Searle, M., 1995. Age of crustal melting and leucogranite formation from U-Pb zircon and monazite dating in the western Himalaya, Zanskar, India. Geology 23, 1135.

Robyr, M., Hacker, B., Mattinson, J., 2006. Doming in compressional orogenic settings: new geochronological constraints from the NW Himalaya. Tectonics 25, TC2007.

Robyr, M., Vannay, J., Epard, J., Steck, A., 2002. Thrusting, extension, and doming during the polyphase tectonometamorphic evolution of the High Himalayan Crystalline Zone in NW India. Journal of Asian Earth Sciences 21, 221–239.

Rosenberg, C.L., Stünitz, H., 2003. Deformation and recrystallization of plagioclase along a temperature gradient: an example from the Bergell tonalite. Journal of Structural Geology 25, 389–408.

Searle, M., Law, R., Godin, L., Larson, K., Streule, M., Cottle, J., Jessup, M., 2008. Defining the himalayan main central thrust in Nepal. Journal of the Geological Society of London 165, 523–534.

Searle, M., Waters, D., Rex, D., Wilson, R., 1992. Pressure, temperature and time constraints on Himalayan metamorphism from eastern Kashmir and western Zanskar. Journal of the Geological Society 149, 753.

Searle, M.P., Rex, A.J., 1989. Thermal model for the Zanskar Himalaya. Journal of Metamorphic Geology 7, 127–134.

Searle, M.P., Stephenson, B., Walker, J., Walker, C., 2007. Restoration of the western himalaya: implications for metamorphic protoliths, thrust and normal faulting, and channel flow models. Episodes 30, 242.

Simpson, C., Wintsch, R., 1989. Evidence for deformation-induced k-feldspar replacement by myrmekite. Journal of Metamorphic Geology 7, 261–275.

Stipp, M., Stünitz, H., Heilbronner, R., Schmid, S.M., 2002. The eastern Tonale fault zone: a natural laboratory for crystal plastic deformation of quartz over a temperature range from 250 to 700 C. Journal of Structural Geology 24, 1861–1884.

Tullis, J., 2002. Deformation of granitic rocks: experimental studies and natural examples. Reviews in mineralogy and geochemistry 51, 51–95.

Vannay, J.C., Grasemann, B., 2001. Himalayan inverted metamorphism and syn-convergence extension as a consequence of a general shear extrusion. Geological Magazine 138, 253–276.

Vannay, J.C., Sharp, Z.D., Grasemann, B., 1999. Himalayan inverted metamorphism constrained by oxygen isotope thermometry. Contributions to Mineralogy and Petrology 137, 90–101.

Vollmer, F.W., 1995. C program for automatic contouring of spherical orientation data using a modified kamb method. Computers & Geosciences 21, 31–49.

Walker, C.B., Searle, M.P., Waters, D.J., 2001. An integrated tectonothermal model for the evolution of the High Himalaya in western Zanskar with constraints from thermobarometry and metamorphic modeling. Tectonics 20, 810–833.

Walker, J.D., Martin, M.W., Bowring, S.A., Searle, M.P., Hodges, K.V., 1999. Metamorphism, melting, and extension: Age constraints from the High Himalayan Slab of southeast Zanskar and northwest Lahaul. The Journal of Geology 107, 473–495.